Photothermal and Photochemical Tumor Response to Carbon Nanotube Mediated Laser Cancer Therapy

By

Saugata Sarkar

Dissertation submitted to the faculty of the Virginia Polytechnic Institute and State University in partial fulfillment of the requirements for the degree of

DOCTOR OF PHILOSOPHY
In
Mechanical Engineering

Marissa Nichole Rylander, Committee Chair
Thomas E. Diller
Harry C. Dorn
Scott T. Huxtable
James E. Mahaney
Christopher G. Rylander
Suzy Torti

September 7, 2010
Blacksburg, Virginia

Keywords: cancer treatment, nanoparticles, thermal conductivity, optical properties, reactive oxygen species, free radical, cellular uptake, tumor model.

Photothermal and Photochemical Tumor Response to Carbon Nanotube Mediated Laser Cancer Therapy

By
Saugata Sarkar

ABSTRACT

The objective of this study was to determine the photothermal and photochemical tissue response to carbon nanotube inclusion in laser therapy using experimental and computational methods. In this study, we specifically considered varying types and concentrations (0.01-1 mg/ml) of carbon nanotubes (CNTs), e.g., multi-walled carbon nanotubes (MWNTs), single-walled carbon nanotubes (SWNTs), and single-walled carbon nanohorns (SWNHs). In order to determine the photothermal effect of CNT inclusion, the thermal conductivity and optical properties of tissue representative phantoms with CNT inclusion were measured. Thermal conductivity of tissue phantoms containing CNTs was measured using the hot wire probe method. For identical CNT concentrations, phantoms containing MWNTs had the highest thermal conductivity. Optical properties (absorption and reduced scattering coefficients) of solutions and tissue phantoms containing carbon nanotubes were measured with spectrophotometry and determined by the inverse adding doubling (IAD) method. Inclusion of CNTs in phantoms increased light absorption with minimal effect on scattering and anisotropy. Light absorption of MWNTs was found to be higher than SWNTs and SWNHs.

The photochemical response to laser irradiation (wavelength 1064 nm) of CNTs was measured with spin-trap electron paramagnetic resonance (EPR) spectroscopy. Only SWNHs appeared to produce significant levels of ROS production in response to laser excitation in the presence of NADH. We detected the predominant presence of trapped hydroxyl radical (•OH) with a trace of the trapped super oxide ($O_2^{\bullet -}$) radical. These free radicals are highly reactive and could be utilized to cause targeted toxicity to cancer cells.

The distribution of CNTs at the cellular level, in phantoms, and in kidney tumors was measured using transmission electron microscopy (TEM) imaging. Samples were imaged following various time periods (2-48h) of incubation and CNTs were observed inside the cell

cytoplasm, nucleus, vacuole, and outside cells for the above mentioned time periods. CNTs in phantoms and tumor tissue were randomly and uniformly distributed in the entire volume. Computational model geometries were developed based on CNTs distribution in cells, tissue phantoms, and kidney tumor tissue.

In the computational part of this research the temperature response to laser irradiation alone or with CNT inclusion was determined using Penne's bioheat equation which was solved by finite element methods. Experimentally measured thermal conductivity and absorption and reduced scattering coefficients were used as input parameters in Penne's bioheat equation. The accuracy of the model predicted temperature distribution was determined by comparing it to experimentally measured temperature in tissue phantoms and kidney tumors following CNT inclusion and laser therapy. The model determined temperature distribution was in close correspondence with the experimentally measured temperature. Our computational model can predict the effectiveness of laser cancer therapy by predicting the transient temperature distribution.

Acknowledgements

I would like to express gratitude to my supervisor Dr. Marissa Nichole Rylander, for her kind support, guidance, and supervision throughout my entire PhD program. I am also thankful to my PhD committee Dr. James Mahaney, Dr. Christopher G. Rylander, Dr. Thomas E. Diller, Dr. Harry Dorn, Dr. Suzy Torti, and Dr. Scott T. Huxtable for supporting me in various projects and guiding my research to successful completion. I am grateful to my lab mates who also helped me in many ways during my research.

This research was funded by the following sources: National Science Foundation Grant CBET 0731108, National Institute of Health Grant 1 R21 CA135230-01, and an Institute for Critical Technology and Applied (ICTAS, Virginia Tech) Science Grant. We would also like to thank Dr. David Geohegan from Oak Ridge National Laboratories for his kind gift of the single walled carbon nanohorns.

I am always grateful to almighty God, my parents, and my beloved wife who helped me through every step in my life and brought me to this stage to complete my PhD successfully.

Contents

List of Figures

List of Tables

Chapter 1: Introduction and Background

1.1. Motivation

More than 1.47×10^6 million men and women have been diagnosed with cancer and over 562,000 people have died of this disease within the United States in 2009 [1].Thermally based treatments for cancer include thermal ablation (high temperature, T>55^{o}C, based tissue coagulative treatments), local hyperthermia (lower temperature, T~42-44^{o}C), hyperthermia sensitization as an adjuvant to radiotherapy, chemotherapy, or brachytherapy, and thermally mediated drug or gene deliveries. The effectiveness of hyperthermia therapies such as laser treatment is limited due to nonspecific heating of target tissue and diffusion limited thermal deposition which often leads to healthy tissue injury and extended treatment durations. Laser therapies can be further compromised due to induction of molecular chaperones called heat shock proteins (HSPs) in tumor regions where non-lethal temperature elevation occurs. HSP up-regulation in cancer cells can lead to enhanced tumor cell viability and tumor recurrence by mitigating apoptosis [2-4] and providing resistance to subsequent chemotherapy and radiation treatments which are typically used in combination with the initial hyperthermia treatment [2,5-14]. Therefore, more effective laser therapy may be achieved through increased thermal deposition, improved heating selectivity, reduced treatment times and thermal doses, confined tumor injury, and elimination of HSP expression in the tumor. Incorporating carbon nanotubes (CNTs) in the tumor has the potential to achieve the previously mentioned objectives for improved cancer treatment. CNTs possess significantly high thermal conductivity and light absorbing ability. Incorporating CNTs into tissue enhances the light absorbing capabilities and thermal conductivity of tissue, thereby generating more heat (by absorbing more laser light) in the tissue and delivering more heat (by increasing thermal conductivity) to the targeted tissue volume during laser irradiation. CNTs also generate highly reactive free radicals, called reactive oxygen species (ROS) in the presence of laser irradiation. ROS can cause damage to DNA, cell apoptosis, and damage proteins, lipids, and nucleic acids [15-16]. Therefore, CNT mediated laser therapy has a combinatorial treatment effect by generating and delivering more heat to the targeted tissue and generating highly cell damaging ROS. The combinatorial effects of CNT mediated laser therapy can produce more cell damage compared to traditional laser therapy without CNTs.

The goal of this research is to develop a comprehensive understanding of the photothermal and photochemical response associated with incorporation of CNTs in laser cancer therapy. Based on this knowledge, a novel treatment planning computational model will be created to predict the photothermal and photochemical response of tissue to CNT-mediated laser therapy. Ultimately, this model will permit optimization of the CNT-mediated laser treatment by determining the most appropriate CNT properties and laser parameters for maximum tumor destruction.

1.2. Traditional laser therapy

Laser therapy could provide a minimally invasive and potentially more effective treatment alternative to surgical resection, chemotherapy, and radiation. During laser cancer therapy, laser light is absorbed by different chromophores (hemoglobin, protein, lipid, etc) depending on the wavelength of light and converted into heat energy [17]. The heat energy generated in the tumor kills cancer cells. Near infrared (NIR, 700-1100 nm) laser is very effective in laser cancer treatment because in this optical window human skin is optically transparent and light within this spectral region has been shown to penetrate tissue at depths beyond 1.6–2.0 mm [18] with irradiance well below the threshold for normal tissue damage. At an NIR wavelength of 1064 nm light, which is clinically relevant, can penetrate skin approximately 1.65 mm [18]. At this wavelength CNTs were found to have significant light absorption which will be described in the following section. Therefore, we utilized 1064 nm wavelength laser in our study.

During laser therapy of a tumor, light propagates into tissue in different directions due to scattering, reflection, and transmission. Some light is absorbed by chromophores during its propagation which eventually generates heat. Therefore, heating is not specific to a certain region of the tumor volume in traditional laser therapy. The nonspecific heating often leads to healthy tissue injury. During the therapy maximum temperature occurs near the probe tip and heat diffusion from the irradiation area becomes very slow due to low thermal conductivity of tissue. Because of low thermal deposition in the entire tumor region heat shock protein

expression is induced which enhances tumor cell viability and recurrence of cancer cells. Therefore, it is difficult to kill a larger volume of a tumor with the traditional laser therapy.

1.3. Nanoparticles and laser therapy

Many studies were conducted to make the laser therapy more effective including incorporating light absorbing nanomaterials (Gold nanorods, Au cages, Ag, quantum dots, C_{60}, nanotubes, etc.) [19-21]. These nanomaterials absorb laser light locally and kill targeted cancer cells. However, based on our previous study [22] and other literature [23-24], carbon nanotubes were found to have greater light absorbing characteristics than the above mentioned nanoparticles because of their antenna effect.

1.4. Carbon nanotubes in Medicine

Carbon nanotubes (CNTs) are utilized in different medical applications such as drug delivery, radiotherapy, and to improve optical and MRI image contrast, cancer detection, etc. After the invention of Carbon nanotubes (CNTs) by Iijima in 1991 [25], CNTs have received significant attention for their potential role as thermal enhancers for hyperthermia and drug delivery [26-27]. CNTs are composed of graphene sheets with sp^2 bonded carbon atoms rolled seamlessly into a tubular form. The two major types of CNTs are single-walled carbon nanotubes (SWNTs) which have one seamless tube (Figure.1.1 A), and multi-walled carbon nanotubes (MWNTs) which possess two or more concentric tubes (Figure.1.1 B). The diameter and length of SWNTs are 1.5-3.0 nm and 20-1000 nm respectively whereas the corresponding dimensions for MWNTs are 5.0 -100 nm and 1-50 microns respectively [28-32]. Another unique embodiment of SWNTs are single-walled carbon nanohorns (SWNHs) which are composed of an aggregate of cone shaped SWNTs in a dahlia structure with agglomerate diameters of 50-100 nm (Figure1.1 C). Throughout many of the sections of the paper we will refer collectively to SWNT, MWNTs, and SWNHs as CNTs for brevity. Though CNTs are hydrophobic, they can be made hydrophilic in two different ways, i.e., 1) introducing a non-covalent hydrophilic layer on the surface of CNTs (using pluronic, micel, etc.), 2) functionalizing CNT surfaces with covalently attaching carboxyl (-COOH) and hydroxyl (-OH) ion. CNTs can be functionalized with MRI contrast agents like Gd, Fe, and Lu (by making peapods) and optical imaging contrast agents such as quantum dots (QDs), Au, and Ag in order to improve MRI and optical image contrast respectively. A peapod is made when an endohedral metallo fullerine (an atom/ion or

cluster of atoms/ions are encapsulated into C60, C70, and C80) is inserted in CNTs (Figure 1.1D). It was found that peapods with Gd atoms improve MRI contrast 40 folds than Gd alone. CNTs can be functionalized with anticancer drugs for chemotherapy. They are also used to target specific cancer cells by functionalizing CNT surface with appropriate antibodies which have high affinity for over-expressed proteins of that cancer cells.

CNT structures possess extraordinary ability to absorb large amount of electromagnetic signals in the near infrared region (NIR) (700-1100 nm) leading to considerable heat generation and permitting tumor cell destruction [23-24,33]. Light within this spectral region has been shown to penetrate human skin at depths beyond 1.6-2 mm [18]. Since skin is optically transparent to this light, CNTs that are contained in a tumor remain capable of absorbing light and producing heat. The length of CNTs has considerable impact on its ability to absorb light. For a specific frequency of the incident electromagnetic signal, efficient light absorption occurs when the length of the CNT is at least half the wavelength of the incident light based on antenna theory [34-37]. Our CNT lengths for this study were chosen to be 900 nm-1200 nm, which are suitable for significant light absorption in the NIR. In addition to length, the presence of metallic catalysts (used during the manufacturing process of CNTs), affect the efficiency of light absorption and the heat diffusion rate. Higher levels of metal catalysts reduce light absorption capacity and thermal conductivity of CNTs in tissue because of less CNTs per unit mass [38].

Incorporating these CNTs into tissue could potentially change tissue properties and improves laser therapy. CNTs possess extraordinary electromagnetic, thermal, optical, and chemical properties. They exhibit very high thermal conductivity (3000-6000 W/m·K) measured experimentally and computationally [39-44], compared to the thermal conductivity of tissue and tumors which vary from 0.511-0.561 W/m·K [45-46]. CNTs have significant light absorbing capacity due to their antenna effect as described previously. These highly thermally conductive and light absorbing CNTs can be used to make relatively higher thermally conductive and light absorbing CNT-tissue composites compared to actual tissue. Thereby, the effectiveness of laser therapies can be greatly enhanced by introducing CNTs into the tissue prior to laser irradiation [26-27].

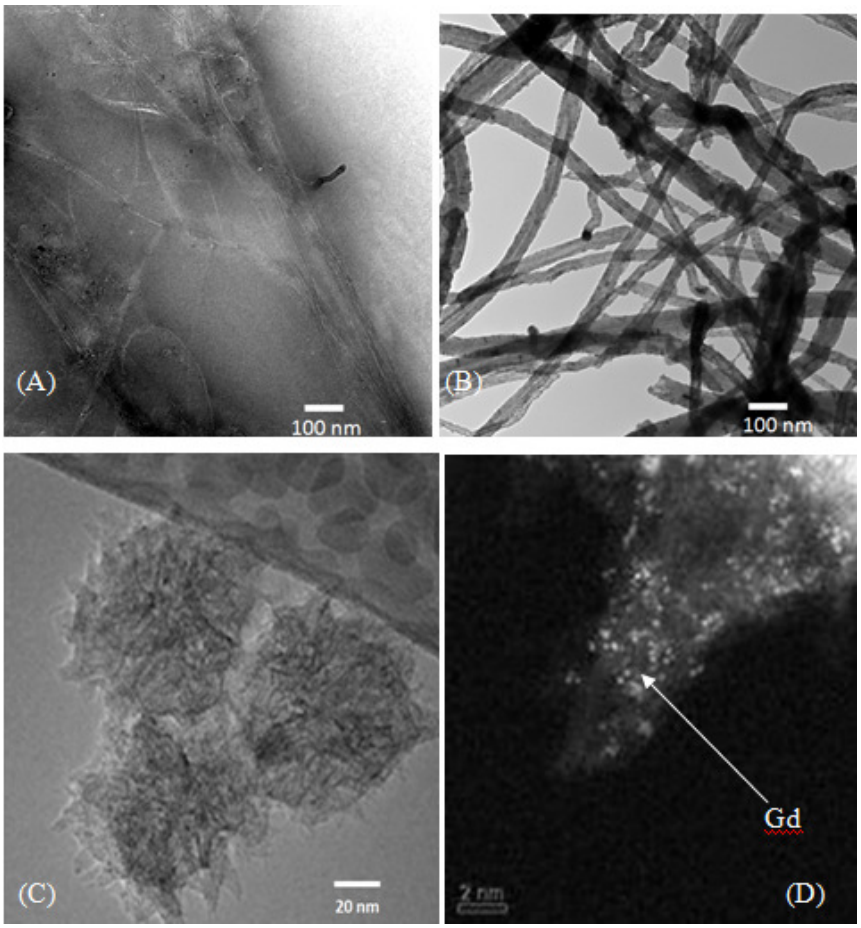

Figure 1.1: (A), (B), and (C) are the SWNT, MWNT, CNH, and peapods respectively

1.4.1. Selection of CNTs

Although SWNTs, SWNHs, and MWNTs greatly enhance the effectiveness of laser therapy due to their ability to act as antenna for electromagnetic energy, the antenna properties of MWNTs have been documented to be superior to SWNTs. MWNTs can absorb approximately 3/4 times the light of SWNTs in irradiated skin and subcutaneous tissue by NIR laser light [24,38]. Because of the larger diameter of MWNTs compared to SWNTs and SWNHs, it is expected that MWNT-composites will have higher thermal conductivity than that of SWNT-composite and SWNH- composites [47]. However, the presence of metallic catalysts used during manufacture of CNTs affect the efficiency of light absorption and heat diffusion. Higher levels of metal catalysts reduce light absorption capacity and thermal conductivity of CNTs, because

there are less CNTs per unit mass [38]. MWNTs and SWNTs require metal catalysts during their manufacturing process which are very difficult to remove even after several purification processes. However, SWNHs do not require any metal catalyst during their manufacturing process and can be produced from pure graphite, which results in SWNHs without any metal impurities. Therefore, an appropriate selection of CNTs is very important in our research to achieve CNTs with ideal absorption characteristics and thermal conductivity to receive maximum benefit for their inclusion in laser therapy.

1.5. Photothermal effect

During laser treatment of tumors with CNTs, a significant amount of laser light will be absorbed by CNTs and converted into heat energy. The amount of light absorbed and the amount of heat diffused out in a tumor volume will depend on optical and thermal properties of tissue-CNT composites. However, the optical and thermal properties of tissues containing CNTs in the form of SWNHs, MWNTs, and SWNHs have not been investigated. Optical and thermal properties are critical inputs for the computational model for predicting photothermal response to nanoparticle inclusion in laser therapy. The traditional Penne's bioheat transfer equation [48] will be utilized to determine the temperature response and this computational prediction will be compared with experimentally measured temperature during and following laser irradiation of tissue phantoms and mice tumors.

1.5.1. Measurement of thermal conductivity

Thermal conductivity of human and animal tissues (except liver tissue) vary from 0.5 W/m·K to 0.58 W/m·K [49-53]. Tissue representative phantoms made of agar and sodium alginate have been used as representative tissue systems due to their similar thermal and optical properties to tissue. The thermal conductivity of agar gel phantoms (95% water content) was measured and the values were in the range of 0.576-0.585 W/m·K [54]. Due to a similar water content, the thermal conductivity of sodium alginate phantoms (97% water), animal and human tissues (>85% water) [12], and agar phantoms (95%) can be assumed to be nearly identical.

There are several methods for measuring the thermal conductivity of soft tissue and each method possesses inherent advantages and challenges. In general it is complicated to measure the

thermal conductivity of a soft tissue due to the difficulty in designing an apparatus for steady state or quasi-steady state measurement. Traditionally, thermal conductivities of soft tissues have been measured by guarded hot plates [53,55]. In this method a tissue sample is placed between two electrical heater plates at different temperatures. Heat is allowed to flow from the hotter plate to the colder plate until steady state conditions are reached at which time temperature is measured. However, the difficulty of this method in bringing the samples to steady state conditions requiring significant periods of time which leads to dehydration of the sample and corresponding changes in thermal properties. This method also requires complex solution methods involving two or three dimensional heat transfer analysis. Other techniques have been developed to measure thermal conductivity of biological samples in a more rapid manner using transient heat transfer methods. Among them, the Dual-thermistor probe method [56], which uses two thermistor beads, consisting of a heater and sensor, is placed in a sample at specific distances so that thermal diffusion can be measured accurately by the sensor. Although this method is highly invasive and not suitable for *in vivo* experiments however, it is amenable for measurement of liquid samples like blood plasma, skimmed milk, etc. Another thermal conductivity measurement alternative is the Pulse-decay method [57] which utilizes a microprobe resistor to provide several square-wave heating pulses and measures temperature decay with a sensor attached to the microprobe resistor. However, this method is complicated and difficult to construct the microprobe. It is also suitable for liquid samples and has been utilized to determine the thermal conductivity of silicon oil and glycerin.

We used a simpler and more accurate technique, called the hot wire probe method [49,52,58-59] to measure thermal conductivity of tissue representative sodium alginate phantoms containing varying CNT types (SWMTs, MWNTs, and SWNHs) and CNT concentrations (0.1 mg/ml, 0.5 mg/ml, and 1.0 mg/ml). This method is minimally invasive and considers transient heat diffusion analysis to compute thermal conductivity. A single line heat source, called a hot wire probe acts as a heater and temperature sensor allowing measurement of the time dependent temperature response from the surface of the heater probe (Figure 1.2). In Figure 1.2 a hotwire probe is inserted into a tissue sample and heater wire is connected to the voltage source. During voltage supply time dependent temperature data was collected with a thermocouple connected to data acquisition system.

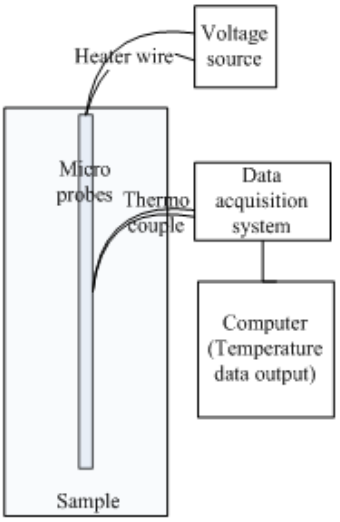

Figure 1.2: Schematic diagram of the experiment

This method requires minimal experimental setup and less time to measure temperature response and thermal conductivity. Therefore little water content is removed from samples and thermal properties are unchanged during the experiment. In this method, the samples are made considerably long with a high aspect ratio (the sample is considered infinitely long), so that any axial heat flow is negligible and only heat flow occurs in the radial direction. Therefore 1-dimentional (1-D) radial heat transfer is only considered in the analysis. The governing equation used for this method is described below.

$$\frac{\partial^2 T}{\partial r^2} + \frac{1}{r}\frac{\partial T}{\partial r} = \frac{1}{\alpha}\frac{\partial T}{\partial t} \tag{1.1}$$

Equation (1.1) is a 1-D transient heat transfer equation with cylindrical coordinates, where T is the temperature, r is the position, t is the time, and α is the thermal diffusivity. A solution of Equation 1 for thermal conductivity K is represented in Equation 1.2.

$$K = \frac{q'}{4\pi}\left(\frac{dT}{d\ln(t)}\right)^{-1} \tag{1.2}$$

If the slope $\frac{dT}{d\ln(t)}$ and heat source q' is known, K can be measured from Equation 1.2.

1.5.2. Measurement of optical properties

The optical properties (attenuation, absorption, scattering, and anisotropy coefficients) of tissue can be measured with a spectrophotometer. However this method is an indirect method,

because spectrophotometer only measures diffuse transmittance, collimated transmittance, and reflectance. These parameters are used as input parameters to solve the radiative transport equation inversely [17] to calculate absorption, scattering, and anisotropic coefficients. In order to solve the radiative transport equation another input parameter, refractive index, is essential. The refractive index can be measured with optical coherence tomography (OCT) [60] and the envelope-extremes location technique [61]. In our research we used OCT to measure refractive index (ratio of the light velocity in vacuum to the velocity in the medium) of tissue phantoms.

Different computational techniques are used to solve radiative transport equation inversely in order to compute absorption, scattering, and anisotropy coefficients. The Kubelka-Munk approach [62] can be used to calculate absorption and scattering coefficients from total diffuse reflection, however this method is limited due to lack of accuracy. The Inverse Monte Carlo method [63-65] requires large computing time to minimize signals to noise ratio and is often difficult to converge. On the other hand, the IAD method [66] is very accurate and computing time is very rapid. This method is capable of calculating absorption, scattering, and anisotropy coefficients making this method very popular. We utilized the IAD method for optical property determination in this study.

1.5.2.1. Spectrophotometry

While measuring transmittance and reflectance with the spectrophotometer, ballistic-light intensity I_0 should be measured for 100% transmission and 100% reflection to obtain a baseline in the absence of a sample and with a presence of standard reflecting sample respectively. Sample light intensity, I_s is measured to determine transmittance, reflectance, and absorbance, depending on position of the sample in the DRA (Figures 1.3 A-E). 100% transmission (T100%) is measured in the absence of a sample at the sample port (Figure 1.3 A). 100% reflectance (R100%) is measured for a standard reflecting sample at the reflection port (Figure 1.3 C). Transmittance (Ts) (Figure 1.3 B) and reflectance (Rs) (Figure 1.3 D) are measured by placing the sample at the transmittance and reflectance ports of the integrating sphere. Samples are mounted in the middle of the integrating sphere to measure absorbance (Figure 1.3 E).

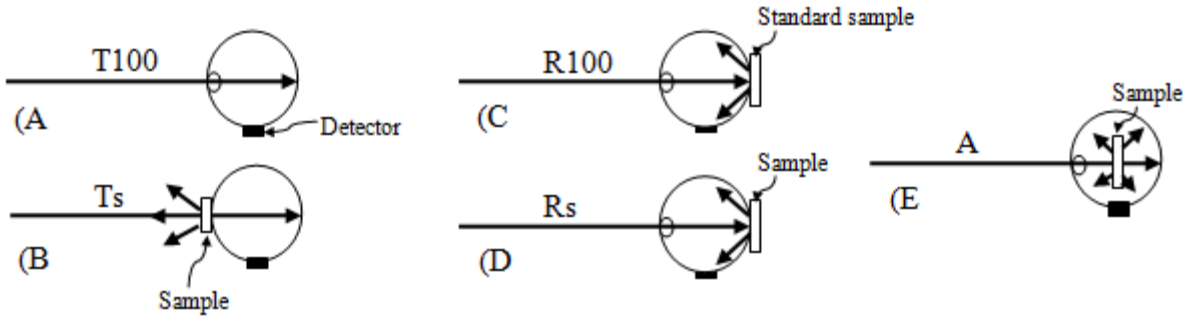

Figure 1.3: Sample position in the DRA in order to measure transmittance, reflectance, and absorbance

1.5.2.2. Optical Coherence Tomography (OCT)

OCT can be used to determine refractive index of tissue phantoms with CNT inclusion. OCT is a ballistic optical imaging technique [60]. OCT can be used to measure refractive index for any solid or liquid sample. With this technique a monochrome light source emits a horizontal source beam to a diagonally inclined beam splitter. The beam splitter splits the source beam into two parts. One part is reflected away by the beam-splitter and then reflected back by a reference mirror. Another part is transmitted through the beam splitter and reflected back by an object surface. These two back-reflected beams are combined in the beam-splitter and received by a detector.

Knowledge of the composite optical properties of solutions and tissue phantoms with CNT inclusion will assist with selection and prediction of tissue response to nanoparticle-mediated laser therapies.

1.5.2.3. Inverse adding-doubling (IAD) method

The IAD technique can be used to calculate the absorption and reduced scattering coefficients for tissues. This method determines optical properties by inverse calculation of the radiative transport equation [17], where samples require homogenous optical properties with infinite plane parallel slabs. During computation, this method assumes a set of initial values of albedo (a'), optical thickness (b'), and sample thickness (δ) [17,66]. These optical properties are expressed in terms of absorption, scattering and anisotropy coefficients. The initial values

calculate absorption, scattering, and anisotropy coefficients. It also calculates transmittance and reflectance as well as compares the values with the corresponding experimentally measured parameters. If the values are not identical, it assumes a new set of values for optical parameters. The process continues until the calculated reflectance and transmittance values are identical to the experimental values.

1.6. Photochemical effect

When excited by laser light many types of fullerenes (C_{60}, C_{70}, C_{76}, C_{80}, C_{84}, and endohedral fullerenes) have been shown to generate reactive oxygen species (ROS) [67-70]. Therefore, there is a potential for CNTs to generate ROS during laser irradiation. Introducing CNTs in tumors can enhance the efficiency of the laser surgery by depositing more heat and potentially generating ROS. ROS normally exists in all aerobic cells in balance with biochemical antioxidants. ROS can cause damage to DNA, cell apoptosis, and damage proteins, lipids, and nucleic acids leading to cell death. Our hypothesis is that laser-activated CNTs could effectively generate ROS and heat in response to laser excitation, permitting a multimodal therapeutic tool.

1.6.1. Free radicals and Reactive Oxygen Species (ROS)

A free radical is an atom (e.g. oxygen, nitrogen) with at least one unpaired electron in the outermost shell [71]. Due to the presence of unpaired electrons, they are highly reactive. There are numerous types of free radicals and we are particularly interested in oxygen centered free radicals or reactive oxygen species (ROS). The most common ROS are the superoxide anion (O_2^-), the hydroxyl radical (-OH), and hydrogen peroxide (H_2O_2). Superoxide anions are formed when an oxygen molecule (O_2) receives an additional electron and forms a molecule with only one unpaired electron. ROS form in human cells as a natural byproduct of the metabolism of oxygen. Super oxide anion (O_2^-) is continuously formed in the mitochondria. The rate of formation depends on the amount of oxygen flowing through the mitochondria at any given time. During any environmental stress (laser light or heat exposure) ROS levels increase dramatically, which result in significant damage to cell structures. This situation is known as oxidative stress [71]. Compared to super oxide and hydrogen peroxide, hydroxyl radicals are short-lived radicals, but are the most damaging radicals to cells [72].

1.6.2. Electron Paramagnetic Resonance (EPR)

The presence of ROS can be detected by Electron Paramagnetic Resonance (EPR). EPR is a spectroscopic technique and a very robust method for detecting free radicals by measuring unpaired electrons. This method is also known as Electron Spin Resonance (ESR). An unpaired electron can behave as a small magnet with an electron spin of either $+1/2$ or $-1/2$ direction. If the electron is exposed to an external magnetic field it can align itself either parallel or anti-parallel to that field and create two possible energy levels, which vary with magnetic field strength. If electromagnetic radiation of the correct energy is applied, where the radiation frequency is very close to the natural frequency of the unpaired electron, resonance takes place. In this case, energy (in the form of microwave energy) will be absorbed by electrons at a lower energy level and electron will move from the lower to a higher energy level. Thus absorption spectra are obtained [16]. The absorption spectrum is unique for a specific ROS. Therefore, a ROS can be identified by analyzing EPR absorption spectrum.

1.6.3. Spin trapping

ROS are highly unstable in nature. To stabilize the free radical species for measurement, spin trapping agents must be used. In this method, an unstable free radical reacts with a diamagnetic molecule, called a spin trap, to form a relatively stable free radical. There are two types of free radicals, i.e., Nitroso, and Nitrones [16]. For nitroso traps, the radical detected adds directly to the nitrogen, whereas with nitrones, it adds to the adjacent carbon. For nitroso traps, the trapped radical thus more easily influences the EPR spectrum and usually generate hyperfine splitting, whereas with nitrone traps the EPR spectra tend to be broadly similar for all types of free radicals. However, nitroso compounds often give less stable adducts compared to nitrones, especially when oxygen radicals are trapped and tend to be more toxic to living cells. Hence nitrones are more commonly used. We used spin trap in this research: 5,5-dimethyl-1-pyrroline *N*-oxide (DMPO) which belong to the nitrones group. Reaction of spintrap (R-NO) compounds with short lived radicals ($R^{\cdot *}$) can produce longer-lived nitroxide radicals [16]. The reaction is shown below,

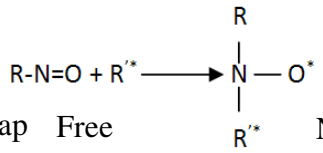

Spintraps are used to detect O_2^-, -OH, $^1O_2$, and H_2O_2. DMPO reacts with –OH, and O_2^- to form products (DMPO-OH, and DMPO-OOH respectively) with EPR spectra. DMPO has a higher affinity for –OH compared to O_2^-. Thus at equal concentrations of radicals –OH is trapped much faster than O_2^-. Hence efficient trapping of O_2^- requires high DMPO concentrations. However, DMPO with O_2^- is unstable and decomposes into DMPO-OH, the same product generated directly from –OH. For this reason, it is often difficult to detect the presence of O_2^- with DMPO.

1.7. Distribution study of CNTs in vivo and in vitro

In order to develop a computational model of CNT mediated laser cancer therapy, it is crucial to know the actual distribution of CNTs in tissue. Incorporating CNTs in tissue changes its thermal and optical properties. Variations in CNT distribution will also affect the temperature profile in the tissue following laser irradiation. Therefore, it is very important to know the actual distribution of CNTs in the tissue to create a realistic computational model of a tumor, where tissue properties will depend on the CNT distribution in the actual tissue.

Previous literature has measured CNT distribution in cells [26,73-77]. Liu *et al.* described the distribution of SWNTs in various organs of mice functionalized with radioactive materials (tracer materials), where Raman signature gave a quantitative analysis of SWNTs in different organs for specific times [77]. Nancy *et al.* measured the interaction of MWNTs in human epidermal cells *in vitro* for various incubation periods using TEM imaging [74]. The TEM images showed the presence of MWNTs in cell vacuoles. However, they did not describe the presence of MWNTs in other parts of the cell such as the cell nucleus, membranes, cytoplasm, etc. Kam *et al.* described the presence of SWNTs in Hipco cells after labeling SWNTs with a fluorescent tag [26]. His confocal microscopic images showed several SWNTs were present around the cell nucleus. Cheng et al. measured the distribution and toxicity of unpure and pure MWNTs in human macrophage cells using TEM imaging. In this study, TEM imaging was utilized to measure the cellular uptake of MWNTs. MWNTs were observed in cell membrane and vacuole after 4 hrs and 4 days [73].

The CNT distribution in human and animal tissue depends on the mass transport through the complex structure of tissue. A tissue domain is composed of extracellular matrix of skin and connecting tissues primarily consisting of collagen, which forms a fibrous network created and maintained by fibroblast with various alignment angles. When CNTs are introduced to the tissue domain, they will be aligned according to local tissue structure. In our CNT distribution study we have measured the distribution of MWNTs in tissue phantom, cancer cells, and mice tumors by TEM image analysis at different times. This measurement gave us an idea about the position and distribution of MWNTs in cells. Based on the distribution study of CNTs we developed a computational model of tumors in which optical and thermal properties are the input parameters.

1.8. Computational Model

Despite the promise of nanotube-mediated laser therapies, treatment planning models are necessary to determine optimal CNT properties and laser parameters to effectively cause targeted tumor destruction. However, no prior studies have investigated the absorption and thermally conductive properties of CNTs for cancer treatment. Therefore, in this research we compared the properties of SWNTs, MWNTs, and SWNHs for their potential use in laser therapy [78-79].

Typically people use Penne's bioheat equation [48] to make a computational model of laser cancer therapy and predict temperature distribution in the model. Penne's bioheat equation is a transient heat transfer equation which incorporates expressions for the thermal effects of local blood perfusion and laser energy absorption represented in Equation 1.3.

$$\rho_t c_t \frac{\partial T}{\partial t} = \nabla \cdot [k(T)\nabla T] - \omega_b(T) c_b (T - T_a) + Q(\vec{r}, t) \tag{1.3}$$

where ρ_t , c_t , T_a, and c_b are the density and specific heat of the tissue, arterial blood temperature, and specific heat of the blood, respectively. The temperature dependent blood perfusion rate within the tumor is denoted as ω_b and is represented in Equation 1.4 [80].

$$\omega_b = \begin{Bmatrix} 0.833 & T < 37 \\ 0.833 - (T-37)^{4.8} / 5.438 \times 10^3 & 37 \le T \le 42 \\ 0.416 & T > 42 \end{Bmatrix}, \text{kg/s.m}^3 \quad (1.4)$$

Computational models have been developed by others using Penne's equation to predict tissue response to laser irradiation [81-84]. Previously few treatment planning models developed for prostate cancer laser therapy were capable of predicting and optimizing temperature, thermal injury, and HSP expression based on measured data [12,85-87]. They accurately predicted temperature distribution in the tumor model which was close to MRTI temperature data [87-90].

However, existing models of photothermal heating of tissue embedded with nanoparticles is limited. Penne's bio heat equation can predict temperature response accurately if the material properties of tissue-nanoparticle composites (absorption coefficient, thermal conductivity, etc) are known. However these composite properties are not available in current literatures. Therefore measurement of light absorption coefficients and thermal conductivity is mandatory prior to use the Penne's equation in a computational model of tisuue-nanoparticle. In order to model a CNT mediated laser cancer therapy the above composite properties are need to be measured accurately. Our research will develop a new treatment planning model for predicting the thermal response to inclusion of appropriate CNTs in laser therapy.

Chapter 2: Overall Goal

Our overall strategy for development of the treatment planning model with combinatorial photothermal and photochemical effects will be based on both experimental measurements and computational methods which are summarized in Figure 2.1.

2.1. Experimental goal

The CNT distribution will be determined using transmission electron microscopy (TEM) imaging and will provide the basis for defining the finite element system geometry of the phantom containing CNTs for our computational model. Thermal properties of CNT-Tissue composites will be measured by hot wire probe method. Optical properties of solutions and phantoms containing CNTs will be measured using a spectrophotometer and inverse adding doubling (IAD) method. Reactive oxygen species (ROS) of solutions containing CNTs will be measured during laser irradiation using Electron paramagnetic resonance (EPR) spectroscopy.

2.2. Computational goal

The measured optical properties will be utilized as inputs to a Penne's bioheat equation [48] and Monte Carlo model to solve the light transport equation for determination of the fluence distribution. The fluence distribution will be used to calculate the laser heat sources term for the heat transfer model. The calculated heat source and thermal conductivity will be used as input parameters to solve the bioheat transfer equation to deduce temperature distribution in the phantom following laser irradiation. The model predicted temperature response associated with laser irradiation of phantoms containing CNTs will be compared to the experimentally measured temperature distribution for model validation.

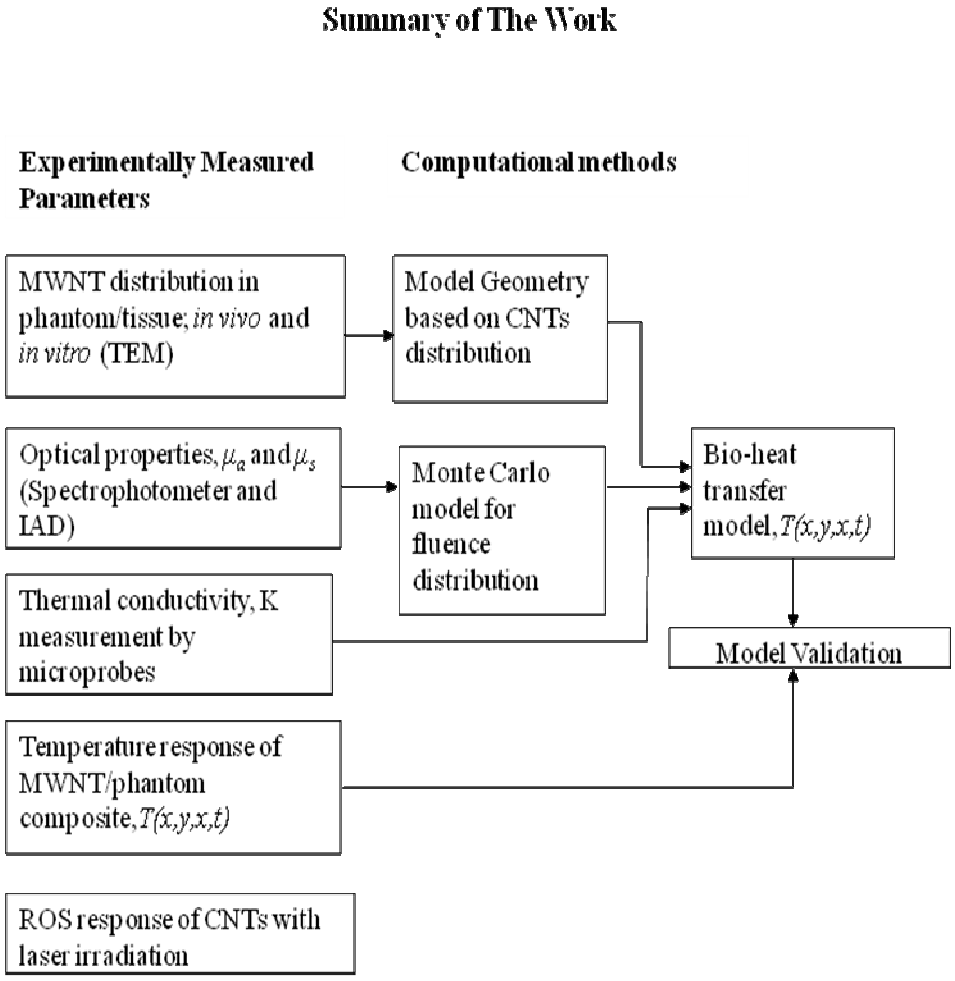

Figure 2.1: Over all summery of the project

Chapter 3: Outline of the project

The project specific aims are divided into three categories

1. Specific Aim 1: Measure photothermal response to CNT inclusion in laser therapy
    - Measure thermal properties of tissue phantoms containing varying CNT types (SWNT, MWNT, and SWNH) and concentrations.
    - Measure optical properties of solutions and tissue phantoms containing varying CNT types (SWNT, MWNT, and SWNH) and concentrations.
2. Specific Aim 2: Characterize cellular uptake and distribution of CNTs
    - Measure intracellular uptake of CNTs of varying types (SWNT, MWNT, and SWNH) and concentrations
    - Measure CNT distribution in tissue phantoms, cancer cells, and mice tumors
3. Specific Aim 3: Measure phototchemical response to CNT inclusion in laser therapy
    - Measure reactive oxygen species (ROS) in solutions containing varying CNT types (SWNT, MWNT, and SWNH) and concentrations alone or in combination with laser irradiation
4. Specific Aim 4: Develop a computational model for predicting photothermal response for CNT-laser therapy planning.
    - Develop model for photothermal response

3.1. Specific Aim 1: Photothermal effect of CNT mediated laser cancer therapy

Our first aim is to measure thermal and optical properties of nanotube-tissue composites. Previous literature has measured optical and thermal properties of human and animal tissue and several types of nanoparticles in solution [49,52,64,91-92]. However, the optical and thermal properties of tissues containing CNTs in the form of SWNHs, MWNTs, and SWNHs have not been investigated. Optical and thermal properties are critical inputs for the computational model

for predicting photothermal response to nanoparticle inclusion in laser therapy. The traditional Penne's bioheat transfer equation [48] will be utilized to determine the temperature response and this computational prediction will be compared with experimentally measured temperature during and following laser irradiation of tissue phantoms and mice tumors. Measurement of thermal properties of CNT-Tissue composites will be discussed in chapter 4 and measurement of optical properties will be described in chapter 5. An overview of photothermal response of MWNTs mediated laser therapy was discussed in chapter 6.

3.2. Specific Aim 2: Time dependent Cellular uptake and distribution study of CNTs

The second aim is to study the distribution of CNTs in tissue phantom, cancer cells, and mice tumors. Knowledge of CNT distribution is critical to predicting the heat source distribution. Based on the distribution of CNTs in tissue, optical and thermal properties of CNT-tissue composite varies. In order to know the actual distribution of CNTs in tumor, several time dependent measurements will be conducted: cellular uptake of CNTs, transport of CNTs in tissue phantoms, and CNT distribution in mouse tumors as described in chapter 8.

3.3. Specific Aim 3: Photochemical effects of CNT mediated laser cancer therapy

The third aim involves measuring the photochemical response of CNTs of varying type and concentration before and following laser irradiation. Different fullerenes (C_{60}, C_{70}, C_{76}, C_{80}, C_{84}, and endohedral fullerenes) have been shown to generate reactive oxygen species (ROS) in prior literature [15,67,69]. It is expected that SWNTs, MWNTs, SWNHs, Peapods will generate ROS when they are irradiated with a laser. ROS can damage DNA and targeted cell apoptosis providing another mechanism for tumor cell destruction. We will identify the best CNTs in terms of ROS generation during laser irradiation. Photochemical response of CNTs before and following laser irradiation is described in chapter 7.

3.4. Specific Aim 4: Computational model of CNT mediated laser cancer therapy

A computational model of CNT mediated laser cancer therapy was developed and will be discussed in chapter 9. This model will be developed based on CNT distribution described in chapter 8 and experimental model of phantom/tumor. A model for predicting the photothermal response to laser irradiation of CNTs will be created, where thermal and optical properties

measured in chapters 4 and 5 will serve as inputs. The computational model will be compared with the experimental models of phantom and tumor in order to validate the computational model.

Chapter 4: Photothermal effects

The following article was submitted in the **Annals of biomedical engineering** for publication. The article was written based on the format of above mentioned journal.

Measurement of thermal conductivity of carbon nanotube-tissue phantom composites with hot wire probe method

Saugata Sarkar[1] and Marissa Nichole Rylander[1, 2]

[1]Department of Mechanical Engineering
Virginia Polytechnic Institute and State University
ICTAS Building, Stanger Street, MC0298
Blacksburg, Virginia 24061

[2]School of Biomedical Engineering and Sciences
Virginia Tech-Wake Forrest University
ICTAS Building, Stanger Street, MC0298
Blacksburg, Virginia 24061
Corresponding author E-mail: mnr@vt.edu

4.1. Abstract

Developing combinatorial treatments involving laser irradiation and nanoparticles, requires an understanding of the effect of nanoparticle inclusion on tissue thermal properties such as thermal conductivity. This information will permit more accurate prediction of temperature distribution and tumor response following therapy and guide selection of the appropriate type and concentration of nanoparticles. This study measured the thermal conductivities of tissue representative phantoms containing varying types and concentrations of carbon nanotubes (CNTs). Multi-walled carbon nanotubes (MWNTs, length 900-1200 nm, diameter 40-60 nm), single-walled carbon nanotubes (SWNTs, length 900-1200 nm, diameter <2 nm), and a novel embodiment of SWNTs known as single-walled carbon nanohorns (SWNHs,

length 25-50 nm, diameter 3-5 nm) of varying concentrations (0.1 mg/ml, 0.5 mg/ml, and 1.0 mg/ml) were uniformly dispersed in sodium alginate tissue representative phantoms. The thermal conductivity of phantoms containing CNTs was measured using a hot wire probe method. Inclusion of CNTs in phantoms increased their thermal conductivity slightly with the level of increase dependent on CNT type and concentration. Increasing CNT concentration from 0 to 1.0 mg/ml caused the thermal conductivity of phantoms containing SWNTs, SWNHs, and MWNTs to increase by 24%, 30%, and 66% respectively. For identical CNT concentrations, phantoms containing MWNTs had the highest thermal conductivity.

Keywords thermal property, soft tissue, nanoparticle, thermal conductance, hyperthermia.

4.2. Introduction

Laser therapies can provide a minimally invasive cancer therapy alternative to surgical resection. However, their effectiveness is limited by nonspecific heating of target tissue, which can lead to healthy tissue injury. Inclusion of optically absorbing and thermally conductive nanoparticles such as carbon nanotubes (CNTs) in laser therapy has the potential to enhance optical absorption leading to improved heat generation and tumor destruction. Furthermore, integration of highly thermally conductive CNTs can enhance the overall thermal conductivity of the tissue composite thereby increasing thermal diffusion within the tissue and allowing treatment of larger tumor volumes. CNTs have received significant attention for their potential role as thermal enhancers for laser ablation and drug delivery [26-27]. They are composed of graphene sheets with sp^2 bonded carbon atoms rolled seamlessly into a tubular form. The two major types of CNTs are SWNTs which have one seamless tube and MWNTs which possess two or more concentric tubes. The diameter and length of SWNTs are 1.5-3.0 nm and 20-1000 nm respectively whereas the corresponding dimensions are 5.0 -100 nm and 1-50 μm for MWNTs [28,31-32,93]. Another unique embodiment of SWNTs are single-walled carbon nanohorns (SWNHs) which are composed of an aggregate of SWNTs in a dahlia shape with agglomerate diameters of 50-100 nm [94-95]. Throughout many of the sections of the paper we will refer collectively to SWNT, MWNTs, and SWNHs as CNTs for brevity. All of the previously mentioned CNT structures possess significant ability to absorb electromagnetic signals in the near infrared region (NIR) (700-1100 nm) leading to considerable heat generation and permitting tumor cell destruction [22-24,31,33,96-97]. NIR light is transmitted through tissue such as the skin with scattering-limited attenuation and minimal heating. Light within this spectral region

has been shown to penetrate tissue at depths beyond 1.6–2.0 mm with irradiance well below the threshold for normal tissue damage[18]. Previous studies have shown excitation of CNTs with a laser wavelength of 1064 nm, known to possess clinical relevance due to estimated light penetration depth of several millimeters, to cause significant light absorption, associated heat generation, and tumor cell killing[22-24]. Previous literature has also measured the absorbance of various nanoparticles (C_{60}, nanoshell, gold nanorods, etc.)[19-21]. Based on work by our group and other researchers, CNTs have been shown to possess greater capability for optical absorption compared to other fullerenes (e.g. C_{60}) and gold nanoshells/nanorods due to their exceptional antenna properties [21-24].

CNTs possess extraordinary electromagnetic, thermal, optical, and chemical properties. They exhibit very high thermal conductivity (3000-6000 W/m·K) measured experimentally and determined computationally [39,41-44] compared to the thermal conductivity of tissue and tumors which vary from 0.511-0.561 W/m·K [45-46]. Therefore, inclusion of CNTs into the tissue can potentially enhance the overall thermal conductivity of the tissue composite. It is anticipated that varying the CNT type and concentration will have a significant impact on the measured composite thermal conductivity. Selection of an appropriate type of CNT and concentration could dramatically enhance the overall thermal conductivity of the tissue and ultimate heat diffusion properties following laser heating. However, the impact of CNT inclusion on the overall tissue thermal conductivity is unknown and is critical to determining the associated heat diffusion in tissue following laser excitation. A more comprehensive understanding of the impact of CNT inclusion on the overall tissue thermal conductivity would enable better prediction of the size of the treatment volume following therapy. Ultimately, this knowledge would enable tuning of laser parameters (e.g. laser irradiance and duration) and selection of CNT properties (e.g. length, concentration) to achieve better correspondence between treated region and desired therapy margins. Treatment planning models can be utilized for designing laser therapies incorporating CNTs, but effective prediction and optimization of tissue response require knowledge of the appropriate input thermal properties such as thermal conductivity.

Several studies have characterized the effect of thermal conductivity at the CNT-liquid interface. For these studies the interfacial thermal conductance between CNTs and liquid solvents [98-99] was measured. Interfacial thermal conductance is defined as

$q'' = -U \cdot \Delta T = -\Delta T / R''$ where q'' is the heat flux, ΔT is the temperature difference, U is the interfacial thermal conductance, and R'' is the interfacial thermal resistance. The interfacial thermal conductance is the inverse of interfacial thermal resistance. Interfacial conductance is a measure of the interfacial resistance between the nanoparticle and its surrounding. Huxtable *et al* used picosecond transient absorption to measure the interfacial thermal conductance of CNTs suspended in surfactant micelles in water [99]. They determined the CNT composite thermal conductivity was limited by exceptionally small interfacial thermal conductance (G=12 $MW \cdot m^{-2} \cdot K^{-1}$). Merabia *et al* described the interfacial thermal conductance of gold nanoparticles in octane and in water by Molecular dynamics (MD) [98]. For this case, interfacial thermal conductance was determined to be 50 $MW \cdot m^{-2} \cdot K^{-1}$ to 100 $MW \cdot m^{-2} \cdot K^{-1}$ in octane and 150 $MW \cdot m^{-2} \cdot K^{-1}$ to 170 $MW \cdot m^{-2} \cdot K^{-1}$ in water for power ranges of 150 nW to 700 nW. Extremely small interfacial thermal conductance relates to very high interfacial thermal resistance, which plays an important role in the overall thermal conductivity of the CNT composite. Based on the above studies a hypothesis can be made that large interfacial thermal resistance will drastically reduce the overall thermal conductivity of the CNT-tissue composite compared to the intrinsic thermal conductivity of the CNT. Nan *et al*, Bryning *et al*, Clancy *et al*, and Gao *et al* also calculated overall thermal conductivity of CNT composites computationally by Effective Medium Approach (EMA) [47,100-103]. This approach describes the effect of thermal conductivity of a composite with and without interfacial thermal resistance. They concluded interfacial thermal resistance reduced the overall thermal conductivity of CNT composites significantly as compared to the CNT composite without interfacial thermal resistance. However, when the CNT formed a perfect interface with a polymer matrix, the interfacial thermal resistance was negligible and the overall thermal conductivity of the CNT composite was increased 5 to 20 times (depends on diameters and aspect ratio) as compared to the thermal conductivity with the presence of interfacial thermal resistance [47].

Previous literature has measured the thermal conductivity of human and animal tissues varying from 0.5 W/m·K to 0.58 W/m·K [49-53]. Tissue representative phantoms made of agar and sodium alginate have been used for representative tissue systems due to their similar thermal and optical properties to tissue. The thermal conductivity of agar gel phantoms (95% water content) has been measured and the values were in the range of 0.576-0.585 W/m·K [54]. Due to a similar water content, the thermal conductivity of sodium alginate phantoms (97% water),

animal and human tissues (>85% water) [12], and agar phantoms (95%) can be assumed to be nearly identical. However, no prior studies have measured the overall thermal conductivity of tissues with inclusion of CNTs. Therefore little is known regarding the true impact of CNT inclusion on the overall heat diffusion properties of a tissue matrix.

There are several methods for measuring the thermal conductivity of soft tissue and each method possesses inherent advantages and challenges. In general it is difficult to measure the thermal conductivity of a soft tissue due to the difficulty in designing an apparatus for steady state or quasi-steady state measurement. Traditionally, thermal conductivities of soft tissues have been measured by guarded hot plates [53,55]. In this method a tissue sample is placed between two electrical heater plates at different temperatures. Heat is allowed to flow from the hotter plate to the colder plate until steady state conditions are reached at which time temperature is measured. However, this method has difficulty in bringing the samples to steady state conditions requiring significant periods of time which leads to dehydration of the sample and corresponding changes in thermal properties. This method also requires complex solution methods involving two or three dimensional heat transfer analysis. Other techniques have been developed to measure thermal conductivity of biological samples in a more rapid manner using transient heat transfer methods. Among them, the Dual-thermistor probe method [56], which uses two thermistor beads, consisting of a heater and sensor, can be placed in a sample at specific distances so that thermal diffusion can be measured accurately by the sensor. This method is highly invasive and not suitable for *in vivo* experiments however this method is amenable for measurement of liquid samples like blood plasma, skimmed milk, etc. Another thermal conductivity measurement alternative is the Pulse-decay method [57] which utilizes a microprobe resistor to provide several square-wave heating pulses and the temperature decay is measured with a sensor attached to the microprobe resistor. This method is complicated and difficult to construct the microprobe. This method is also suitable for liquid samples and has been utilized to determine the thermal conductivity of silicon oil and glycerin.

Recently, a simpler and more accurate technique, called the hot wire probe method [49,52,58-59] has been used to measure thermal conductivity of *in vivo* and *ex vivo* samples. This method is minimally invasive and considers transient heat diffusion analysis to compute thermal conductivity. A single line heat source, called a hot wire probe acts as a heater and temperature sensor allowing measurement of the time dependent temperature response from the surface of the

heater probe. This method requires minimal experimental setup and less time to measure temperature response and thermal conductivity. Therefore little water content is removed from samples and thermal properties are unchanged during the experiment. In this method, the samples are made considerably long with a high aspect ratio (the sample is considered infinitely long), so that any axial heat flow is negligible and only heat flow occurs in the radial direction. Therefore 1-dimentional (1-D) radial heat transfer is only considered in the analysis.

In this paper, a hot wire probe was created and utilized to measure thermal conductivity of tissue representative sodium alginate phantoms containing varying CNT types (SWMTs, MWNTs, and SWNHs) and CNT concentrations (0.1 mg/ml, 0.5 mg/ml, and 1.0 mg/ml). Concentrations lower than 1.0 mg/ml have been shown to cause minimal toxicity [23-24,33] and when combined with laser heating can produce significant heat generation, thermal based tumor destruction, and tumor regression in both *in vitro* and *in vivo* studies [22-24,74,104]. Knowledge of the impact of CNT type and concentrations will permit more accurate prediction of temperature distribution and tumor response following therapy and guide selection of the appropriate type and concentration of nanoparticles to maximize thermal diffusion in the laser treated zone. This knowledge will also aid in development of computational treatment planning models for laser therapies utilizing CNTs by providing more accurate thermal conductivity input properties necessary for temperature prediction within the treated tissue.

4.3. Materials and methods

4.3.1. Hot Wire Probe

The hot wire probe was constructed from high precision stainless steel tubes, Nichrome wire, and thermocouples. Two stainless steel tubes with outer diameters (ODs) of 0.635 mm (inner tube) and 1.47 mm (outer tube, d) were cut into 50 mm long (L) pieces (Figure 4.1A), which gives the aspect ratio (L/d) of 34. Backwell *et al* [105] found that the aspect ratio must be greater than 24 in order to avoid any axial heat transfer in the probe. The inner tube was coiled tightly with Nichrome wire to prevent formation of a gap between the two coils and eliminate overlap (Figure 4.1B). The inner tube with the Nichrome coil was then dipped into highly conductive Ceramabond aluminum nitride solution to create a coating around the coil and placed into the outer tube (Figure 4.1C) to eliminate an air gap between the coil and the outer tube. A

thermocouple (K-type) was welded to the middle of the outer tube in order to measure temperature response (Figure 4.1C) [49,52]. The heater probes were calibrated with agar gel samples with known thermal conductivity.

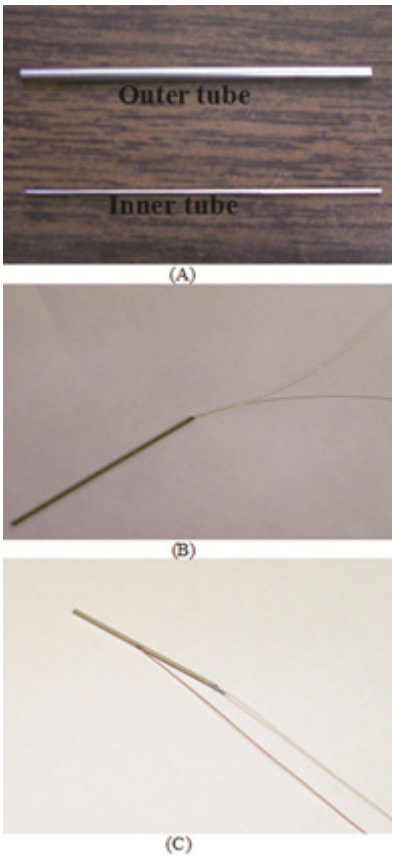

Figure 4.1: Development of hot wire probe: two high precision stainless steel tubes, inner and outer tube (A). Inner tube was coiled with Nichrome wire (B). A complete hot wire probe (C)

4.3.2. Measurement theory

Thermal conductivity of tissue phantoms alone or incorporated with CNTs of varying type (MWNT, SWNT, and SWNH) and different CNT concentrations referred to as CNT-phantom composites were measured using a cylindrical hot wire technique [49,52,58-59]. The governing equation used for this method is described below.

$$\frac{\partial^2 T}{\partial r^2} + \frac{1}{r}\frac{\partial T}{\partial r} = \frac{1}{\alpha}\frac{\partial T}{\partial t} \tag{4.1}$$

Equation (4.1) is a 1-D transient heat transfer equation with cylindrical coordinates, where T is the temperature, r is the position, t is the time, and α is the thermal diffusivity. The solution of equation (4.1) [106] was expressed as

(4.2)

$$T - T_i = -(q'/4\pi K)E_i(-r^2/4\alpha t)$$

where, T_i is the uniform initial temperature at time $t < 0$, K (W/m·K) is the thermal conductivity, q' (W/m) is the constant heat source applied to the heater probe at $t > 0$ represented by $q' = \frac{V^2}{R \cdot L}$, where V is the voltage, R is the resistance, and L is the length of the heat source. $E_i(-x)$ is the exponential integral function, which is defined as

$$E_i(-x) = -\gamma + \ln x + \sum_{n=0}^{\infty} \frac{(-x)^n}{n \times n!} \quad , \quad \text{when } x > 0 \tag{4.3}$$

where γ=0.5772 is an Euler's constant.

Equation (4.3) can be reduced to the first two terms for the condition of $r^2/4\alpha t < (0.16)^2$ by eliminating the infinite summation component [107] and expressed as the following equation (4.4).

$$T - T_i = \frac{q'}{4\pi K}\left[\ln\left(\frac{4\alpha t}{r^2}\right) - \gamma\right] \tag{4.4}$$

After differentiating equation (4), and solving for K,

$$K = \frac{q'}{4\pi}\left(\frac{dT}{d\ln(t)}\right)^{-1} \tag{4.5}$$

If the slope $\frac{dT}{d\ln(t)}$ is known, K can be measured from equation (4.5).

In order to avoid the outer surface effects of the sample on the temperature rise of the heater probe, the following criteria must be satisfied for a one dimensional model

$$R_0 > 2(\alpha t)^{1/2} \tag{4.6}$$

where R_0 is the outer radius of the sample. With this criteria, the surface effects on the temperature response are less than 0.1% and a linear relationship is formed between the temperature response and logarithmic time [49,52]. If the heating time is less than 5 min and the thermal diffusivity, α is $1.4 \times 10^{-7} m^2/s$ (e.g. water, pig tissue, or any sample more than 90% of water), the minimum outer radius, R_0 of a sample can be calculated to be 12.9 mm from equation 4.6. For this sample, a linear temperature response will become nonlinear and surface temperature will begin to affect the probe temperature at 5 min of heating. The linearity of

temperature response is critical since the thermal conductivity will be determined from the slope of the temperature response in the linear region.

4.3.3. Sample preparation

MWNTs and SWNTs were purchased from SES research, inc. SWNHs were received from Dr. David Geohegan's lab at Oak Ridge National Laboratories. The purity of all above mentioned CNTs was confirmed to be greater than 95% by thermogravimetric analysis (TGA) and transmission electron microscopy (TEM). The length of MWNTs and SWNTs were in the range of 900-1200 nm. Outer diameters of MWNTs were in the range of 40-60 nm, whereas the outer diameters of SWNTs were less than 2 nm. The individual SWNHs had diameters of 3-5 nm and lengths of 25-50 nm.

MWNTs, SWNTs, and SWNHs are naturally hydrophobic and are not soluble in polar solvents like water. All types of CNTs were made water soluble by functionalizing their outer surface with 1% w/v concentration of Pluronic F-127 purchased from Biotium, Inc. This process formed a non-covalent hydrophilic layer around the CNTs without changing any thermal, optical, or mechanical properties. CNTs in the pluronic-water solutions were sonicated for 30-40 minutes to create three desired concentrations (0.1 mg/ml, 0.5 mg/ml, and 1.0 mg/ml). We paid significant attention to the quality and extent of CNT dispersion in the aqueous solutions. For instance, after functionalizing CNTs with 1% pluronic water, we sonicated the mixture for 40 min and then monitored the solutions for several months. We observed no precipitation of the CNTs out of solution and the solution maintained a homogenous coloration. Furthermore, previous studies have shown CNTs dispersed in pluronic solution does not cause any cytotoxisity when incubated with cells and when introduced into tumors[23-24]. Therefore, the use of pluronic does not pose any concerns for future clinical studies.

Tissue representative phantoms were created from sodium alginate Protanal LF 10/60 (FMC Biopolymer, Drammen, Norway) a low viscosity alginate with a mean guluronate / mannuronate (G/M) ratio of 70% and mean molecular weight of 180 kDa. Sodium alginate powder was mixed with CNT-pluronic water solutions described above to a 3% w/v concentration (3g / 100 ml) for 1 hour to create the desired final concentrations of CNTs in alginate solution. We monitored CNT dispersion in liquid alginate gel at 4^0C temperature before and following cross-linking for a month. For non-crosslinked samples maintained at 4^0C for several weeks, no precipitation of CNTs in the solution was observed as evidenced by a

homogeneous dark phantom. This indicates CNTs are evenly suspended in the solution without forming any precipitation. Before measurement of thermal conductivity, the final solution was cross-linked with calcium chloride for several weeks [108-109] to completely solidify the sample. The sodium alginate phantoms had a radius of 15.75 mm and length of 120 mm. The samples were made long enough to minimize any axial heat flow, which makes the system amenable to a 1-D radial heat diffusion analysis [105]. Our sample radius, 15.75 mm, was large enough to avoid any surface effects on the probe temperature. In order to verify the homogeneity of CNTs dispersion in cross-linked samples, phantoms were sectioned into tissue samples of 50-60 nm thickness by a microtome at locations at the top, middle, and bottom of the phantom. From each section at least 5 samples were made. TEM images were taken of all samples. Based on these images, CNTs were observed to be uniformly distributed. The following TEM image was taken from the middle of a phantom containing MWNTs after cross-linking. This image was included in the paper as Figure 4. 2. Although not shown, phantoms containing SWNHs and SWNTs looked similar.

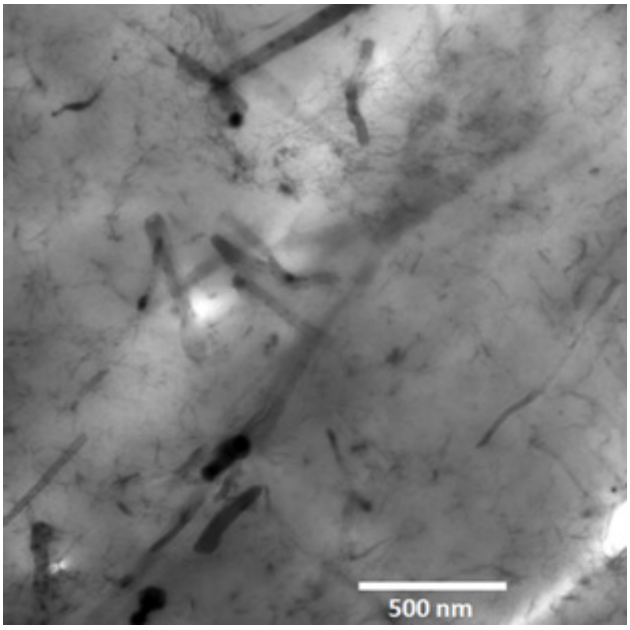

Figure 4.2: TEM image of MWNTs incorporated in solid phantom

Ten types of experimental samples of tissue representative phantoms were prepared with sodium alginate solution with n=3 for each type of sample. Among them one phantom was made

without CNTs and nine phantoms were prepared with inclusion of MWNTs, SWNTs, and SWNHs with three different concentrations of 0.1 mg/ml, 0.5 mg/ml, and 1 mg/ml.

In order to calibrate the hot wire probe and confirm its accuracy, an agar tissue phantom with known thermal conductivity was created and the thermal conductivity was measured with the hot wire probe [54]. The phantom was made from 5 gm agar gel in 100 ml water. Agar gel was mixed in boiling water uniformly and cooled rapidly in ice water. After 12 hrs the sample became solidified to allow measurement.

4.3.4. Experimental setup

Samples were maintained in a water bath with a fixed temperature (24^{o}C) to avoid any temperature fluctuation at the boundary of the samples. A heater probe with length of 50 mm pierced the middle of a sample and was connected to a power source as shown in Figure 4. 3. Agar gel and all sodium alginate phantoms were heated for 5 to 10 minutes depending on the maximum heating time calculated in equation 6 by applying 5 V. The thermocouple of the heater was attached to a data acquisition system (National Instruments, NI 9211) and the time dependent temperature response was measured with the VI Logger from LabVIEW software.

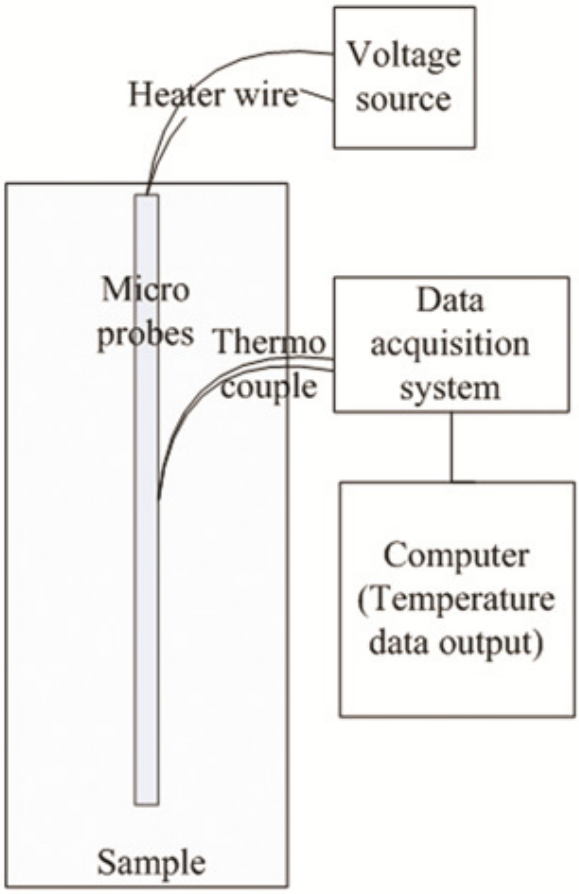

Figure 4.3: Schematic diagram of the experiment

4.3.5. Uncertainty analysis

Uncertainties and sensitivities [110-111] of all experimentally measured parameters were determined in order to calculate estimated sources of error in the thermal conductivity measurement. Thermal conductivities were represented in terms of experimentally measured parameters, slopes (*S*) of the temperature response and prescribed values of heat sources (q') in equation 4.5. The total estimated uncertainty (δK) of the thermal conductivity measurements was computed by the method of propagation of uncertainties in equation 4.7 [110].

$$\delta K = \left\{ \sum_{i=1}^{N} \left(\frac{\partial K}{\partial X_i} \delta u_i \right)^2 \right\}^{1/2} \tag{4.7}$$

where, $\frac{\partial K}{\partial X_i}$ is the sensitivity coefficient of thermal conductivity with respect to each parameters, X_i (slopes and heat sources) and δu_i is the uncertainty for a specific parameter X_i.

4.4. Results

4.4.1. Surface effect of the heater probes

The temperature response of all samples consisted of both linear and nonlinear components with respect to the natural logarithm of time. For agar gel samples, the linear response of temperature became nonlinear at approximately 7 min (ln(t)~4) due to the surface effects of the samples of 15.75 mm radius (Figure 4.4). The maximum heating time for the linearity of temperature response was calculated to be $7\,\text{min}\,23\,\text{sec}$ from equation 6 with $\alpha = 1.4\times10^{-7}\,m^2/s$ and sample radius, $R_0 = 15.75$ mm. Beyond this time the temperature response became nonlinear and the surface temperature of samples was affected by the temperature rise of the heater probe. This calculated time was close to the experimentally measured value of approximately 7 min (Figure 4.4). This close correspondence between measured and calculated values confirms the accuracy of the probe measurement.

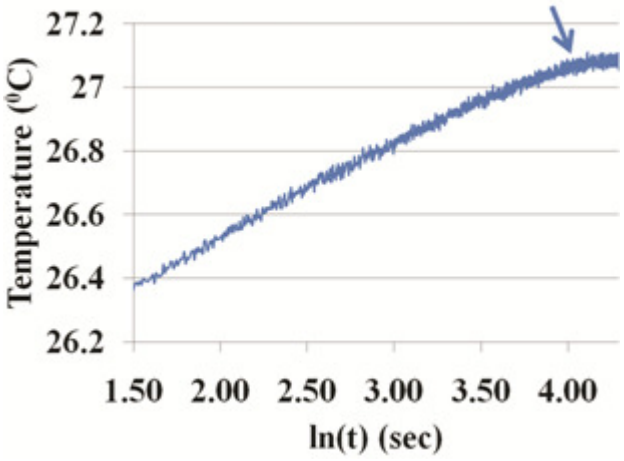

Figure 4.4: Temperature response of Agar gel sample of radius 15.75 mm. The arrow indicates where the linear response becomes non-linear at approximately 7 min (ln(t)~4) due to the surface effects

4.4.2. Variable of heat source voltage

Prior to measurement of the thermal conductivities of all CNT-phantoms, different voltages (5V and 8V) were applied to the agar gel sample to determine the effect of varying voltage on thermal conductivity. For each voltage, temperature responses were represented with logarithmic time (Figure 4.5A-B). Slopes of the temperature responses were measured by curve

fitting of the linear portion (from ln(t)=1.35-3 sec) of the temperature response. In this region the curve fit was found to yield R^2 values of 0.9785 and 0.9913, indicating an accurate curve fit for 5V and 8V respectively. Using a lower voltage (5V) contributes to higher noise for the temperature response and results in a lower R^2 value compared to a higher voltage (8V). The slope $(dT/d\ln t)$, determined by linear regression from Figures 4.5A-B, was used in equation 5 and thermal conductivities for the agar gel samples were calculated to be 0.568 W/m·K and 0.5889 W/m·K for 5V and 8V respectively. Due to the similarity of the thermal conductivity values, it is evident that varying the voltage had minimal effect on thermal conductivity measurement. Based on the literature, the actual thermal conductivity of the agar gel (5 gm in 100 ml of water) is 0.576 W/m·K [54], which is very close to our experimental results.

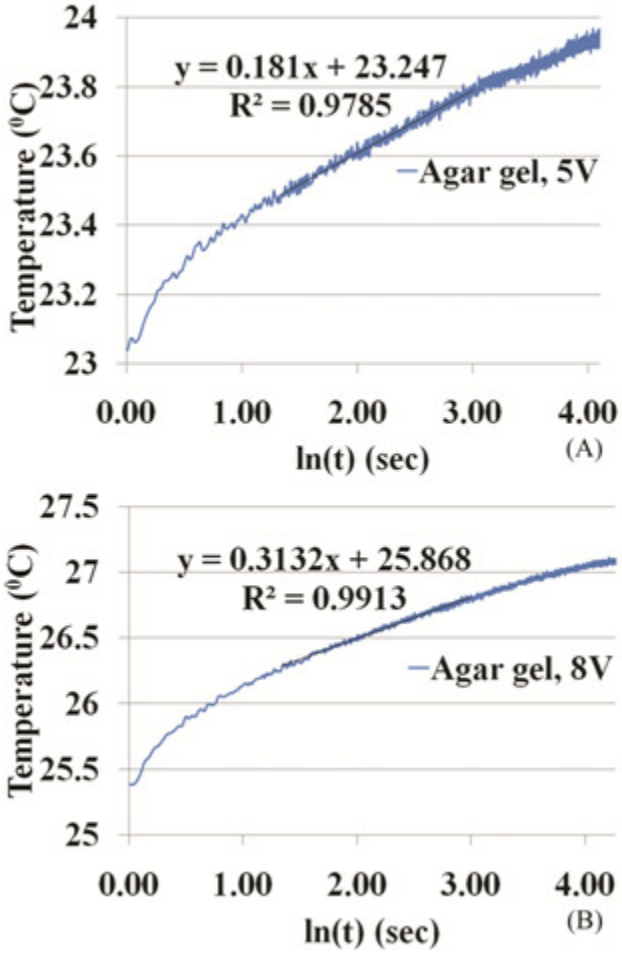

Figure 4.5: Temperature response of Agar gel with natural log of time for 5 V (A) and 8V supply

4.4.3. Error estimation

Uncertainty of the temperature measurement (±0.05 ^{0}C) was associated with the data acquisition system, the thermocouples, and the electronic weigh machine (concentration error). Uncertainties of voltage (±0.025 V) and resistance (±2.16 ohms) measurement were associated with the power source. Uncertainty of temperature measurement was utilized to determine the uncertainty of slopes (S) and uncertainties of voltage and resistance measurement were utilized to determine the uncertainty of heat sources ($q^{'}$) by the method of propagation of uncertainties [111]. Uncertainties of slopes (S) and heat sources ($q^{'}$) and sensitivities of thermal conductivities with respect to slopes and heat source are tabulated in Table 1. These values were utilized to compute the total estimated uncertainty of thermal conductivities, which were found to be 5.46%. The majority of estimated uncertainty arose from the uncertainties associated with the slopes from which thermal conductivity is determined.

Table 4.1: Estimated uncertainties and sensitivity coefficients of the experiment

Parameters	Slope (S)	Heat source (q')	Total estimated uncertainty
Δu_i	0.139 K·s^{-1}	0.0241 W·m^{-1}	5.46%
$\partial K/\partial x_i$	4.526 W·m^{-1}·s^{-2}·K^{-2}	0.4411 s·K^{-1}	

4.4.4. Thermal conductivity of tissue phantoms

We used a heat source of 5V to measure thermal conductivities for sodium alginate phantoms with and without CNT inclusion in order to avoid thermal damage to the heater probes. Figure 4. 6 represents the temperature response with respect to natural logarithmic time of sodium alginate phantoms (3 gm in 100 ml water) without CNT inclusion. The slope of the temperature response was 0.1809 with R^2 value of 0.9792 found by linear regression in the range of ln(t) values from 1.35-3 sec. The thermal conductivity was computed for the phantom to be 0.5737 W/m·K using equation 5, which is very close to the measured thermal conductivity of agar gel. Due to the high volume of water content (>95%) in agar gel and sodium alginate phantoms, thermal conductivities were nearly identical to mineral water (0.58 W/m·K).

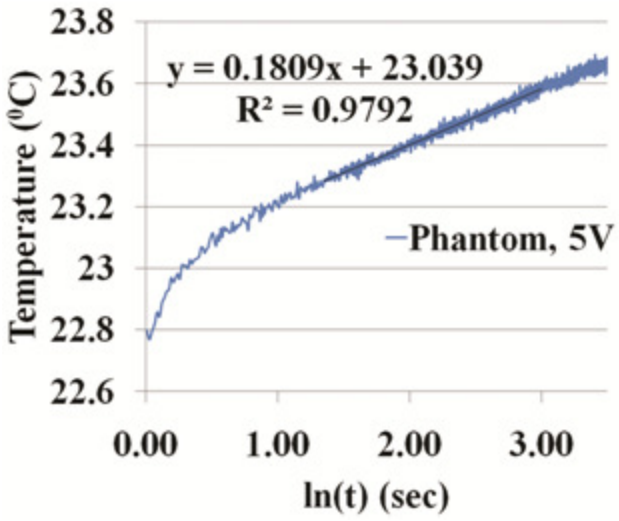

Figure 4.6: Temperature response of sodium alginate phantom without CNTs using 5 V supply

Thermal conductivities of phantoms containing SWNTs, MWNTs, and SWNHs of varying concentrations (0.1 mg/ml, 0.5 mg/ml, and 1.0 mg/ml) were determined in a similar manner as discussed for the agar gel and phantoms without CNTs. The experimental measurement was conducted at least three times for each type of sample with multiple heater probes. Since all heater probes were calibrated with the known thermal conductivity of agar gel, the thermal conductivity was independent of the heater employed. The slope was determined uniformly for all samples according to ln(t)=1.35-3. Slopes will vary based on the thermal conductivity of the samples in the same data range. However, since all slopes were determined from same ln(t) range 1.35-3 all thermal conductivities are comparable to each other. Different ranges were explored, but the selected range gave the highest R^2 value of 0.9785-0.9913. Thermal conductivities of phantom and all CNT-phantom composites are shown in Figure 4. 7. The error limits of each data in Figure 4.7 were computed from the total estimated uncertainties (5.46%). We observed that thermal conductivities of CNT-Phantom composites increased with concentration (0.1 mg/ml, 0.5 mg/ml, and 1.0 mg/ml). If the concentrations of CNTs were increased by 10 times (0.1 mg/ml to 1 mg/ml), the composite thermal conductivities increased 10%, 26%, and 38% for phantoms containing SWNTs, SWNHs, and MWNTs respectively (Figure 4.7). Incorporating a 0.1 mg/ml of SWNTs, SWNHs, and MWNTs into phantoms increased the overall thermal conductivity by 13%, 4%, and 20% compared to phantoms without CNTs. Thermal conductivities of phantoms increased by 24%, 30%, and 66% when 1.0 mg/ml

SWNTs, SWNHs, and MWNTs were respectively incorporated in phantoms. MWNT-Phantom composites provided the highest thermal conductivity compared to other CNT composites. Thermal conductivities of phantoms containing SWNTs were superior to phantoms with SWNH inclusion in the concentration range of 0.1 mg/ml to 0.5 mg/ml. However, inclusion of SWNHs increased thermal conductivity more significantly than SWNTs for concentrations higher than 0.5 mg/ml. The values of thermal conductivities with estimated errors are tabulated in Table 4.2.

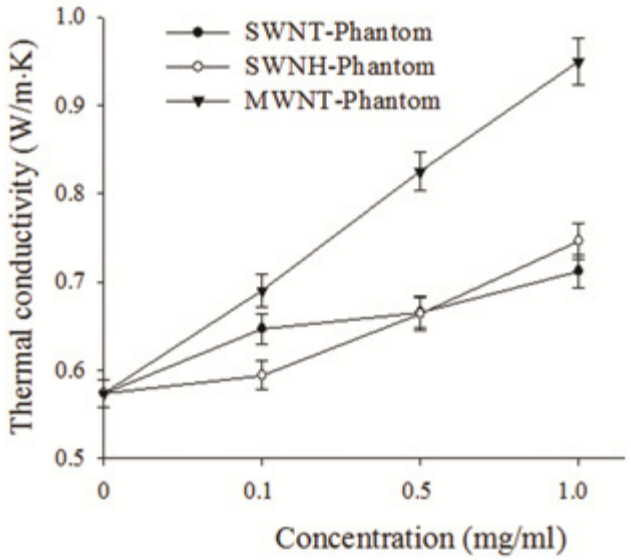

Figure 4.7: Thermal conductivities of CNT-phantom composites with varying CNT type and concentration

Table 4.2: Thermal conductivity of Phantom-CNT composites

	Thermal Conductivity, (W/m·K)			
Concentrations, (mg/ml)	Phantom	Phantom-SWNT	Phantom-SWNH	Phantom - MWNT
0	0.5737±0.016	-	-	-
0.1	-	0.6464±0.017	0.5941±0.016	0.6901±0.019
0.5	-	0.6654±0.018	0.6636±0.018	0.8253±0.022
1	-	0.71152±0.019	0.7463±0.02	0.9495±0.026

4.5. Discussion

This study determined the effect of incorporating varying CNT type (SWNT, MWNT, and SWNH) and concentration (0.1 mg/ml, 0.5 mg/ml, and 1.0 mg/ml) on the overall composite thermal conductivity of tissue representative phantoms. Sodium alginate phantoms were utilized as tissue mimics since their thermal conductivity (0.5737 W/m·K) is very close to that of human tissue (0.5-0.58 W/m·K) [49-53]. Inclusion of CNTs into tissue representative phantoms increased the overall thermal conductivity of the tissue phantom composite. Due to the extremely high thermal conductivity of CNTs (3000-6000 W/m·K), we anticipated the thermal conductivity of tissue phantoms would increase significantly following inclusion of CNTs. However, we observed the overall thermal conductivity of tissues with CNT inclusion to increase less than expected due to the presence of interfacial thermal conductance. Despite the moderate gains in thermal conductivity, their inclusion is still valuable.

Although other studies have measured interfacial thermal conductance of CNTs in liquid solution, [98-99] few studies have measured the overall thermal conductivity of CNTs in tissue or in solution. The hot wire probe method we used is simple and accurate for measuring thermal conductivity of tissue representative phantoms. Previous studies used this method to measure thermal conductivities of agar gel, styrofoam, gelatin, and cow liver where uncertainty was estimated to be 4% [49]. The total estimated uncertainty of our experiments was found to be 5.46% which represents the accuracy of our experimental setup. Therefore, the hot wire probe method is an ideal method for measuring thermal conductivity of all types of soft tissue.

4.5.1. Effect of Concentration

We utilized CNT concentrations of 0.1 mg/ml, 0.5 mg/ml, and 1.0 mg/ml, because previous research has shown CNT concentrations lower than 1.0 mg/ml to have minimal toxicity [23-24,33]. Furthermore SWNT, MWNT, and SWNH concentrations in the range of 0.1-1.0 mg/ml used in combination with laser heating can produce significant heat generation for effective thermal based tumor destruction and regression in both in vitro and in vivo studies [22-24]. Increasing CNT concentration by 10 fold (0.1 mg/ml to 1 mg/ml), caused the overall composite thermal conductivities of phantoms containing SWNTs, SWNHs, and MWNTs to increase by 10%, 26%, and 38% respectively. However if the concentrations was increased from 0 to 0.1 mg/ml, thermal conductivities increased by 13%, 4%, and 20% for phantoms containing SWNTs, SWNHs, and MWNTs respectively. If the CNT concentration was increased from 0 to

1.0 mg/ml thermal conductivities increased by 24%, 30%, and 66% for phantoms containing SWNTs, SWNHs, and MWNTs respectively. For an identical concentration of 1.0 mg/ml, the thermal conductivity of phantoms containing MWNTs and SWNHs were 1.33 and 1.05 times higher respectively than phantoms with inclusion of SWNTs. Phantoms containing MWNTs have the highest thermal conductivity compared to phantoms incorporated with SWNHs and SWNTs.

The greatest increase in thermal conductivity was observed for the highest CNT concentration. Higher CNT concentrations than 1 mg/ml may potentially cause cells to experience reduced cell proliferation [104]**.** However, many epithelial based tumors (e.g., skin, bladder, prostate) are amenable to localized direct injection of CNTs into the tumor followed by laser treatment. In this instance, we will want to maximize light absorption and thermal conductivity. Therefore, increasing CNT concentration greater than 1 mg/ml will be beneficial. Furthermore, by preferentially targeting tumor cells with CNTs conjugated with tumor specific antibodies or biomolecules (e.g. folic acid), we can supply a high concentration of CNTs in the desired tumor regions, thereby locally increasing optical absorption and thermal conductivity. By selectively depositing CNTs in the tumor regions, we can eliminate associated toxicity to normal tissue eliminating concern with high CNT concentration.

4.5.2. Effect of interfacial thermal resistance

SWNTs, SWNHs, and MWNTs possess exceptionally high thermal conductivity in the range of 3000-6000W/m·K. However, inclusion of CNTs in sodium alginate phantoms did not increase the thermal conductivity of the overall composites substantially. This is due to the high interfacial thermal resistance between CNTs and sodium alginate phantoms. These results are in close agreement with the effect of interfacial thermal conductance at the CNT-matrix interface, described by Huxtable *et al*, and Merabia *et al* [98-99]. The measured thermal conductivities of CNT composites were found to be less than computationally determined thermal conductivities by Nan *et al* [47,100], when interfacial thermal resistances were not considered. Thermal conductivities could be potentially increased 5-20 times, if the interfacial thermal resistances were negligible.

4.5.3. Diameter effects of CNTs in tissue composites

MWNT-Phantom composites provided the highest thermal conductivity compared to other CNT composites. This is most likely due to their larger diameter (40-60 nm). However, the intrinsic thermal conductivity of MWNTs (3000 W/m·K) is lower than that of SWNTs (6000 W/m·K). Nan *et al* described [47] computationally by effective medium approach that MWNT-composites will have higher thermal conductivity than that of SWNT-composite due to the larger diameter of MWNTs. Our experimental results exhibit close agreement with the computational results of Nan *et al*. Due to the smaller diameter of SWNTs (less than 2 nm), thermal conductivities of SWNT-Phantom composites increased gradually with higher CNT concentration. However, for SWNH-Phantom composites, thermal conductivities exceeded SWNT-Phantom composites for concentrations greater than 0.5 mg/ml. SWNHs are composed of numerous SWNTs held together by Van-der-Waals forces forming Dalia like structures with overall diameters of 50-100 nm. It is this difference in structure that has been shown to influence optical properties and may affect the thermal conductivity. Higher concentrations of larger clusters may exceed the thermal conductivity of relatively smaller diameter SWNTs in a composite.

4.6. Conclusion

This is the first study investigating the impact of CNT inclusion on the composite thermal conductivity of tissue representative structures containing varying CNT type and concentration. Inclusion of MWNTs in the tissue phantom caused the greatest increase in thermal conductivity compared to all CNTs considered due to their large diameter. The measurement of thermal conductivities of CNT-Phantom composites was in close agreement with other researcher's computational model predictions. It is anticipated that inclusion of CNTs in normal and tumor tissue will exhibit similar trends observed for sodium alginate phantoms. The composite thermal conductivity of phantoms containing CNTs did not increase as significantly as expected due to the existence of interfacial thermal resistance. Thermal conductivity could be potentially increased 5-20 times if the interfacial thermal resistance was negligible. Knowledge of the composite thermal conductivity permits comparison of the thermal diffusion properties of tissues containing varying CNT types. The measured thermal conductivity values for CNT phantom composites can provide more accurate input parameters necessary for development of

computational models for predicting laser heating of CNTs in tissue. In the future, we envision targeting of CNTs to tumor cells to locally enhance thermal conductivity in desired tumor regions.

4.7. Acknowledgements

This research was funded by the following sources: National Science Foundation Grant CBET 0731108, National Institute of Health Grant 1 R21 CA135230-01, and an Institute for Critical Technology and Applied (ICTAS, Virginia Tech) Science Grant. We would also like to thank Dr. David Geohegan from Oak Ridge National Laboratories for his kind gift of the single walled carbon nanohorns. We would also like to express our gratitude to Dr. Thomas Diller of Virginia Tech for his insightful guidance and assistance with fabricating the hot wire probes.

Chapter 5: Photothermal effects

The following article will be submitted in the **Lasers in surgery and medicine** following refinement and statistical analysis.

Comparison of optical properties of breast tumor phantoms containing SWNTs, MWNTs, and SWNHs

Saugata Sarkar[1], Abhijit A. Gurjarpadhye[2], Christopher G. Rylander[1,2], Marissa Nichole Rylander[1,2].
[1]Department of Mechanical Engineering
Virginia Tech, Blacksburg, VA 24061.

[2]School of Biomedical Engineering and Sciences
Virginia Tech-Wake Forest, Blacksburg, VA 24061.

Email: mnr@vt.edu.
Keywords: Cancer therapy, Carbon nanotubes, laser treatment, oncology, soft tissue composite.

5.1. Abstract

The effectiveness of photothermal cancer therapy depends on the amount of light absorbed by a tumor during irradiation. The light absorbing capacity of a tumor can be greatly enhanced by introducing carbon nanotubes (CNTs) into the tissue prior to laser treatment. However, the degree by which light absorbing and scattering properties of tumors are altered following introduction of CNTs is not well understood. In this study we determined the optical properties of breast tumor representative phantoms following inclusion of CNTs of varying type and concentration.

Multi-walled carbon nanotubes (MWNT, length 900-1200 nm, diameter 40-60 nm), single-walled carbon nanotubes (SWNT, length 900-1200 nm, diameter <2 nm), and single-walled carbon nanohorns (SWNH, overall diameter of 50-100 nm) of varying concentrations (0.01-0.1 mg/ml) were uniformly added to aqueous solutions and phantoms representative of breast tumor tissue. Breast cancer representative phantoms (thickness~800 μm) were made from sodium alginate (3 g/ml) incorporated with polystyrene microbeads (diameter 3 μm, and 1 mg/ml) and talc-France (40 mg/ml). Transmittance and reflectance of phantoms containing CNTs were measured with a spectrophotometer and served as inputs to the inverse adding doubling algorithm (IAD) to allow determination of the absorption (μ_a) and reduced scattering

(μ_s') coefficients for the wavelength range of 400-1300 nm. Whereas absorption coefficients of aqua solution were determined by Beer's law.

The optical properties of breast cancer phantoms without CNTs were μ_a = 0.044-0.055 mm^{-1} and μ_s' = 0.05- 0.07 mm^{-1} at a wavelength of 900 nm which corresponds closely with published data of human breast tumor tissue. Incorporating MWNTs, SWNTs, and SWNHs in phantoms with a concentration of 0.1 mg/ml increased light absorption coefficients 20-30 fold, 5-6 fold, and 9-14 fold respectively for the wavelength range of 800-1100 nm. However, the corresponding change in reduced scattering coefficients for identical conditions was minimal, varying 1.2-1.3 fold.

Introduction of CNTs into aqueous solutions and tissue representative phantoms significantly increased absorption with minimal effect on scattering thereby providing a means to enhance the photothermal therapeutic benefit of laser therapies.

5.2. Introduction

Inclusion of light absorbing nanoparticles into tissue undergoing laser cancer therapy can increase the absorption coefficient and thus photothermal generation within the targeted tissue volume. Photothermal therapies with nanoparticle inclusion can potentially achieve a greater degree of efficacy, treat larger tumor volumes, and require shorter treatment durations due to the increased heat deposition and thermal diffusion in the tumor [22-24]. CNTs have received attention for their potential role as thermal enhancers for laser ablation and drug delivery [26-27]. CNTs are composed of graphene sheets with sp^2 bonded carbon atoms rolled seamlessly into a tubular form. The two major types of CNTs are SWNTs which have one seamless tube and MWNTs which possess two or more concentric tubes. The diameter and length of SWNTs are 1.5-3.0 nm and 20-1000 nm respectively whereas the corresponding diameter and length dimensions for MWNTs are 5.0 -100 nm and 1-50 microns respectively [24,28,31-32]. Another unique embodiment of SWNTs are single-walled carbon nanohorns which are composed of an aggregate of cone shaped SWNTs each with an individual length of 25-50 nm and diameter of 1-1.5 nm. The spiny agglomerate SWNH structure has an overall diameter of 50-100 nm. CNTs possess exceptional electromagnetic, thermal, and chemical properties. The most remarkable property of CNTs (both metallic and semiconducting) is their ability to absorb electromagnetic

signals in the near infrared region (NIR) (700-1100 nm) leading to considerable heat generation at specified tissue depths [23-24,33]. Light within this optical window has been shown to penetrate human skin with 1/e penetration depths of 1.6-2 mm [18]. The length of a CNT has considerable impact on its ability to absorb light. For a specific frequency of the incident electromagnetic signal, efficient light absorption occurs when the length of the CNT is at least half the wavelength of the incident light based on antenna theory [34-37]. CNT lengths of 900-1200 nm have been shown by our group to possess significant light absorption at a wavelength of 1064 nm leading to heat generation capable of tumor destruction [22-24]. However, limited information exists regarding the optical properties (absorption and scattering coefficients) of solutions or tissues containing CNTs of varying type, properties, and concentration. This information is critical to appropriate selection of CNTs for designing therapies utilizing laser treatment and nanoparticles.

Previous studies have measured a variety of optical properties including refractive index, absorbance, transmittance, reflectance, and scattering properties of CNTs in liquid solutions [26,112-122]. Jeong *et al*. measured attenuation and extinction coefficients of SWNTs in water by optical absorption spectroscopy in the wavelength range of 270-1000 nm [120]. Khudyakov *et al.* measured the optical absorption coefficient of SWNTs in carboxymethyl cellulose (CMC) thin polymer film by the Z-scan method and found absorption coefficients to be nonlinear with different intensities of pulsed laser (20-50 MW/cm^2) [122]. Despite these initial studies, this will be the first paper measuring and comparing the absorbance of SWNTs, MWNTs, and SWNHs for identical wavelengths and concentrations of CNTs providing the ability for true comparison of the absorbing ability of these CNTs.

Different computational techniques can be used to compute absorption and reduced scattering coefficients such as Kubelka-Munk approach [62], Inverse Monte Carlo method [63-65], and IAD method [66]. We chose to use the IAD method because it is accurate and computing time is rapid. IAD requires transmittance, reflectance and refractive index as input parameters in order to calculate absorption and reduced scattering coefficients. Others have used inverse and forward adding doubling to obtain the previously mentioned optical properties of tissue and phantoms [66,123-124]. However, prior studies have not determined the absorption

and reduced scattering coefficient of tissues or representative tissue phantoms incorporated with CNTs.

In this paper we determined the attenuation, absorption and scattering coefficients of two different media, 1) aqueous solutions and 2) representative breast tumor phantoms with optical properties identical to breast tissue both containing CNTs of varying type (SWNTs, MWNTs, and SWNHs) and concentration (0.01-0.1 mg/ml) . This study offers the first opportunity to truly compare the absorbing and scattering ability of CNTs of varying type under identical conditions (wavelength, CNT concentration). Liquid and solid media were considered in order to study the effect of optical properties in the both media in presence of CNTs. Since the interfacial contact between CNTs and liquid or solid phantoms, may be different potentially impacting optical properties, both types of samples were utilized. Knowledge of the composite optical properties of solutions and tissue phantoms with CNT inclusion will assist with selection and prediction of tissue response to nanoparticle-mediated laser therapies.

5.3. Materials and methods

5.3.1. Water soluble CNTs

MWNTs were synthesized by Dr. David Carroll's group at Wake Forest university [23-24], SWNTs were purchased from SES research, and SWNHs were synthesized by Dr. David Geohegan's group at Oak Ridge National Laboratories [125-126]. The length of MWNTs and SWNTs ranged from 900-1200 nm. Outer diameters of the MWNTs were in the range of 40-60 nm, whereas SWNT outer diameters were less than 2 nm. Individual SWNHs had diameters of 1-1.5 nm and lengths of 25-50 nm. The purity of all above mentioned CNTs was confirmed to be greater than 95% by thermogravimetric analysis (TGA) and transmission electron microscopy (TEM).

MWNTs, SWNTs, and SWNHs are naturally hydrophobic and they are not soluble in polar solvents such as water. All types of CNTs were made water soluble by functionalizing their outer surfaces with 1% w/v concentration of Pluronic F-127 purchased from Biotium, Inc. This process formed a non-covalent hydrophilic layer around the CNTs without changing any

thermal, optical, or mechanical properties. CNTs in the pluronic-water solutions were sonicated for 40-50 minutes to make desired concentrations of 0-1.0 mg/ml for liquid samples.

5.3.2. Tissue phantom preparation

Tissue representative phantoms were created with optical properties similar to that of breast tumor tissue. Tissue representative phantoms were produced from sodium alginate Protanal LF 10/60 (FMC Biopolymer, Drammen, Norway) a low viscosity alginate with a mean guluronate / mannuronate (G/M) ratio of 70% and mean molecular weight of 180 kDa. Sodium alginate is transparent and does not adequately reflect the intrinsic scattering properties of biological tissues. In order to create phantoms that possessed optical properties representative of breast tumor tissue, light scattering and absorbing polystyrene beads and highly light scattering talc-France perfume powder were evenly mixed with water-CNT solution [127-128]. The final formulation utilized talc-France perfume powder (40 mg/ml) , and polystyrene beads (diameter= 3 µm, 1 mg/ml) in sodium alginate.

Next, the CNT phantom composite tissue structures were created. Three concentrations (0.01 mg/ml, 0.05 mg/ml, and 0.1 mg/ml) of CNTs were suspended in 1% pluronic water. The concentration range was chosen based on prior studies showing 0.01-0.1 mg/ml caused minimal toxicity while enabling significant heat generation [23-24,33]. Sodium alginate was stirred vigorously with CNT-pluronic water containing polystyrene beads and talc powder to a 3% w/v concentration for 1 hour. The final solution was cross-linked with calcium chloride for 1 hr [108-109]. All samples were made less than 1 mm in thickness to permit adequate light transmission necessary for spectrophotometric measurement [17] (Figure 1A-C). The radius (35 mm) of the cylindrical samples was made large enough to completely cover the reflection and transmission ports of the integrating sphere accessory of the spectrophotometer. For each concentration and type of CNTs, five experimental samples (N=5) were made and all results were represented as the mean values of these samples.

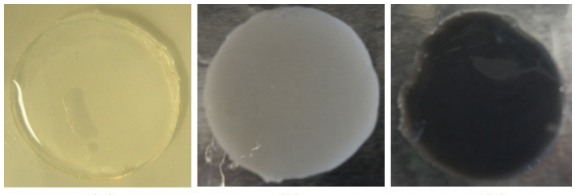

Figure 5.1: Sodium alginate phantom (A), phantom with inclusion of polystyrene beads and talc powder (B), and phantom with polystyrene beads, talc powder, and CNTs

5.3.3. Spectrophotometry

A Cary 5000 Spectrophotometer (Varian Inc, NC) was used to measure transmittance and absorbance of liquid samples in quartz cuvettes. This allowed determination of total attenuation and absorption coefficients respectively of water with and without CNT inclusion in the wavelength range of 200-2000 nm.

Transmittance and reflectance of breast cancer phantoms with varying type and concentration of CNT inclusion were also measured with the spectrophotometer for the wavelength range of 400-1300 nm. This information enabled the absorption and reduced scattering coefficients to be determined by inverse adding doubling method as described in the following section. A diffuse reflectance accessory (DRA 2500) was mounted in the spectrophotometer to allow measurement of diffuse scattering effects. Ballistic-light intensity was measured for 100% transmission (in the absence of sample, I_{0T}) and 100% reflection (using a reflectance standard, I_{0R}) to obtain baseline values. . Sample transmittance, reflectance, and absorbance were calculated based on measured light intensity, I_s at the detector depending on position of the sample in the DRA (Figures 2A-E).

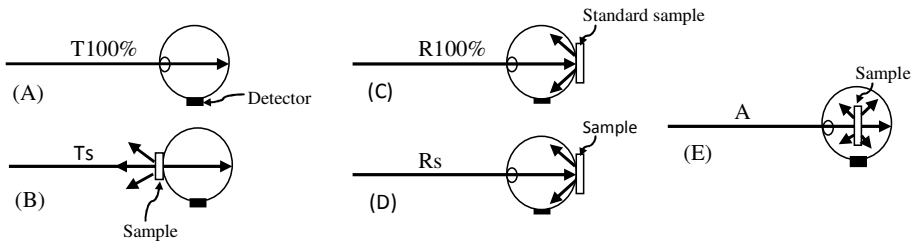

Figure 5.2: Sample position in the DRA in order to measure transmittance, reflectance, and absorbance

When samples are mounted at the transmission and reflection ports of the integrating sphere, transmittance (T) and reflectance (R) are expressed as $T = I_{sT} / I_{0T}$ and, $R = I_{sT} / I_{oT}$ respectively. CNTs in liquid solutions such as water follow a Beer-Lambert law relationship for absorption as shown in equation 1. The total attenuation coefficient (μ_t) is the summation of absorption (μ_a) and scattering coefficient (μ_s) is expressed in equations 2 and 3.

$$\frac{I_s}{I_0} = e^{-\mu_t \cdot d} \tag{5.1}$$

$$\mu_t = \mu_a + \mu_s \tag{5.2}$$

$$\mu_t = -\frac{1}{d}\ln T \tag{5.3}$$

where, d is sample thickness and T is transmittance.

In order to determine absorption coefficients (μ_a), CNT solutions are placed in the center of the integrating sphere and the spectrophotometer only detects the intensity of light which are not absorbed by the sample (Figure 2 E). Absorption coefficient is expressed in equation 5.4.

$$\mu_a = -\frac{2.303}{d}\ln\frac{I_s}{I_0} \tag{5.4}$$

Equations 5.3-5.4 were used to determine attenuation and absorption coefficients for water alone or with CNT inclusion. For the breast cancer phantom samples with and without CNT inclusion, diffuse transmittance and reflectance measured by the spectrophotometer served as input parameters to the inverse adding doubling method allowing determination of the absorption and reduced scattering coefficients.

5.3.4. Inverse adding-doubling (IAD) method

The IAD technique was used to calculate the absorption, scattering, and anisotropy coefficients for breast cancer phantoms with CNT inclusion. An assumption can be made that a soft turbid tissue behaves as an isotropic media and only diffuse transmittance and reflectance are required to measure absorption and reduced scattering coefficients [17]. According to this assumption, scattering can be expressed in terms of reduced scattering coefficient, $\mu_s' = \mu_s(1-g)$, where μ_s is a scattering coefficient and g is an anisotropy factor. In our study, we made the above assumption that anisotropic turbid tissue was expressed as an isotropic media and measurements of diffuse transmittance and reflectance allowed determination of absorption and reduced scattering coefficients by IAD method. This method determined optical properties by inverse calculation of the radiative transport equation [17], where samples require homogenous optical properties with infinite plane parallel slabs. During computation, this method assumed a set of initial values of albedo (a'), optical thickness (b'), and sample thickness (δ) [17,66] which are expressed in equations 5.6 and 5.7. These optical properties are

expressed in terms of absorption and reduced scattering coefficients in Equations 5.8 and 5.9. Absorption (μ_a) and reduced scattering (μ_s') coefficients are calculated from albedo and optical thickness in equations 5.8 and 5.9. The IAD method calculates transmittance and reflectance based on assumed values of optical properties and compares the values of R and T with the corresponding experimentally measured parameters. If the values are not identical, it assumes a new set of values for optical parameters. The process continues until the calculated reflectance and transmittance values are identical to the experimental values, yielding the most accurate values of optical properties.

$$a' = \frac{\mu'_s}{\mu'_s + \mu_a} \tag{5.6}$$

$$b' = \delta(\mu'_s + \mu_a) \tag{5.7}$$

$$\mu_a = \frac{(1-a')b'}{\delta} \tag{5.8}$$

$$\mu'_s = \frac{a'b'}{\delta} \tag{5.9}$$

5.3.5. Optical Coherence Tomography (OCT)

Optical coherence tomography (OCT) is a ballistic optical imaging technique [60,129-130] . OCT was used in this study to measure refractive index for phantoms which was used as an input parameter to the IAD algorithm. When an optically transparent sample is placed in the incident beam, light is reflected from both the first incident plane (air to solid interface) and the second incident plane (solid to air interface) of the sample due to the mismatch of refractive index. The position of the mirror is optically changed after placing the sample in the incident light beam. The optical thickness (OPL) of the sample can be represented as the distance between two reflection peaks of two incident planes. Physical thickness (d) of a sample is represented as the difference between optical thickness (OPL) of the sample and displacement of the mirror position before and after placing the sample in the incident beam. For any sample, refractive index is represented as the ratio between optical thickness to the physical thickness (d) of the sample and determined according to $n_g = \frac{OPL}{d}$, which was utilized to determine the refractive index of phantom samples.

5.4. Results

5.4.1. Total attenuation and absorption coefficients of CNTs in water

The total attenuation coefficients of MWNTs, SWNTs, and SWNHs of varying concentration (0.01-1 mg/ml) in water for the wavelength range of 200-2000 nm are shown in Figures 5.3 A-C. The optical absorption by MWNTs and SWNHs was much more significant than SWNTs such that concentrations greater than 0.25 mg/ml caused substantial noise leading to measurement error of attenuation coefficient. Therefore, the maximum concentration considered for measurement of attenuation of MWNTs and SWNHs in solution was limited to 0.25 mg/ml. The attenuation of SWNTs in water, however, was measured over the complete concentration range (0.01-1 mg/ml) with considerable accuracy. Inclusion of any of the three CNTs in water caused a significant increase in attenuation across all wavelengths compared to water. The total attenuation coefficient of any of the three CNT solutions increases with higher CNT concentration. The attenuation coefficients of all three CNT types were compared at a concentration 0.1 mg/ml as shown in Figure 5.3D. Water containing MWNTs possess the greatest level of attenuation compared to water containing SWNTs and SWNHs. Attenuation coefficients of MWNTs in water are approximately 3.8 times higher than SWNTs and 1.86 times higher than SWNHs at a concentration of 0.1 mg/ml and wavelength of 1064 nm. Attenuation coefficients of SWNHs are approximately 2.07 times higher than SWNTs at the same wavelength.

Total attenuation and absorption coefficients of CNTs were measured and compared for a concentration of 0.1 mg/ml in Figures 5.3 E-G. The comparison was made to determine the contribution of CNTs to optical scattering and absorption. The curves representing the attenuation and absorption coefficients are nearly identical implying the scattering effect of CNTs is negligible when they are evenly dispersed in media. The attenuation coefficients of CNTs in water were compared at 1064 nm wavelength for varying concentration (0-1.0 mg/ml) and were observed to be linearly correlated with concentration (Figure 5.3 H) which correlates with Beer's law. Higher CNT concentration produces increased attenuation. However, the linear relationship of attenuation coefficient with MWNT concentration becomes nonlinear for concentrations of 0.5 mg/ml or greater . All results are the mean of five experimental measurements (N=5) with average standard deviation of $\pm 4.4\times10^{-3}$ for the wavelength range of 200-2000 nm. Error bars are not shown for clarity.

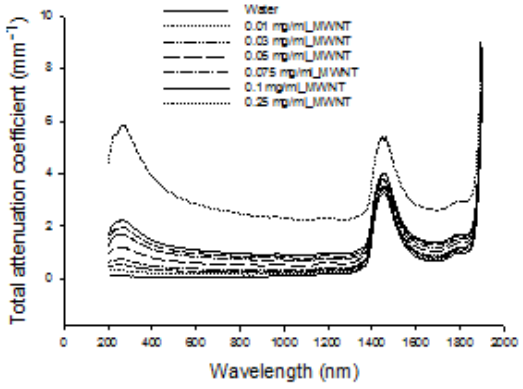
Water
0.01 mg/ml_MWNT
0.03 mg/ml_MWNT
0.05 mg/ml_MWNT
0.075 mg/ml_MWNT
0.1 mg/ml_MWNT
0.25 mg/ml_MWNT
Total attenuation coefficient (mm-1)
Wavelength (nm)

(A)

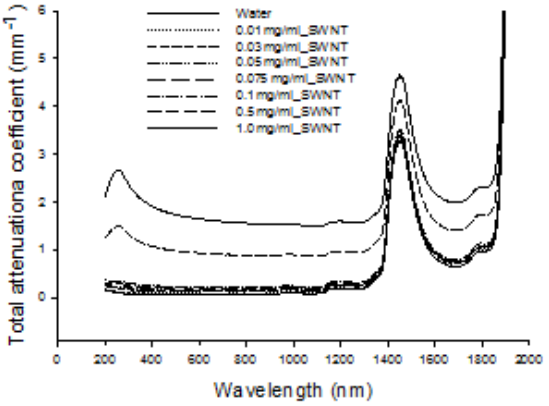
Water
0.01 mg/ml_SWNT
0.03 mg/ml_SWNT
0.05 mg/ml_SWNT
0.075 mg/ml_SWNT
0.1 mg/ml_SWNT
0.5 mg/ml_SWNT
1.0 mg/ml_SWNT
Total attenuationa coefficient (mm-1)
Wavelength (nm)

(B)

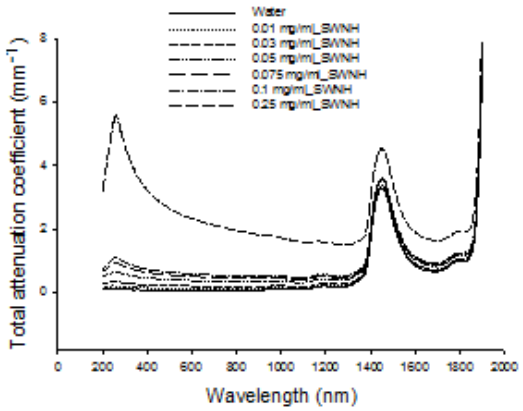
Water
0.01 mg/ml_SWNH
0.03 mg/ml_SWNH
0.05 mg/ml_SWNH
0.075 mg/ml_SWNH
0.1 mg/ml_SWNH
0.25 mg/ml_SWNH
Total attenuation coefficient (mm-1)
Wavelength (nm)

(C)

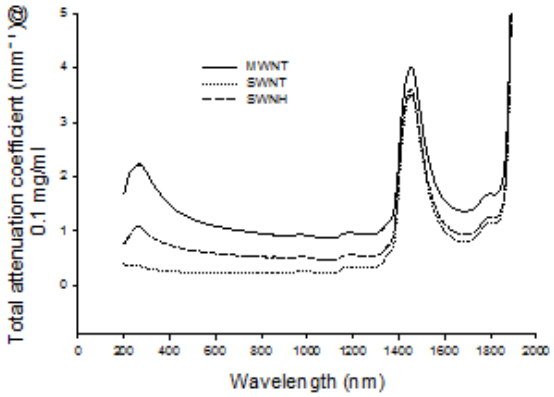
MWNT
SWNT
SWNH
Total attenuation coefficient (mm-1)@
0.1 mg/ml
Wavelength (nm)

(D)

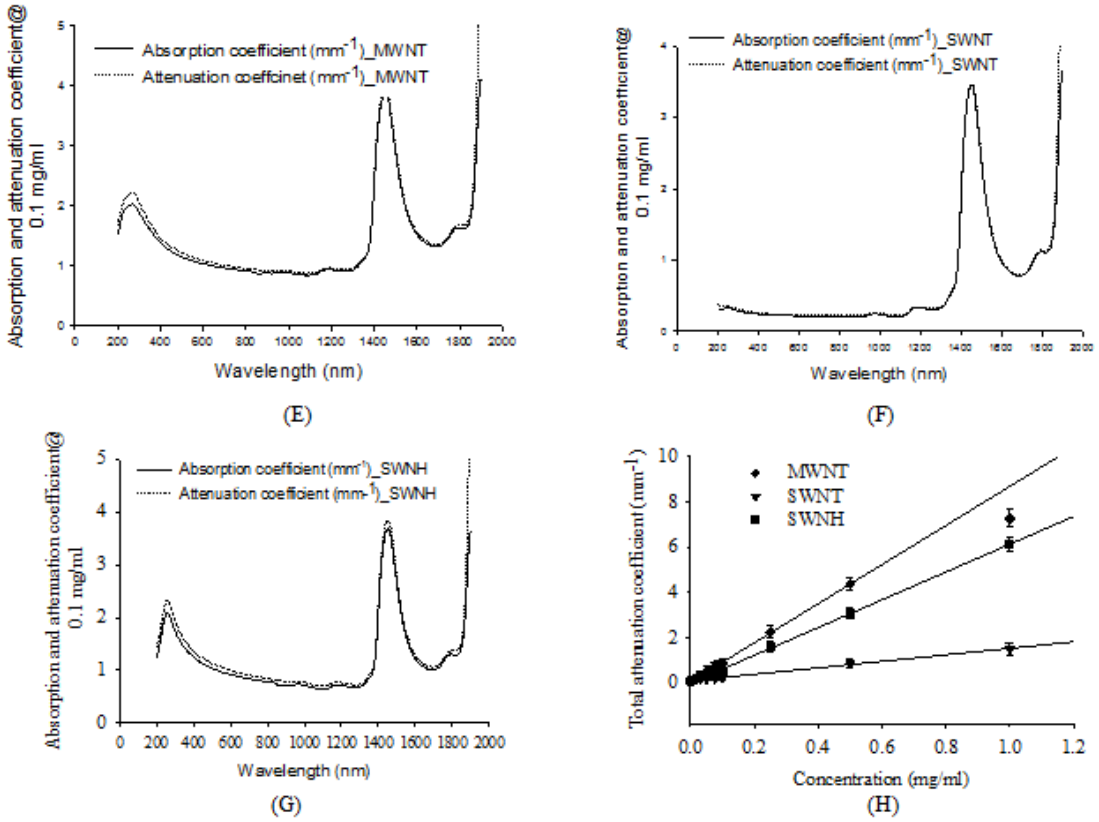

Figure 5.3: Total attenuation coefficients (mm-1) of MWNTs (A), SWNTs (B), and SWNHs (C) in water for varying concentration (0.01-1 mg/ml), attenuation coefficients of MWNTs, SWNHs, and SWNTs in water compared for a concentration of 0.1 mg/ml (D), absorption and attenuation coefficient of MWNTs (E), SWNTs (F), and SWNHs (G) for a CNT concentration of 0.1 mg/ml, and total attenuation coefficient of all three types of CNTs as a function of concentration (H)

5.4.2. Optical Properties of Tissue Phantoms

Diffuse transmittance and reflectance of sodium alginate phantoms incorporated with polystyrene beads (3 μm diameter and 1.0 mg/ml concentration) and talc perfume powder (20 mg/ml and 40 mg/ml) were measured with a spectrophotometer. Figure 5.5A shows the corresponding values of polystyrene beads and talc perfume powder with concentrations of 0.1 mg/ml and 40 mg/ml respectively. The measured transmittance and reflectance were used as inputs to the IAD algorithm and permitted determination of the corresponding absorption and reduced scattering coefficients shown in Figures 5.5 B and C.

Without incorporating polystyrene beads and talc, the absorption coefficients of sodium alginate phantoms (97% water) were found to have a similar absorption spectra and peaks as water at 970 nm and 1200 nm (Figure 5.5 B) [17,131] and scattering was found to be negligible

(Figure 5.5 C). After incorporating polystyrene beads (1.0 mg/ml) in phantoms, both absorption and scttering increased. Inclusion of polystyrene beads alone caused the phantom to possess an absorption coefficient similar to breast cancer tissue, however the reduced scattering coefficient was not sufficient to mimic actual breast cancer tissue. In order to increase the reduced scattering coefficient for the phantoms, talc powder with concentrations of 20 mg/ml and 40 mg/ml was introduced in the phantom in combination with polystyrene beads. For both concentrations of talc, absorption coefficients were unchanged (Figure 5.5 B), however the reduced scattering coefficients increased significantly (Figure 5.5 C). The change in scattering coefficent with varying talc concentrations is represented in Figure 5.5 D. Scattering linearly incresed with greater talc concentration. The final concentration of talc (40 mg/ml) and polystyrene beads (1 mg/ml) in sodium alginate phantoms represent similar optical properties to breast cancer phantoms shown in Figure 5.5 E. All experiments were conducted with five experimental samples (N=5) and all results were considered as the mean of five experimental samples with average standard deviation of ± 0.0124 for the wavelength range of 400-1300 nm.

Absorption and reduced scattering coefficients of breast cancer phantoms were compared with previously published human breast cancer tissue [17,128] at 800 nm and 900 nm in Table 1. At a wavelength of 800 nm, absorption and reduced scattering coefficients of our breast cancer phantoms (μ_a=0.037-0.046 mm^{-1} and μ_s=1.35-1.58 mm^{-1}) are found very close to human breast cancer tissue (μ_a=0.02-0.07 mm^{-1} and μ_s=0.7-1.4 mm^{-1}). The close relationship was also found in the wavelength of 900 nm where the absorption and reduced scattering coefficients of our breast cancer phantom are μ_a=0.044-0.055 mm^{-1} and μ_s=1.22-1.5 mm^{-1} and those for human breast cancer tissue are μ_a=0.05-0.07 mm^{-1} and μ_s=0.8-1.2 mm^{-1}.

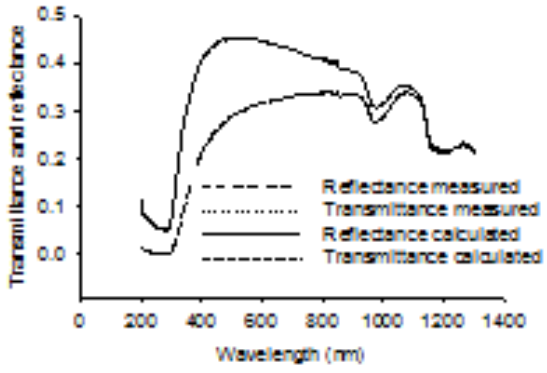
Transmittance and reflectance
Wavelength (nm)
Reflectance measured
Transmittance measured
Reflectance calculated
Transmittance calculated

(A)

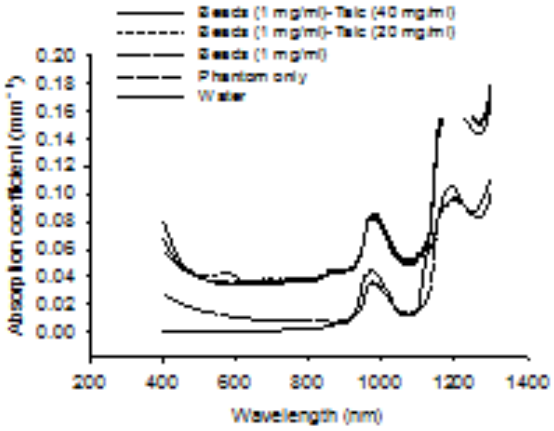
Beads (1 mg/ml)-Talc (40 mg/ml)
Beads (1 mg/ml)-Talc (20 mg/ml)
Beads (1 mg/ml)
Phantom only
Water
Absorption coefficient (mm⁻¹)
Wavelength (nm)

(B)

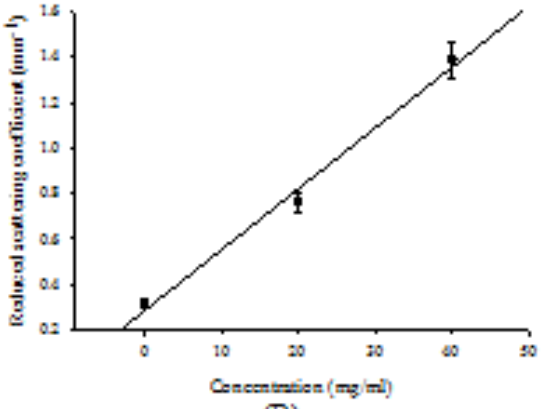
Reduced scattering coefficient (mm⁻¹)
Concentration (mg/ml)

(D)

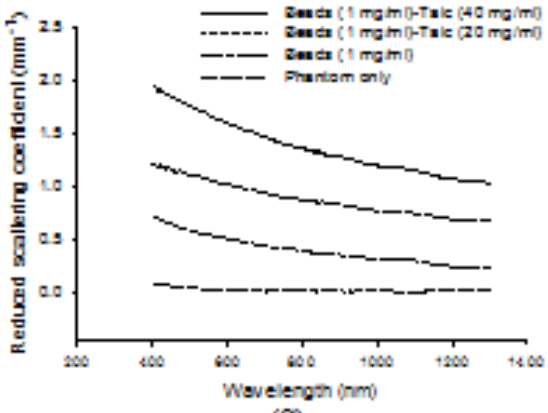
Beads (1 mg/ml)-Talc (40 mg/ml)
Beads (1 mg/ml)-Talc (20 mg/ml)
Beads (1 mg/ml)
Phantom only
Reduced scattering coefficient (mm⁻¹)
Wavelength (nm)

(C)

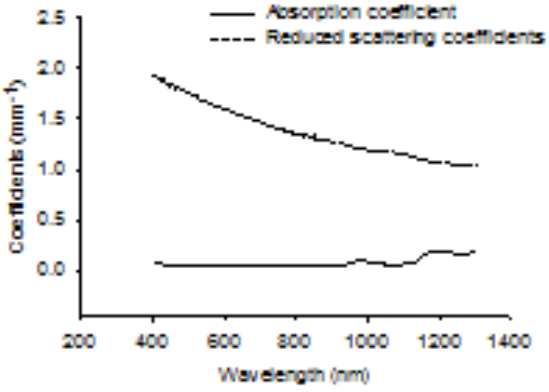
Absorption coefficient
Reduced scattering coefficients
Coefficients (mm⁻¹)
Wavelength (nm)

(E)

Figure 5.4: Transmittance and reflectance of phantoms incorporated with talc powder (1 mg/ml) and polystyrene beads (40 mg/ml) measured with a spectrophotometer and computed by IAD (A). Absorption and reduced scattering coefficients of phantoms with varying concentration of polystyrene beads (0 and 1.0 mg/ml) and talc powder (0, 20, and 40 mg/ml) (B and C). Reduced scattering coefficient as a function of talc powder concentration (D). Absorption and reduced scattering coefficients of sodium alginate phantoms with polystyrene beads (1 mg/ml) and talc (40 mg/ml) computed by the IAD method (E)

Table 5.1: Optical properties of actual breast cancer tissue and breast cancer phantom

Wavelength (nm)	Reduced scattering coefficient (mm^{-1})		Absorption coefficient (mm^{-1})	
	Breast tumors	Breast phantoms	Breast tumors	Breast phantoms
800	0.7-1.4	1.35-1.58	0.02-0.07	0.037-0.046
900	0.8-1.2	1.22-1.5	0.05-0.07	0.044-0.055

5.4.3. Refractive index

The refractive indices (n) of phantoms in combination with polystyrene beads, talc powder, and CNTs were measured with optical coherence tomography (OCT). The values were found to vary between 1.4-1.44 and used as input parameters to the IAD model. Refractive index (1.37) of sodium alginate phantoms without polystyrene beads, talc, and CNTs were measured by Esteban *et al* [61]. Our measured values (refractive index) of breast cancer representative phantoms was higher than Esteban *et al.*, because it contains talc (40 mg/ml) with refractive index, n= 1.586 [132] and polystyrene beads (1 mg/ml) with refractive index, n=1.592 [133] along with sodium alginate (3 g in 100 ml water).

.

5.4.4. Breast cancer phantom-CNT composites

The diffuse transmittance and reflectance of breast cancer phantoms as a function of MWNTs of varying concentration are shown in Figures 5.6A-B respectively. Both transmittance and reflectance decreased with increasing MWNT concentration due to the significant degree of absorption by MWNTs. Absorption and reduced scattering coefficients of phantoms containing

MWNTs are shown in Figures 5.6C-D. These properties were computed by IAD based on measured transmittance and reflectance shown in Figures 5.6A-B.Absorption and scattering coefficients of phantoms containing SWNTs and SWNHs were computed in the similar way and shown in Figures 5.6E-H.

For all types of CNTs, absorption coefficient increases with greater CNT concentration. Inclusion of MWNTs caused the absorption coefficients of phantoms (0.1 mg/ml) to increase by 21 times compared to phantoms without MWNTs (figure 5.6C) at a wavelength of 1064 nm. Absorption coefficients of phantoms containing SWNTs and SWNHs increased by 5 and 9 times respectively for the same concentration (0.1 mg/ml) and wavelength (1064 nm) compared to phantoms without CNTs (Figures 5.6E and 5.6G). Reduced scattering coefficients of phantoms with 0.1 mg/ml CNTs exhibited minor increase with values of 1.2-1.3 greater compared to phantoms without CNTs (Figures 5.6 D, F, and H). Trends described previously were observed for all wavelengths considered. These results suggest that CNTs are predominantly absorbing particles with little contribution to scattering.

The absorption coefficient of phantoms containing varying types of CNTs were compared for an equal concentration 0.05 mg/ml (Figure 5.7A). Phantoms containing MWNTs have the largest absorption coefficients. Absorption of phantoms containing MWNTs is 3.3-3.7 times higher than phantoms containing SWNTs and 1.5-1.6 times higher than phantoms containing SWNHs in the NIR region (800-1200 nm). The absorption coefficient of phantoms with SWNHs is 2-2.4 times higher than phantoms with SWNTs in the NIR. For higher concentration (0.1 mg/ml), MWNTs absorb light approximately 3.8-4 times greater than SWNTs and 1.8-2 times greater than SWNHs. At the same concentration (0.1 mg/ml), light absorption by SWNHs is approximately 1.7-2 times higher than SWNTs.

The absorption coefficients of breast cancer phantoms with CNT inclusion for a range of concentrations (0.0-0.1 mg/ml) of CNTs were found to be linearly related to concentration (Figure 5.8) at a wavelength of 1064 nm. Figure 5.8 can be used as a calibration curve for determining the absorption coefficients of breast cancer tissue or concentration of CNTs of varying type providing either of these parameters are known.

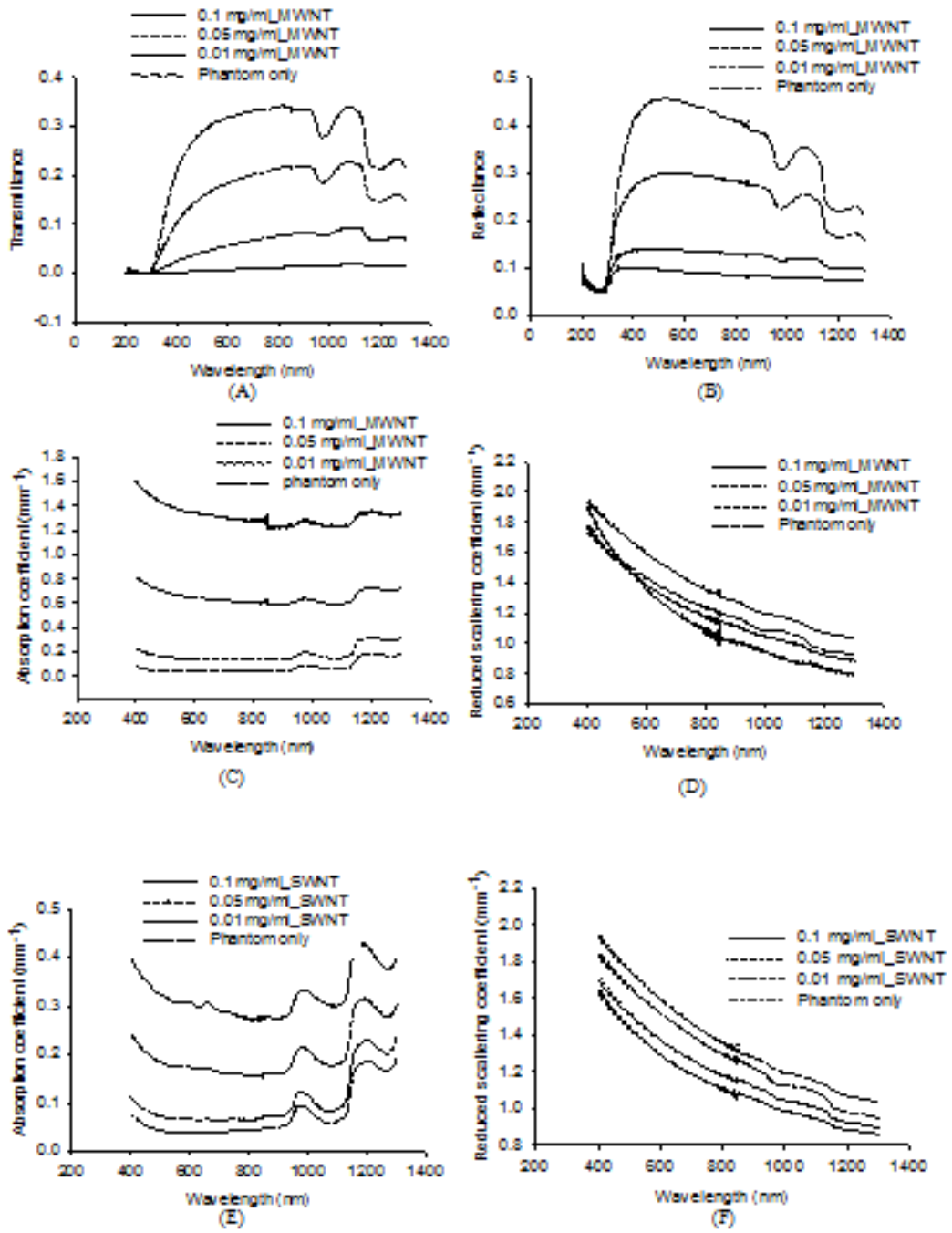

Figure 5.5: Absorption and scattering coefficients of breast cancer phantoms containing MWNTs, SWNTs, and SWNHs determined with the IAD method for the wavelength range of 400-1300 nm

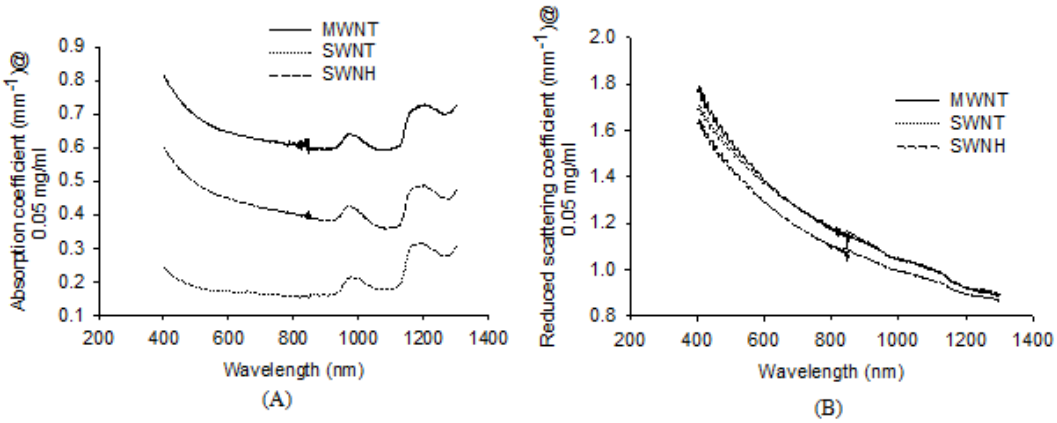

Figure 5.6: Absorption (A) and reduced scattering coefficients (B) of phantoms containing MWNTs, SWNTs, and SWNHs for an identical concentration of 0.05 mg/ml

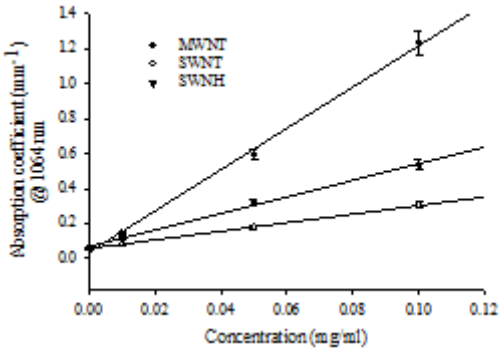

Figure 5.7: Absorption coefficients of phantoms containing varying CNT type as a function of CNT concentration at a wavelength of 1064 nm

5.5. Discussion

Three different types of CNTs were utilized in our experiment to allow comparison of optical properties and permit selection of the most efficient photoabsorbers for photothermal therapy. Although previous studies have measured optical properties including refractive index, absorbance, transmittance, reflectance, and absorption and scattering coefficients of CNTs in solution [26,112-122], this is the first study measuring and comparing the absorption and scattering coefficients of SWNTs, MWNTs, and SWNHs as a function of wavelength and concentration in water and tissue representative phantoms . Since the interfacial contact between CNTs and liquid or solid phantoms may differ, potentially impacting optical properties, both liquid and solid samples were utilized. The dispersion of CNTs in liquid and solid media was

uniform leading to similar behavior by both types of samples. The inclusion of all types of CNTs in water and phantoms significantly increased light absorption.

5.5.1. Optical properties of CNTs in water

The total attenuation coefficient was measured for three types of CNTs in water solutions. Inclusion of all types of CNTs in water for the concentration range (0.01-1 mg/ml) significantly increased the attenuation of light. We demonstrated that the absorption and total attenuation coefficient were nearly identical indicating the scattering effect of CNTs to be negligible (<4%) over the wavelength range of 200-2000 nm (Figures 5.3E-G). Therefore all attenuation coefficients measured for CNTs in water (Figure 5.3A-C) can be represented as absorption coefficients. In our experiments with liquid samples, we found the absorbance of MWNTs to be approximately 4 fold higher than SWNTs at a concentration of 0.1 mg/ml and wavelength of 1064 nm (Figure 5.3D). Previous literature has predicted that the absorbance of MWNTs should be superior to SWNTs which coincides well with our experimental results [24,38]. The absorption of MWNTs is 2 fold higher than SWNHs and SWNHs possess approximately 2 fold higher absorption than SWNTs at the same concentration in water and wavelength.

The linear relationship of attenuation coefficient with CNT concentration in water (Figure 5.3H) satisfies Beer's law [17] which will help to determine any unknown attenuation or absorption coefficient and concentration at a wavelength of 1064 nm providing one of the previously mentioned quantities are known. The linear relationship of attenuation and absorption coefficients is similar to the absorbance study of Kam *el al.* [26], where absorbance of non-covalently functionalized SWNTs in water had a linear relationship with SWNT concentration. However, for MWNTs at a concentration of 0.5 mg/ml or greater the absorption curve became nonlinear no longer complying with Beer's law and prohibiting use of this relation for concentration or absorption coefficient determination.

5.4.2. Model validation

Prior to measuring optical properties of tissue representative phantoms and their CNT composites, optical properties of pig skin was measured in order to validate our experimental

measurement technique and IAD algorithm. Figure 5.8 shows absorption and reduced scattering coefficients of pig epidermis computed by IAD method for the wavelength range of 400-1300 nm. Our measured absorption and reduced scattering coefficients of pig skin (epidermis) were compared with the well known experimental results of Beek *et. al.* [134] at wavelengths of 632.8 nm, 790 nm, and 850 nm. Our results were shown to correlate closely with Beek's work proving the accuracy of our measurement and computational techniques.

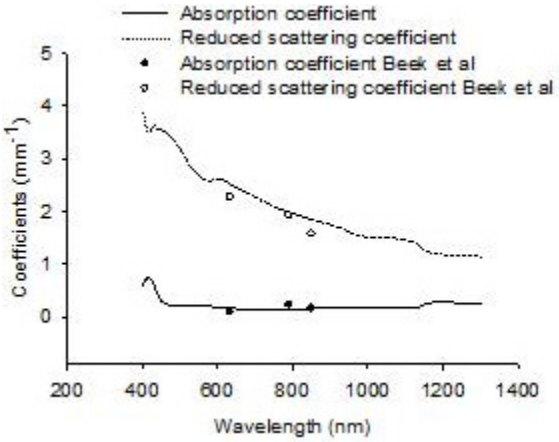

Figure 5. 8: Absorption and reduced scattering coefficients of pig measured by our group and compared to the experimental results of Beek et.al

5.5.2. Breast cancer phantom with CNTs

Since tissue is composed of nearly 85% water, its absorption coefficient is similar but slightly higher than water due to the presence of hemoglobin and protein [17]. The absorption profile of all types of tissue exhibited relative maxima at 970 nm and 1200 nm, which are the characteristics of well-known water absorption peaks [22], However, the light scattering properties vary significantly for different types of tissue due to variation of collagen fibers and blood vessels [135-136]. Sodium alginate which formed the basis for the breast tumor structure is highly transparent with optical properties similar to water. Therefore, in order to mimic breast cancer tissue, we incorporated varying concentrations of highly light scattering particles including polystyrene beads and talc perfume powder in the sodium alginate gel to increase the scattering coefficient of the alginate gel to more effectively match the actual breast tumor scattering properties (Figure 5.5C). The final composition of the breast tumor phantom utilized 1 mg/ml polystyrene beads (3 μm diameter) and 40 mg/ml talc powder in alginate providing a

tissue representative phantom with optical properties close to that of actual breast cancer tissue (Figure 5.5E and Table 5.1). Our breast cancer phantom possessed absorption and reduced scattering coefficients very close to actual breast cancer tumors [17,128] at wavelengths of 800 and 900 nm as shown in Table 5.1.

Inclusion of CNTs in breast cancer phantoms caused the absorption to increase significantly. Absorption coefficients of MWNTs, SWNHs, and SWNTs in phantoms were increased by 21, 9, and 5 fold compared to phantoms without CNTs respectively (Figure 5.6 C, E, and G) for an identical concentration of 0.1 mg/ml and wavelength of 1064 nm. For an identical CNT concentration, the change in reduced scattering coefficient is relatively minor with 1.2-1.3 fold increase compared to phantoms without CNTs (Figure 5.6 D, F, and H).

5.5.3. Comparison of MWNTs, SWNTs, and SWNHs

Phantoms containing MWNTs possess the highest absorption coefficient. MWNTs absorb light approximately 4.5 times greater than SWNTs and 2.2 times greater than SWNHs for a CNT concentration of 0.1 mg/ml in phantoms at the wavelength of 1064 nm (Figure 5.7). A similar phenomenon was observed for CNTs in water, where MWNTs possessed approximately 3.8-4 and 1.86-2 times higher absorption than SWNTs and SWNHs respectively at a concentration of 0.1 mg/ml (Figure 5.3D). Previous literatures predicted that MWNTs may have superior light absorbing capacity compared to SWNTs [24,38,137]. Our study proved this prediction. CNTs in solid and liquid mediums exhibit similar absorption coefficients with small discrepancies. This might be due to the difference of interfacial contacts of CNTs with solids and liquids.

Variation in scattering effects among different types of CNTs is less than 1% for an identical concentration confirming inclusion of CNTs has minimal effect on the scattering properties of a media. The measured optical properties of breast cancer representative phantoms with inclusion of CNTs provides an understanding of the effect of CNTs on the overall optical properties of real tumor tissue. Similar to CNTs in water (Figure 5.3H), the absorption coefficient of solid breast cancer phantoms containing CNTs increase linearly with rising CNT concentrations (Figure 5.8).

5.6. Conclusion

It is anticipated that tumor tissue injected with CNTs will have similar absorption and scattering properties as those determined for tissue representative sodium alginate phantoms incorporated with CNTs. The optical properties determined in this study will provide valuable input parameters for treatment planning models for predicting and optimizing tissue response to photothermal therapies utilized in combination with CNTs.

5.7. Acknowledgements

This research was funded by the following sources: National Science Foundation Grant CBET 0731108, National Institute of Health Grant 1 R21 CA135230-01, and an Institute for Critical Technology and Applied Sciences Grant (ICTAS, Virginia Tech). We would also like to thank Dr. David Geohegan from Oak Ridge National Laboratories for his kind gift of the single walled carbon nanohorns.

Chapter 6: Photothermal effect

This is a standalone chapter. The figures and equation numbers do not correspond with other chapters. The following article **was published in the journal of Biomechanical Engineering, volume 132, pp 1-5, 2010**. The article was written based on the format of above mentioned journal.

Photothermal Response of Tissue Phantoms Containing Multi-Walled Carbon Nanotubes

Saugata Sarkar
Department of Mechanical Engineering,
Virginia Polytechnic Institute and State University, ICTAS Building, Stanger Street, MC0298, Blacksburg, VA 24061
Jessica Fisher
School of Biomedical Engineering and Sciences (SBES), Virginia Polytechnic Institute and State University,
ICTAS Building, Stanger Street, MC0298, Blacksburg, VA 24061

Christopher Rylander
Marissa Nichole Rylander
e-mail: mnr@vt.edu

Department of Mechanical Engineering,
Virginia Polytechnic Institute and State University, ICTAS Building, Stanger Street, MC0298, Blacksburg, VA 24061:
School of Biomedical Engineering and Sciences (SBES),
Virginia Polytechnic Institute and State University, ICTAS Building, Stanger Street, MC0298, Blacksburg, VA 24061

6.1. Abstract

Inclusion of multi-walled carbon nanotubes (MWNTs) into tissue prior to laser therapy has the potential to enhance the selectivity and effectiveness of cancer therapy by providing greater and more controlled thermal deposition. The purpose of this study was to investigate the optical and thermal response of tissue representative phantoms containing MWNTs to optical radiation. Tissue representative phantoms 20 mm in diameter and 1 mm in thickness were created from sodium alginate. Following the inclusion of MWNTs (900 nm in length, 40–60 nm in diameter) in phantoms, the distribution of MWNTs was observed using transmission

electron microscopy. A predominantly, evenly dispersed and randomly oriented distribution of MWNTs was observed with a rare presence of MWNT clustering or clumping. In order to characterize the response of MWNT inclusion on optical properties of phantoms, the transmittance and reflectance spectra of phantoms with and without MWNT inclusion were measured with a spectrophotometer over a wavelength range of 200–1400 nm. Inclusion of MWNTs in phantoms dramatically enhanced light absorption across the entire wavelength range as evidenced by a diminished transmittance and reflectance compared with phantoms without MWNTs. In order to evaluate the spatiotemporal temperature distribution associated with laser irradiation of phantoms with and without MWNTs, the temperature was measured at discrete radial distances from the center of the incident laser beam using thermocouples. The rate of temperature increase and peak temperature for phantoms containing MWNTs was much greater compared with phantoms without MWNTs at all measurement locations. In conclusion, MWNT inclusion in tissue phantoms increases the optical absorption and temperature elevation, which may enable more effective photothermal therapies of human disease utilizing lasers.

6.2. Introduction

More than 1.47×10^6 million men and women have been diagnosed with cancer and over 562,000 people have died of this disease within the United States in 2009 [1]. Laser based hyperthermia therapies can provide a minimally invasive alternative to surgical resection. However, the effectiveness of laser therapies is limited due to nonspecific heating of the target tissue and diffusion limited thermal deposition, which often leads to healthy tissue injury and extended treatment durations. These therapies can be further compromised due to the induction of molecular chaperones called heat shock proteins (HSPs) in tumor regions, where nonlethal temperature elevation occurs. HSP upregulation in cancer cells can lead to enhanced tumor cell viability and tumor recurrence by mitigating apoptosis [2–4] and providing resistance to subsequent chemotherapy and radiation treatments, which are typically used in combination with the initial hyperthermia treatment [2,5–14]. Therefore, a more effective laser therapy may be achieved through enhanced thermal deposition, improved heating selectivity, reduced treatment times and thermal doses, confined tumor injury, and elimination of HSP expression in the tumor. Nanomaterials such as gold nanoshells and carbon nanotubes (CNTs), including single-walled carbon nanotubes (SWNTs) and multi-walled carbon

nanotubes (MWNTs) have received enormous attention recently for their potential role as heat delivery vehicles for laser treatment of tumors. CNTs possess exceptional electronic, electromagnetic, thermal, and chemical properties. Perhaps the most remarkable property of CNTs is their ability to absorb electromagnetic energy (to act as an antenna) in the near infrared (NTR) region of the spectrum [15]. This causes the tubes to oscillate and generate heat. NTR light is transmitted through tissue such as the skin with scattering-limited attenuation and minimal heating. Light within this spectral region has been shown to penetrate tissue at depths beyond 1.6–2.0 mm with irradiance well below the threshold for normal tissue damage [16]. CNTs functionalized with pluronic have been shown to be nontoxic [17]. However, CNTs excited by electromagnetic radiation are capable of generating significant local temperature elevations capable of cell destruction [17–19].

The effectiveness of laser therapies could be greatly enhanced by introducing CNTs into the tissue prior to laser irradiation [20,21]. Optical radiation may be delivered externally to a tissue surface via a free-space beam, or intratumorally with a minimally invasive fiber optic probe. Introducing CNTs into the tissue prior to laser irradiation can increase photothermal heating specificity when CNTs are targeted to tumor cells. Development of effective CNT-mediated laser therapies requires the determination of optimal CNT characteristics and laser parameters for maximum tumor destruction. By integrating CNTs into laser therapy, lower thermal doses can be employed and more selective heating can be achieved, thereby enabling more effective tumor eradication and minimization of healthy tissue destruction. This results in greater temperature elevations within the tumor and increasing tumor injury.

Although gold nanoshells, SWNTs, and MWNTs may enhance the effectiveness of laser therapy due to their capability to act as an antenna and absorb electromagnetic energy, the optical absorption of MWNTs is greater than the other two nanomaterials. Based on the antenna theory, MWNTs can absorb approximately three times as much NIR light as compared with SWNTs [18, 19]. In this study we confined our interest to incorporating MWNTs in tissue representative phantoms in combination with subsequent laser irradiation as a basis for developing future treatments for cancer therapy.

The development of effective combinatorial therapies utilizing lasers and MWNTs requires an understanding of how the introduction of MWNTs into a representative tissue volume affects the optical and thermal properties, and the distribution of MWNTs within

the tissue. Ultimately, the MWNT distribution and modified optical and thermal properties of tissue will have significant impact on the resultant thermal dose distribution and tissue response. Previous studies have measured cellular uptake and MWNT distribution within cell culture models [20, 21]. In these previous studies, unpurified MWNTs (Fe-doped) were added to cells for 24h, and the intracellular distribution of MWNTs was measured with scanning electron microscopy (SEM) and transmission electron microscopy (TEM). These studies confirmed MWNT presence within the cell with localization of MWNTs in the cell membrane, vacuoles, and nucleus. More recent studies have measured MWNT and SWNT distributions in vivo using TEM and Raman Spectroscopy [22, 23]. These studies showed the biodistribution of MWNTs to be time dependent and the localization and concentration of MWNTs in liver, kidney, heart, blood, and skin fluctuated with time. At 24h, the liver exhibited the highest amount of MWNTs compared with other organs. However, no other studies have characterized the MWNT distribution within a tissue representative phantom model and correlated this with optical properties and temperature response.

Prior studies have measured the optical properties of nanoparticles such as gold nanoshells, gold nanorods, SWNTs, and MWNTs in a solution, including the absorbance as a function of the wavelength, characteristic absorption, and scattering coefficients at specific wavelengths [24–26]. Light scattering by MWNTs depends on their distribution in the liquid solution. Homogeneous distributions of MWNTs were found to be less scattering than heterogeneous distribution of MWNTs, in which clustering of MWNTs in a solution occurs [24]. The absorption characteristics of gold nanorods of varying concentrations incorporated within liquid alginate solutions have been measured. It was observed that with higher concentrations of MWNTs, the absorption of the MWNT-alginate composite linearly increased [25]. However, no other studies have characterized the impact of MWNT inclusion on the optical properties of tissue representative structures such as sodium alginate phantoms. This information is critical in predicting the extent of light absorbed by MWNTs in tissue, which ultimately leads to heat generation and relevant therapeutic dose.

The temperature responses of MWNTs in biological solutions or in vitro cell cultures have been measured as a function of the MWNT length, diameter, and concentration [27, 28]. These studies demonstrated the capability of MWNTs to rapidly (within seconds) heat bulk solutions to lethal levels, leading to thermal ablation and cell death. Recent in vivo studies

by our group have characterized kidney tumor response to laser treatment with the inclusion of MWNTs [29]. These studies have further confirmed the ability of MWNT-mediated laser therapies to enhance temperature elevation, diminish HSP expression, and permit definite tumor regression. However, our understanding of the spatiotemporal temperature/injury response is limited, although necessary for effective treatment planning.

The goal of the project was to measure for the first time the MWNT distribution, optical properties, and temperature response to laser irradiation of sodium alginate phantoms containing MWNTs. The MWNT distribution in phantoms was determined using TEM imaging. Optical properties in the form of transmittance and reflectance of phantoms containing MWNTs were measured using a spectrophotometer. The radial dependent temperature response was measured temporally using thermocouples integrated within the phantoms. Knowledge of the MWNT distribution, optical properties of phantoms with MWNT inclusion, and temperature response to phantoms containing MWNTs in a tissue volume will assist with treatment planning and provide necessary information to advance toward animal studies.

6.3. Materials and Methods

6.3.1. MWNT Fabrication

MWNTs were provided by Dave Carroll's group at Wake Forest University and were fabricated by chemical vapor deposition (CVD) with an iron catalyst of 600 mg Fe, as described previously [30, 31]. Briefly, MWNTs were cut by sonication for 20 h in a 3:1 sulfuric-nitric acid solution. This process yielded MWNTs with a length of 900 nm, which was verified by TEM. This length was used because of its ability to couple to NTR light, as described by the antennae theory and shown in previous work [30–32]. MWNTs were later filtered and dried. Then, MWNTs were made water soluble using 1% Pluronic 127 with a final stock solution of 2 mg/ml and sonicated for 20 min. The resulting solution was autoclaved for 20 min for sterilization.

6.3.2. Tissue Phantom Creation

Sodium alginate phantoms were used as a representative tissue model since they can have similar thermal and optical properties to human tissue. Tissue phantoms also

provided a three dimensional tissue volume for characterizing MWNT distribution as well as photothermal heat generation and diffusion. Tissue representative phantoms were composed of sodium alginate Protanal LF 10/60 (FMC Biopolymer, Drammen, Norway), which is derived from brown algae. Sodium alginate is a low viscosity alginate with a mean guluronate/mannuronate (G/M) ratio of 70% and mean molecular weight of 180 kDa [33, 34]. Sodium alginate was stirred vigorously with deionized water to a 3% w/v concentration (3 g/100 ml) for 1 h. The alginate was sterile filtered through a 0.45 m membrane. A MWNT solution (0.1 mg/ml) dissolved in pluronic was uniformly mixed with the liquid sodium alginate solution to yield a 0.1 mg/ml MWNT concentration. Phantoms were then cross-linked using 80 mM calcium chloride for 20 min. Phantoms of 20 mm diameter and 1 mm thickness were constructed and utilized for optical and temperature measurements.

6.3.2. TEM Imaging of the MWNT Distribution

TEM was utilized to image the MWNT distribution within phantoms. Phantoms were sectioned in depth every 5 mm by a microtome into tissue samples of 50–60 nm in thickness. Tissue sections were stained with 2% Uranyl acetate for 12 min to increase the TEM image contrast. Samples were then rinsed with deionized water after staining and dried. The MWNT distribution within phantoms was imaged for each section using a high resolution Zeiss 10CA TEM (Carl Zeiss SMT Inc., Peabody, MA). Images were recorded at 60 KV and 40,000 X magnifications.

6.3.3. Optical Property Measurement

In order to determine the ability of MWNTs to enhance the light absorption necessary for heat generation, the diffuse reflectance and diffuse transmittance values of phantoms alone or with inclusion of MWNTs at 0.1 mg/ml concentration was measured. A Cary-5000 spectrophotometer with a diffuse reflectance accessory (DRA) was used to measure the diffuse transmittance and diffuse reflectance of phantoms in the wavelength range of 200–1400 nm. The DRA is an integrating sphere, which collects and permits detection of light, which is transmitted or reflected at high angles from the phantom surface. To measure the diffuse transmittance, the phantoms were placed at the light entrance port of the DRA. Diffuse reflectance was measured by placing the phantom at the light exit port of the DRA, while not obstructing the entrance port. The absorbance of phantoms with and without MWNTs was

determined from the measurements of transmittance and reflectance according to the following relationship:

absorbance = 1 − transmittance − reflectance.

6.3.4. Temperature Measurement.

A continuous wave diode-pumped fiber laser with a wavelength of 1064 nm and collimated beam diameter of 5 mm (YLD-5-1064-LP, IPG Photonics, Santa Clara, CA) was used to irradiate phantoms with and without MWNTs. A laser irradiance of 15.3 W/cm2 and heating duration of 45s were employed. Light was coupled to a fiber optic probe that provided collimated incident light on the center of the top surface of the phantom. Four hypodermic thermocouples (Omega Engineering, Inc., Stamford, CT) were placed within the phantom at radial positions of 3 mm, 4 mm, 6 mm, and 7 mm from the center of the phantom inserted at a depth of 1.0 mm for real-time temperature measurements during laser irradiation (Fig. 1). A National Instruments thermocouple reader (USB-9211) and VI LOGGER LITE software were used to record the temperature data during the experiments.

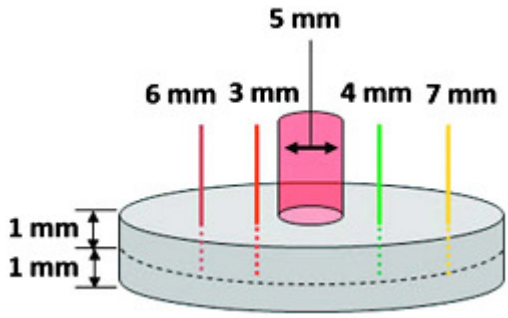

Figure 6.1: Phantom geometry denoting laser beam diameter and thermocouple positions

6.4. Results

6.4.1. Phantom Creation

Sodium alginate phantoms with and without inclusion of MWNTs were successfully created. The dramatic difference in the optical properties is evident between the completely black phantom containing MWNTs and the translucent/white non-MWNT containing phantom, as shown in Fig. 2. From a macroscopic perspective the MWNT distribution appears homogenous,

although transmission electron microscopy is required to truly visualize the MWNT distribution in the phantom.

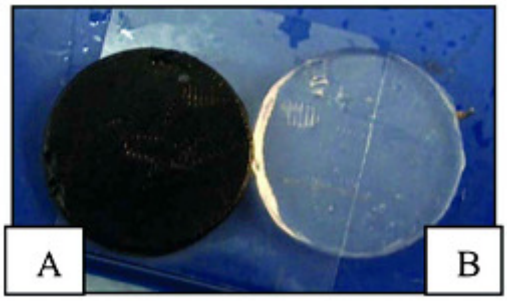

Figure 6.2: Sodium alginate phantom (a) with MWNT inclusion and (b) without MWNTs

6.4.2. MWNT Distribution in Phantoms

TEM images of a sodium alginate phantom alone or with inclusion of MWNTs are depicted in Figs. 3 (*a*) and 3 (*b*), respectively. A distinct fiber distribution associated with the presence of sodium alginate polymer chains can be observed in the phantom without MWNTs [35]. The presence of MWNTs in the phantom can be distinctly identified as dark cylinders within the alginate matrix in Fig. 3 (*b*). The distribution of MWNTs was predominantly observed to be evenly dispersed and randomly distributed throughout the phantom. Infrequent clusters or clumps of MWNTs with diameters on the order of several hundred nanometers were also noted. The diameter of individual MWNTs varied from 40 nm to 60 nm.

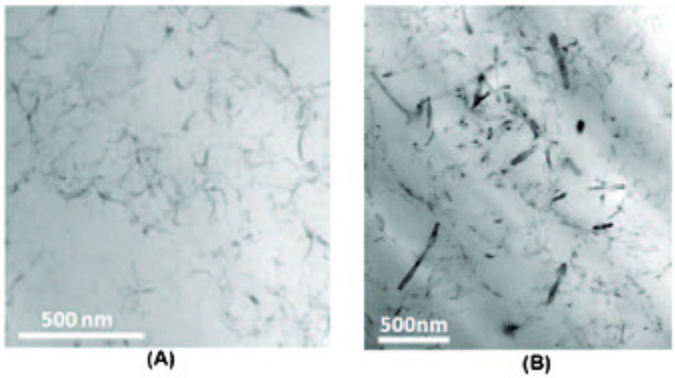

Figure 6.3: TEM images of (a) sodium alginate phantom alone and (b) with inclusion of MWNTs

6.4.3. Optical Property Measurement.

Figure 4 depicts the measured transmittance (Fig. 4 (*a*) and reflectance (Fig. 4(*b*) of phantoms with and without inclusion of MWNTs (concentration of 0.1 mg/ml) for a wavelength range of 200–400 nm. Inclusion of MWNTs in the phantom dramatically increased its ability to absorb light, thereby decreasing the light transmitted through the phantom. This is evidenced by the diminished transmittance of light through the phantoms containing MWNTs compared with phantoms without MWNTs (Fig. 4 (*a*). Due to the scattering of light by sodium alginate phantoms, these phantoms exhibit a varying degree of reflectance as a function of the wavelength. Light scattering is due to internal refraction of photons at the interface of alginate chains and surrounding aqueous sodium chloride solution. Phantoms containing MWNTs have a higher light absorption owing to the MWNTs, and therefore, reduce the reflectance profile compared with phantoms without MWNTs, as shown in Fig. 4 (*b*). The calculated absorbance spectra (absorbance=1−transmittance−reflectance) for phantoms with and without MWNTs is plotted in Fig. 4 (*c*). The absorbance profile of phantoms exhibited relative maxima at 970 nm and 1200 nm, as shown in Fig. 4 (*c*), which are characteristics of well-known water absorption peaks [36]. For shorter wavelengths of 200–00 nm, absorbance is also high, owing to sodium alginate chains. The presence of MWNTs in phantoms greatly increases absorbance for the overall wavelengths measured (200–400 nm).

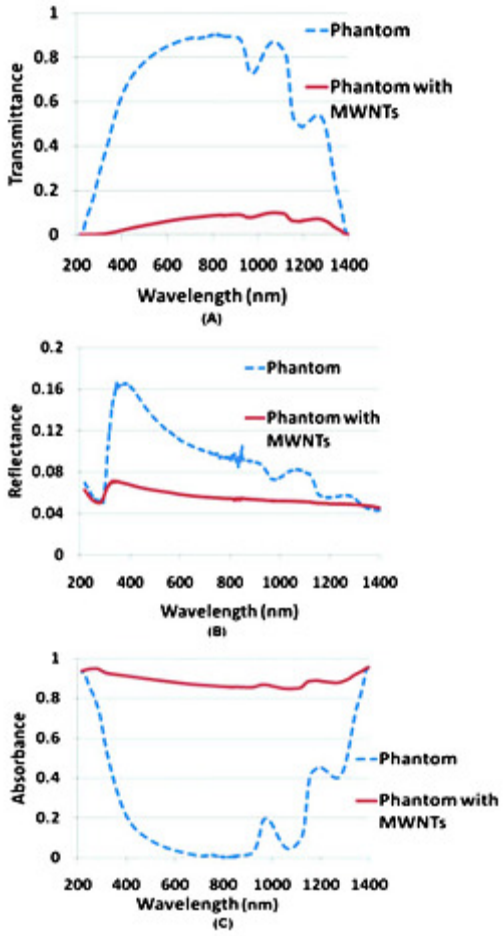

Figure 6.4: (a) Transmittance, (b) reflectance, and (c) absorbance of phantoms with and without MWNTs

6.4.4. Temperature Response

The dynamic temperature response at four discrete radial positions within the phantoms during laser irradiation (15.3 W/cm2 for 45 s) is depicted in Fig. 5. The rate of temperature rise and peak temperature for phantoms containing MWNTs was much greater compared with phantoms without MWNTs for all locations. As expected, there is a radial dependence of temperature in phantoms with and without MWNTs, with higher temperature rises observed closer to the center of the phantom where laser irradiation occurred. Direct coupling of laser light with MWNTs can be distinctly observed in the rapid heating rate and temperature elevation observed at the 3 mm radial position from the phantom center. At this location, the peak temperature observed for phantoms with and without MWNTs was 65°C and 32°C, respectively.

At radial positions of 4 mm, 6 mm, and 7 mm from the phantom center, the rate of heating is very similar for phantoms containing MWNTs.

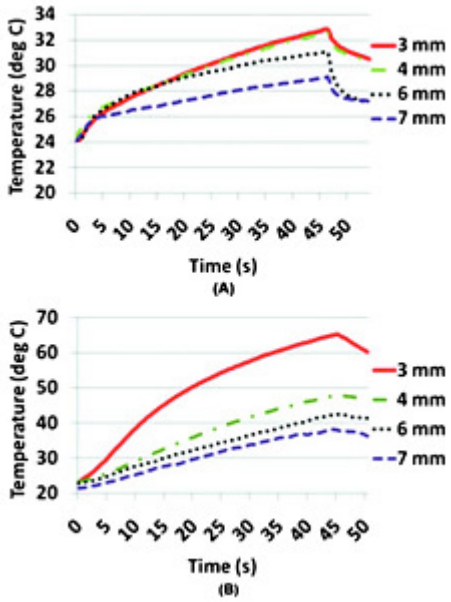

Figure 6.5: Temperature response of (a) phantoms alone or (b) with inclusion of MWNTs at 3 mm, 4 mm, 6 mm, and 7 mm from the center at a depth of 1 mm during laser irradiation at 15.3 W/cm2 for 45 s

6.5. Discussion

This study demonstrated the dramatic increase in laser photothermal deposition provided by incorporating MWNTs into tissue representative phantoms. Although other studies have discussed the antenna properties of MWNTs and have shown their capability for enhancing laser therapy effectiveness in cell culture models [17, 27], this is the first study to measure the temperature responses to laser irradiation of MWNTs incorporated into sodium alginate phantoms. Furthermore, this study provided the first characterization of MWNT distribution in phantoms and measurement of the transmittance and reflectance of phantoms containing MWNTs.

6.5.1. TEM Distribution

Based on the TEM measurements, the distribution of MWNTs in phantoms was found to be evenly dispersed and randomly distributed with minor clustering of MWNTs observed. MWNTs are highly hydrophobic in nature, thereby potentially leading to potential aggregation clustering or clumping when introduced into biological solutions. The evenly dispersed distribution of MWNTs in phantoms attests to the ability of surface fictionalization with pluronic to successfully suspend MWNTs in the solution. The presence and degree of clumping of MWNTs can have a significant impact on their optical and thermal properties when utilized in laser therapy, thereby significantly affecting treatment outcome. Prior studies using MWNTs have documented a direct relationship between clustering of MWNTs with time to increased scattering measured with a spectrophotometer [24]. The thermal diffusion properties of nanoparticleswill also be altered by clustering, which can be embodied in changes in the thermal conductivity. Within MWNT clusters the resistance to heat transfer is diminished, leading to high rates of thermal diffusion. However, when clusters are distributed throughout the phantom, typically significant distances exist between them, causing the resistance to heat flow between the clusters to be high and the thermal conductivity of the overall composite to be reduced. Clumping of MWNTs within a phantom or tissue may significantly reduce the uniformity of heat generation and diffusion.

Knowledge of the MWNT distribution in tissue phantoms will provide a basis for future development of realistic treatment planning models for combinatorial therapies involving lasers and MWNTs. On a size scale comparable to the nanoparticles, MWNTs are randomly oriented and distributed throughout the tissue phantom. However, from a macroscopic prospective, MWNTs can be perceived as uniformly dispersed. In future model development, the entire phantom may be assigned bulk material properties of a MWNT-composite. If the distribution of MWNTs in the tissue representative phantom had not been evenly dispersed on a macroscopic scale, the computational model would require more sophistication in which unique distributions of MWNTs in the phantom model would be represented. The material properties would vary depending on the composition and concentration of MWNTs in various locations of the phantom. We acknowledge that the measurement of the MWNT distribution within *in vivo* systems will possess added complexity due to the presence of perfusion and lymphatic flow, which will cause

the distribution of MWNTs to vary spatiotemporally. However, this study provides an initial basis for the formulation of representative computational models for understanding the spatiotemporal heat diffusion associated with laser irradiation of MWNTs in tissue phantoms.

6.5.2. Optical Properties

Inclusion of MWNTs in sodium alginate phantoms significantly increased their ability to absorb light for the spectrum of 200–1400 nm. Much lower levels of the diffuse transmittance and reflectance in the phantoms containing MWNTs indicated higher levels of absorption for all wavelengths considered. Our results correspond with prior studies, which demonstrated the capability of MWNTs to enhance light absorption when incorporated into the solution 30. The absorption capability of MWNTs in the solution has been shown to be nearly three times greater compared with SWNTs based on the antenna theory and experimental measurements 30. In the future, the measured transmittance and reflectance data will be incorporated into an inverse adding doubling algorithm to determine the absorption and scattering coefficients for phantoms containing MWNTs. Ultimately, absorption and scattering coefficients will be utilized as inputs into a Monte Carlo model to determine the fluence distribution created by laser irradiation of MWNTs in a representative tissue volume. Knowledge of the fluence will permit determination of the temperature distribution within the tissue volume, which is necessary for effective treatment planning.

6.5.3. Temperature

The presence of MWNTs within sodium alginate phantoms increased optical absorption, photothermal heat generation, and heat diffusion throughout the phantom measurement region, causing substantial increases in temperature elevation compared with phantoms without MWNTs. Therefore, laser irradiation of tissues containing MWNTs could permit the attainment of lethal temperatures throughout a greater region, potentially enabling the treatment of larger tissue volumes. Recent *in vivo* studies by our group, in which MWNTs were introduced into mouse kidney tumors 24 h prior to laser irradiation, confirmed higher temperature elevations throughout a larger tumor volume compared with tumors laser treated without MWNT inclusion. Subsequent tumor regression and elimination of HSPs were observed only when MWNTs were

used in combination with laser irradiation [29]. However, the potential of MWNTs for enhancing treatment selectivity can only be achieved through direct targeting of MWNTs to tumor cells. Targeting of MWNTs to tumor cells would enable laser irradiation to create localized zones of temperature elevation necessary for causing selective tumor cell death while preserving the surrounding healthy tissue. The folate receptor is a high affinity membrane folate-binding protein, which is frequently over expressed in a wide variety of cancer cells compared with normal cells, making it an attractive target for MWNT tumor specific MWNT delivery [37]. In a prior study, SWNTs were functionalized with phospholipids with polyethylene glycol moiety, with folic acid terminal group, for selective binding to folate receptors overexpressed on HeLa cells, and CY3-DNA for imaging of SWNT location [28]. This strategy may be utilized by our group in the future to permit selective heat generation and tumor destruction.

6.6. Acknowledgment

This research was funded by the National Science Foundation Grant No. CBET-0731108 and National Institutes of Health Grant Nos. RO1CA12842 and 1 R21 CA135230-01. We would like to thank Xuanfeng Ding from David Carroll's group at Wake Forest University, who synthesized the MWNTs used in the phantom experiments. The content is solely the responsibility of the authors and does not necessarily represent the official views of the National Science Foundation or the National Institutes of Health.

References

1. Gittes, R., 1991, "Carcinoma of the Prostate," N. Engl. J. Med., **324**, pp.236–245.

2. Kiang, J. G., and Tsokos, G. C., 1998, "Heat Shock Protein 70 kDa: Molecular Biology, Biochemistry, and Physiology," Pharmacol. Ther., **80**, pp. 183–201.

3. 1991, *Apoptosis: The Molecular Basis of Cell Death*, L. D. Tomei and F. O. Cope, eds., Cold Spring Harbor Laboratory, Plainview, NY.

4. Calderwood, S. K., Khaleque, M. A., Sawyer, D. B., and Ciocca, D. R., 2006, "Heat Shock Proteins in Cancer: Chaperones of Tumorigenesis," Trends Biochem. Sci., **31**, pp. 164–72.

5. Gibbons, N. B., Watson, R. W., Coffey, R. N., Brady, H. P., and Fitzpatrick, J. M., 2000, "Heat-Shock Proteins Inhibit Induction of Prostate Cancer Cell Apoptosis.

Prostate," Prostate, **45**, pp. 58–65.

6. Levine, A. J., Momand, J., and Finlay, C. A., 1991, "The p53 Tumour Suppressor Gene," Nature _London_, **351**, pp. 453–456.

7. Sõti, C., Nagy, E., Giricz, Z., Vigh, L., Csermely, P., and Ferdinandy, P., 2005, "Heat Shock Proteins as Emerging Therapeutic Targets," Br. J. Pharmacol., **146**, pp. 769–780.

8. Georgopoulos, C., and Welch, W. J., 1993, "Role of the Major Heat Shock Proteins as Molecular Chaperones," Annu. Rev. Cell Biol., **9**, pp. 601–634.

9. Martin, J., Horwich, A. L., and Hartl, F. U., 1992, "Prevention of Protein Denaturation Under Heat Stress by the Chaperonin HSP60," Science, **258**, pp. 995–998.

10. Wiech, H., Buchner, J., Zimmermann, R., and Jakob, U., 1992, "HSP90 Chaperones Protein Folding In Vitro," Nature _London_, **358**, pp. 169–170.

11. Ciocca, D. R., Clark, G. M., Tandon, A. K., Fuqua, S. A., Welch, W. J., and McGuire, W. L., 1993, "Heat Shock Protein HSP70 in Patients With Axillary Lymph Node-Negative Breast Cancer: Prognostic Implications," J. Natl. Cancer Inst., **85**, pp. 570–574.

12. Rylander, M., Feng, Y., and Diller, K., 2006, "Optimizing Heat Shock Protein Expression Induced Byprostate Cancer Laser Therapy Through Predictive Computational Models," J. Biomed. Opt., **11**_4_, p. 041113.

13. Madersbacher, S., Grobl, M., Kramer, G., Dirnhofer, S., Steiner, G., and Marberger, M., 1998, "Regulation of Heat Shock Protein 27 Expression of Prostatic Cells in Response to Heat Treatment," Prostate, **37**, pp. 174–181.

14. Roigas, J., Wallen, E. S., Loening, S. A., and Moseley, P. L., 1998, "Effects of Combined Treatment of Chemotherapeutics and Hyperthermia on Survival and the Regulation of Heat Shock Proteins in Dunning R3327 Prostate Carcinoma Cells," Prostate, **34**, pp. 195–202.

15. Poole, D., 2003, *Introduction to Nanotechnology*, Wiley, Hoboken, NJ.

16. Anderson, R., and John, A., 1981, "The Optics of Human Skin," J. Invest. Dermatol., **77**, pp. 13–19.

17. Fisher, J., and Rylander, M., 2008, "Effective Cancer Laser Therapy Design Through the Integration of Nanotechnology and Computational Treatment Planning Model," Proc. SPIE, **6869**, pp. 1–11.

18. Webster, S., Maultzsch, J., Thomsen, C., Liu, J., Czerw, R., Terrones, M., Adar, F., John, C., Whitely, A., and Carroll, L., 2003, "Raman Characterization of Nitrogen Doped Multiwalled Carbon Nanotubes," *MRS Symposium*
Proceedings, P. Bernier, D. Carroll, G. T. Kim, and S. Roth, eds., Materials Research Society, Warrendale, PA, Vol. 772, pp. 129–134.
19. Xu, J., Xiao, M., Czerw, R., and Carroll, L., 2004, "Optical Limiting and Enhanced Optical Nonlinearity in Doped Carbon Nanotubes," Chem. Phys. Lett., **389**, pp. 247–250.
20. Cheng, C., Muller, K., Koziol, K., Skepper, J., Midgley, P., Welland, M., and Porter, A., 2009, "Toxicity and Imaging of Multi-Walled Carbon Nanotubes in Human Macrophages Cells," Biomaterials, **30**, pp. 4152–4160.
21. Monteiro-Riviere, N., Nemanich, R., Inman, A., Wang, Y., and Riviere, J., 2005, "Multi-Walled Carbon Nanotube Interactions With Human Epidermal Keratinocytes," Toxicol. Lett., **155**, pp. 377–384.
22. Guo, J., Zhang, X., Li, Q., and Li, W., 2007, "Biodistribution of Functionalized Multiwall Carbon Nanotubes in Mice," Nucl. Med. Biol., **34**, pp. 579–583.
23. Liu, Z., Cai, W., He, L., Nakayama, N., Chen, K., Sun, X., and Dai, H., 2007, "In Vivo Biodistribution and Highly Efficient Tumor Targeting of Carbon Nanotubes in Mice," Nat. Nanotechnol., **2**, pp. 47–52.
24. Saltiel, C., and Manickavasagam, S., 2005, "Light-Scattering and Dispersion Behavior of Multiwalled Carbon Nanotubes," J. Opt. Soc. Am. A Opt. Image Sci. Vis, **22**, pp. 1546–1554.
25. Pal, A., and Pal, T., 2005, "Preparation of Nanosized Gold Nanoparticle in a Biopolymer Using UV Photosctivation," J. Colloid Interface Sci., **288**, pp. 396–401.
26. Yang, Y., and Li, J., 2007, "Assembled Alginate/Chitosan Nanotubes for Biological Application," Biomaterials, **28**, pp. 3083–3090.
27. Torti, S., Byrne, F., and Whelan, O., 2007, "Thermal Ablation Therapeutics Based on CNx Multi-Walled Nanotubes," Int. J. Nanomedicine, **2007:2**_4_, pp. 707–714.
28. Kam, N., O'Connell, M., Wisdom, J., and Dai, H., 2005, "Carbon Nanotubes as Multifunctional Biological Transporters and Near-Infrared Agents for Selective Cancer Cell Destruction," Proc. Natl. Acad. Sci. U.S.A., **102**, pp. 11600–11605.
29. Burke, A., Ding, X., Singh, R., Kraft, R., Levi-Polyachenko, N., Rylander, M., Szot, C., Buchanan, C., Whitney, J., Fisher, J., Hatcher, H., Agostino, R., Kock, N., Ajayan, P., Carroll,

D., Akman, S., Torti, F., and Torti, S., 2009, "Long-Term Survival Following a Single Treatment of Kidney Tumor With Multi-Walled Carbon Nanotubes and Near-Infrared Radiation," Proc. Natl. Acad. Sci. U.S.A., **106**, pp. 12897–12902.

30. Torti, S., Byrne, F., Whelan, O., Ucer, B., Schmid, M., Torti, F., Akman, F., Levi, N., Liu, J., Ajayan, P., Nalamasu, O., and Carroll, D., 2007, "Photo- Dynamic Therapeutics Based on CNx Multi-Walled Nanotubes," Nanomedicine, **4**, pp. 707–714.

31. Hanson, G., 2005, "Fundamental Transmitting Properties of Carbon Nanotube Antennas," IEEE Trans. Antennas Propag., **53**, pp. 3426–3435.

32. Wang, Y., Kempa, K., Kimball, B., Carlson, J., Benham, G., Li, W., Kempa, T., Rybczynski, J., Herczynski, A., and Ren, Z., 2004, "Receiving and Transmitting Light-Like Radio Waves: Antenna Effect in Arrays of Aligned Carbon Nanotubes," Appl. Phys. Lett., **85**, pp. 2607–2609.

33. Wong, M., 2003, *Alginates in Tissue Engineering*, Humana Press Inc., Totowa,
NJ, Vol. 238, pp. 77–86.

34. Fisher, F., and Rylander, M., 2008, "Effective Cancer Laser Therapy Design Through the Integration of Nanotechnology and Computational Treatment Planning Models," Proc. SPIE, **6869**, pp. 68690D.

35. Yang, L., Zhang, B., and Zhang, L., 2007, "Amphiphilic Cholesteryl Grafted Sodium Alginate Derivative: Synthesis and Self-Assembly in Aqueous Solution," Carbohydr. Polym., **68**, pp. 218–225.

36. Hale, G. M., and Query, M. R., 1973, "Optical Constants of Water in the 200-nm to 200-μm Wavelength Region," Appl. Opt., **12**, pp. 555–563.

37. Sudimack, J., and Lee, R. J., 2000, "Targeted Drug Delivery via the Folate Receptor," Adv. Drug Delivery Rev., **41**_2_, pp. 147–162.

Chapter 7: Photochemical effect

The following article will be submitted in the **Nano Letters** following and The article was written based on the format of above mentioned journal.

The Generation of Reactive Oxygen Species by Photoexcitation of Single Walled Carbon Nanotubes

Saugata Sarkar[1], James Mahaney[2], Harry Dorn[3], Jianfei Zhang[3], Marissa Nichole Rylander[1]
[1]Department of Mechanical and School of Biomedical Engineering, Virginia Tech, Blacksburg, VA 24061.
[2]Edward Via College of Osteopathic Medicine – Virginia Campus, Blacksburg, VA 24060.
[3]Department of Chemistry, Virginia Tech, Blacksburg, VA 24061.

7.1. Abstract

In this paper, MWNTs, SWNTS, SWNHs, peapods (SWNT-Gd) were investigated for their ability to generate reactive oxygen species (ROS) following laser irradiation. SWNHs are shown to produce ROS following laser irradiation, which could provide a means for photochemical-based tumor destruction. Other types of CNTs generate a small amount of ROS compared to SWNHs. Higher laser power generates a higher amount of ROS. We have utilized spin-trap electron paramagnetic resonance (EPR) spectroscopy to investigate the generation of ROS from CNTs following laser excitation (wavelength 1064 nm). A continuous beam Nd-YAG laser was utilized to photo-excite CNTs in a solution containing the spin trap 5,5-dimethyl-1-pyrroline N-oxide (DMPO). In the presence of the electron donor NADH, we detected the predominant presence of trapped hydroxyl radical (•OH), but also a trace of the trapped super oxide (O2•-) radical. We did not observe trapped species in the absence of the electron donor, NADH or in the absence of laser irradiation. The results are discussed in terms of a model where laser-irradiation of SWNHs generated singlet oxygen ($^1O_2$), which was converted to O_2•- using NADH as an electron source.

KEYWORDS Free radicals, reactive oxygen species, EPR, carbon nanotubes, carbon nanohorns, cancer therapy

7.2. Introduction

Under laser light excitation, many types of fullerenes (C_{60}, C_{70}, C_{76}, C_{80}, and C_{84}) have been shown to generate reactive oxygen species (ROS), including superoxide ($O_2^{\bullet-}$) and hydroxyl radical (•OH) [67-70]. For example, Zhao *et al.* [15] measured ROS production during excitation (wavelength > 400 nm) of C_{60} in water solution with a Xenon arc lamp. Significant evidence of super oxide anion radical (O_2^-), hydroxyl radical (•OH), and C_{60} anion radicals (C_{60}^*) were observed in the presence of nicotinamde adenine dinucleotide (NADH). Yamakoshi *et al.* measured ROS generation by C_{60} in water solution following photo reflector lamp irradiation and found a significant amount of ROS signal in the presence of NADH [67]. Both Zhao *et al.* and Yamakoshi *et al.* did not observe any ROS in C_{60} solutions without light irradiation. During laser excitation, C_{60} absorbs a photon producing the $^1C_{60}$* excited state, which converts spontaneously to the $^3C_{60}$* triplet excited state. In the presence of molecular oxygen, $^3C_{60}$* can be converted back to the ground state, $^1C_{60}$, producing singlet oxygen ($^1O_2$) (equation 1), and singlet oxygen can be converted to the superoxide radical $O_2^{\bullet-}$ by accepting an electron from an electron donor, such as NADH [138-139].

$$^1C_{60} \xrightarrow{h\upsilon} {}^1C_{60}^* \longrightarrow {}^3C_{60}^* \overset{{}^3O_2 \;\; {}^1O_2}{\longrightarrow} {}^1C_{60} \qquad (7.1)$$

Because carbon nanotubes (CNTs) are chemically and physically similar to fullerenes, they may also generate ROS when irradiated by laser light. To test this possibility, we have utilized the spin-trap EPR method [16,140-141] to detect and identify ROS produced following laser-irradiation of CNTs in the presence of NADH. For this experiment, we used multi-walled carbon nanotubes (MWNTs), single-walled carbon nanotubes (SWNTs), and single walled carbon nanohorns (SWNHs) to investigate ROS generation.

CNTs in the form MWNTs, SWNTs, and SWNHs (Figure 7.1) have been previously shown to serve as effective photothermal enhancers [22-23,142] for laser cancer therapy by absorbing a significant amount of light, generating heat, and causing tumor cell death when excited by infrared laser light. However, if CNTs can be shown to produce ROS free radicals, they may provide multimodal therapeutic benefit as both photothermal and photochemical enhancers for more effective cancer treatment. The purpose of our study was to determine

whether photoexcitation of CNTs could indeed generate ROS free radicals. Herein, we detected and identified the free radicals generated during laser irradiation of CNTs in solution and proposed the mechanism by which laser irradiation of CNTs leads to cancer cell damage.

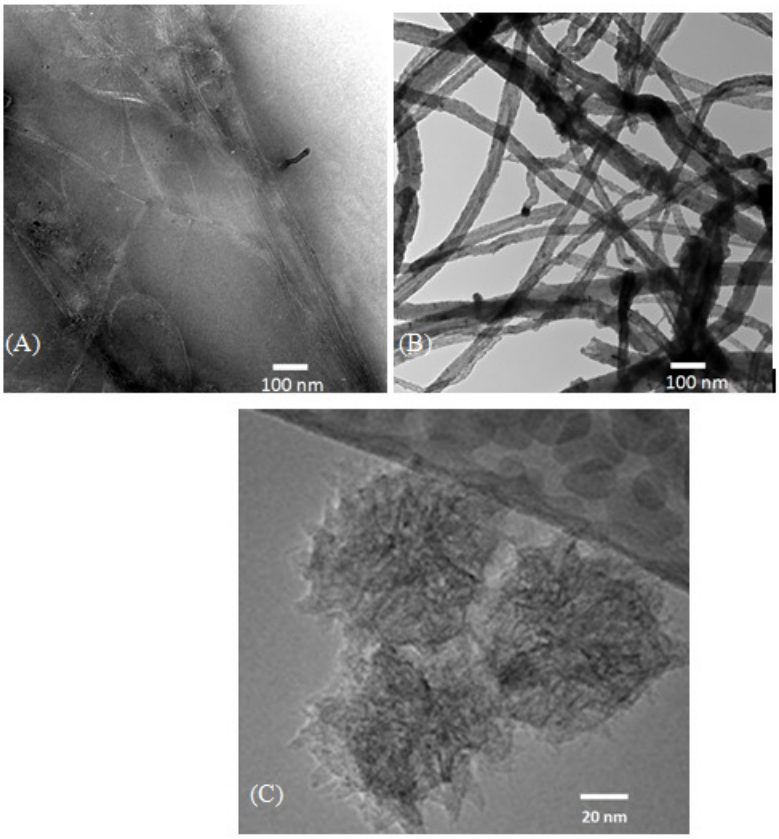

Figure 7. 1: TEM image of SWNTs (A), MWNTs (B), and SWNHs (C)

To our knowledge, this is the first experimental study measuring ROS generation by CNTs following laser excitation. In previous study, Fenogilo *et al.*[143] reported CNTs have ROS scavenging characteristics without laser excitation. They found MWNTs reduced ROS intensity in buffer solution.

7.3. Materials and methodology

Experimental sample consist of MWNTs, SWNTs, SWNHs, or peapods suspended (0.1 mg/ml) in 50 mM phosphate buffer solution, pH7, containing 1% (w/v) pluronic, and NADH (5 mM final). DMPO (100 mM final) was added directly to the CNTs (final concentration 0.08 mg/ml) and 50 µl of the final solution was added to wiretroll glass capillary tube (Fisher Scientific) and sealed at one end with critoseal clay. The samples were analyzed by EPR prior to

laser irradiation, then removed from the EPR instrument and irradiated with a continuous wave, ytterbium fiber laser, YLD-5-1064-LP (IPG Photonics) (1064 nm, 0.4 W/mm^2) for 25 seconds with the sample approximately 6 inches from the light source. Immediately after irradiation, each sample was returned to the EPR instrument to record the resulting spectrum. EPR spectra were obtained using Bruker ER200D EPR spectrometer equipped with at VT-4111 temperature control unit to maintain sample temperature at 25^{o}C. EPR spectra were obtained at 9.79 GHz microwave frequency and 6.3 mW microwave power using a magnet centerfield of 3485 G, 120 G sweep width, 100 kHz modulation frequency with a 1 G modulation amplitude, a 163 ms time constant, and a gain setting of 5x10^5. EPR spectra were digitized, stored, and analyzed on a laboratory computer using the program EWWIN written by Philip D. Morse (Scientific Software Services). Control experiments were carried out using samples omitting one experimental component each, including samples not irradiated, samples not containing CNTs, samples not containing NADH, and samples not containing DMPO. An additional control experiment utilizing superoxide dismutase (SOD, 100 units/ml) in the EPR sample was included to test whether superoxide was the trapped radical in the irradiated samples.

7.4. Results and Discussion

Our first experiment utilized SWNHs, which were suspended (0.08 mg/ml) in 50 mM phosphate buffer (pH 7.0) containing 100 mM DMPO and 5 mM NADH. The EPR spectra were recorded prior to irradiation with laser light (Figure 7.2A) and the spectrum suggested no evidence of a trapped radical. The sample was removed from the EPR and laser irradiated (5W, 1064 nm) for 25 seconds, after which the sample was returned to the EPR spectrometer and the spectrum was recorded (Figure 2B). After that the laser power was raised to 10 W and the EPR spectrum recorded for 25 sec laser irradiation (Figure 7.2C). It was found that 10W laser power gave higher intensity of EPR spectrum than 5 W powers. Both spectra showed the characteristic features for •OH trapped by DMPO (DMPO-OH), specifically, two overlapping triplets with hyperfine couplings of ~15 g [141]. The spectrum also appeared to contain a number of smaller peaks characteristic of trapped superoxide (DMPO-OOH), but these peaks were just above the detection limit for the spectrometer and were difficult to analyze (Figure 7.2 B). Control experiments were carried out using samples omitting one experimental component each

(including samples not irradiated, samples not containing CNTs, samples not containing NADH, and samples not containing DMPO).

It is well documented that superoxide trapped by DMPO is unstable and quickly rearranges to trapped hydroxyl [67,141]. Therefore, test whether laser irradiation produced exclusively •OH radical or $O_2^{\bullet-}$ which rearranged to the hydroxyl radical,•OH when trapped by DMPO, we repeated the experiment in the presence of superoxide dismutase (SOD), which converts $O_2^{\bullet-}$ to H_2O_2 by a diffusion limited reaction. H_2O_2 is not a radical species and does not react with spin traps. As shown in Figure 2G, the inclusion of SOD completely eliminated the trapped radical spectrum. Since SOD has no effect on the presence of •OH radical, this results suggests that the trapped radical was $O_2^{\bullet-}$ itself and that no •OH radical was produced directly.

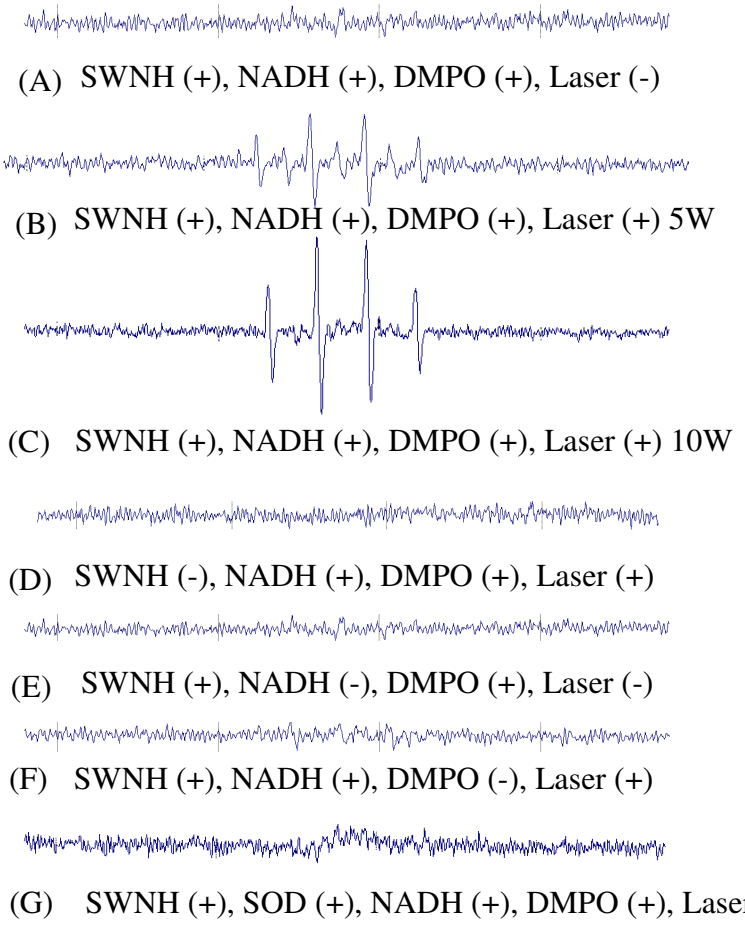

Figure 7.2: EPR spectra resulting from SWNHs in the presence of DMPO spin trap. (Spectrum A) SWNHs (0.1 mg/ml) suspended in 50 mM PBS, pH 7.0, containing 100 mM NADH and 100 mM DMPO. (Spectrum B) Same sample as in (A) after irradiation with 1064 nm laser light (0.4 W/mm^2) for 25 sec prior to spectrum acquisition SWNH (Spectrum D), NADH (Spectrum E) and DMPO spin trap (Spectrum E) were all required for the result obtained in Spectrum B.

(Spectrum G) Inclusion of SOD (100 units/ml) eliminated the trapped radical, indicating superoxide was generated by laser irradiation of SWNHs. Spectra represent 120 G sweep width

We have done the similar experiment for MWNTs, SWNTs, and peapods with same laser power (5W and 10W), and with same amount of NADH and DMPO. However the EPR spectra for MWNTs, SWNTs, and peapods were very weak, even after a longer period of laser irradiation (3 min). Figure 7.3 represented the EPR spectra for MWNTs without laser and with 5 W and 10 W laser power. Following 10 W laser irradiation, the spectrum indicated ROS generation. However the spectrum was too weak and complex to identify the nature of ROS (Figure 7.3 C).

(A) MWNTs (+), NADH (+), DMPO (+), Laser (-)

(B) MWNTs (+), NADH (+), DMPO (+), Laser (+) 5 W

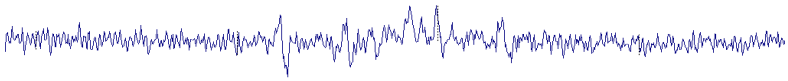

(C) MWNTs (+), NADH (+), DMPO (+), Laser (+) 10W

Figure 7. 3: EPR spectra of MWNTs in presence of NADH and DMPO without laser (A), after laser irradiation with laser power 5W (B), and 10W (C) for 2 min

The EPR spectra of SWNTs and their peapods with laser (5W and 10 W) also indicated a small amount of trapped ROS. For both cases a small amount of ROS generation was noticed with 10 W laser irradiation for 3 min (Figure 7.4-7.5). As above, these spectra were too weak to complex to identify the nature of trapped ROS. Qualitatively the EPR spectra of MWNTs, SWNTs, and peapods were different suggesting each type of CNTs generated different types of ROS.

(A) SWNTs (+), NADH (+), DMPO (+), Laser (-)

(B) SWNTs (+), NADH (+), DMPO (+), Laser (+) 5W

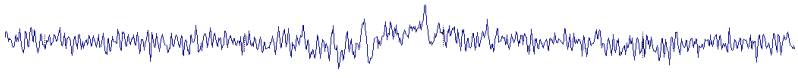

(C) SWNTs (+), NADH (+), DMPO (+), Laser (+) 10W

Figure 7.4: EPR spectra of SWNTs in presence of NADH and DMPO without laser (A), after laser irradiation with laser power 5W (B), and 10W (C)

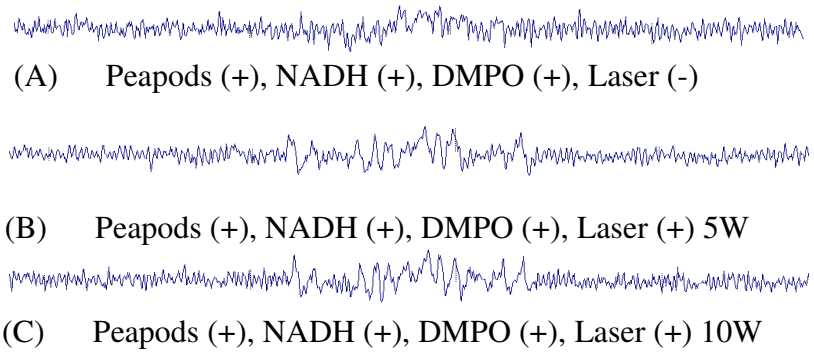

Figure 7. 5: EPR spectra of peapods in presence of NADH and DMPO without laser (A), after laser irradiation with laser power 5W (B), and 10W (C)

Compared to other CNTs, SWNHs generate significant amount of ROS during laser irradiation. This indicates SWNHs is better photochemical therapeutic agent than other types of CNTs discussed in this paper. Based on the results of Zhao et al., and Yamakoshi et al., our spin-trap results suggest that laser irradiation excitation of the SWNHs promotes the formation of superoxide using NADH as an electron source. Because laser irradiation was required to observe the trapped DMPO-OH adduct, we propose the laser-excited SWNHs acted as a photosensitizer that facilitated the formation of singlet oxygen (similar to C_{60} in equation 1), which then received an electron from NADH to form superoxide, which was subsequently trapped by DMPO resulting in the final DMPO-OH adduct (equation 2-4).

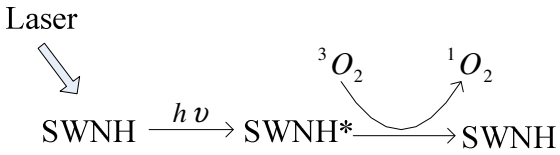

(7.2)

$$\mathrm{NADH} \xrightarrow{-e} {}^1O_2 \longrightarrow \mathrm{NAD^+} + O_2^{\bullet -} \qquad (7.3)$$

(7.4)

The experiment of SOD with SWNHs provided a clear evidence that initially $O_2^{\bullet-}$ was generated in the presence of NADH and after some period of time it was converted into •OH radical. Therefore, when $O_2^{\bullet-}$ was quenched down by SOD no evidence of •OH radical was observed.

7.5. Conclusion

Our results show that in the presence of an electron donor, SWNHs generate ROS during laser irradiation, consistent with the ability of SWNHs to potentially kill cancer cells. In contrast laser irradiation of MWNTs, SWNTs, and peapods generate only small amounts of ROS. Therefore, SWNHs are the best photochemical therapeutic agent, compared to other CNTs, which can be used as a combinatorial treatment tool to kill cancer cells by producing highly reactive free radicals for photochemical based treatment, in addition to their previously published capability to absorb significant amounts of laser light for photothermal therapy.

7.6. Acknowledgement

This research was funded by the following sources: National Science Foundation Grant CBET 0731108, National Institute of Health Grant 1 R21 CA135230-01, and an Institute for Critical Technology and Applied (ICTAS, Virginia Tech) Science Grant. We would also like to thank Dr. David Geohegan from Oak Ridge National Laboratories for his kind gift of the single walled carbon nanohorns.

Chapter 8: Distribution study

Time dependent Cellular Uptake and distribution study of carbon nanotubes (CNTs)

Saugata Sarkar[1], Kathy Lowe[2], Marissa Nichole Rylander[1]
[1]Department of Mechanical Engineering and School of Biomedical Engineering and Sciences
[2]College of Veterinary Medicine
Virginia Tech
Blacksburg, VA 24061

8.1. Abstract

The objective of this research is to measure the time dependent cellular uptake of CNTs in cells and distribution of CNTs in tissue representative phantoms, and mouse tumors. We have measured the cellular uptake and distribution of MWNTs in PC3 (prostate cancer carcinoma) cells, tissue representative phantoms, and mice tumors (RENCA: renal cancer carcinoma). The cellular uptake and distribution of MWNTs in PC3 cells, tissue representative phantoms, and mice tumors was analyzed with Transmission Electron Microscope (TEM). Cellular uptake *in vitro* was measured after incubating MWNTs (diameter 40 nm-60 nm, length 900 nm-1200 nm, concentration: 0.1 mg/ml in media) with PC3 cells for 2 hrs, 4 hrs, 6 hrs, 8 hrs, and 24 hrs. In order to measure the distribution of MWNTs in tissue representative tumor tissue, MWNTs with 0.1 mg/ml in pluronic water were uniformly dispersed in tissue representative sodium alginate phantoms. In order to measure the cellular uptake and distribution of MWNTs within an *in vivo* tumor model, MWNTs in PBS (0.1 mg/ml concentration) were injected in mice tumors (RENCA) *in vivo* and analyzed their cellular uptake and distribution was measured 2 hrs, 5 hrs, 24 hrs, and 48 hrs following injection. MWNT distribution in tissue representative phantoms was found to be quite uniform. The TEM images gave very clear evidence of internalization MWNTs

into tumor cells for both *in vitro* and *in vivo* studies. The TEM distribution study has provided a qualitative understanding of the nanoscale distribution of CNTs.

8.2. Introduction

In order to develop a computational model of CNT mediated laser cancer therapy, it is crucial to known the actual distribution of CNTs in tissue. Incorporating CNTs in tissue changes thermal and optical properties of tissue, which was discussed in chapter 4 and chapter 5. Variations in CNT distribution will also affect the temperature profile in the tissue following laser irradiation. Therefore, it is very important to know the actual distribution of CNTs in the tissue to create a realistic computational model of tumor, where tissue properties will depend on the CNT distribution in the actual tissue.

Among many CNTs, we selected MWNTs (length 900 nm-1200 nm, diameter 40 nm-60 nm) in our preliminary distribution study, because MWNTs are easy to image by TEM due to their larger diameter compared to SWNTs and SWNHs. They also possess metal impurities such as iron, which can provide very good image contrast agent for TEM and magnetic resonance (MR) imaging.

Previous literature has measured CNT distribution and their toxicity in cells [26,73-77]. Liu *et al.* described the distribution of SWNTs in various organs of mice functionalized with radioactive materials (tracer materials), where Raman signature gave a quantitative analysis of SWNTs in different organs for specific times [77]. Nancy *et al.* measured the interaction of MWNTs in human epidermal cells *in vitro* for various incubation periods using TEM imaging [74]. The TEM images showed the presence of MWNTs in cell vacuoles. However, they did not describe the presence of MWNTs in other parts of the cell such as the cell nucleus, membranes, cytoplasm, etc. Kam *et al.* described the presence of SWNTs in Hipco cells after labeling SWNTs with a fluorescent tag [26]. His confocal microscopic images showed several SWNTs were present around the cell nucleus. Cheng et al. measured the distribution and toxicity of unpure and pure MWNTs in human macrophage cells using TEM imaging. In this study, TEM imaging was utilized to measure the cellular uptake of MWNTs. MWNTs were observed in cell membrane and vacuole after 4 hrs and 4 days [73].

However, the time dependent quantity and distribution of CNTs in cells has not been thoroughly investigated. In this work, we have studied the time dependent distribution of

MWNTs in PC3 cells, tissue representative phantoms, and mice tumors using TEM. However, it is difficult to quantify MWNT distribution and image a large region of the sample to provide micro/macro level distribution of CNTs due to the high magnification and small field of view. Therefore, we have taken TEM images at various locations of tissue, cells, and phantoms in order to get an overall picture of the distribution of MWNTs.

8.3. Materials and methodology

8.3.1. Purity test of MWNTs

MWNTs were synthesized by Dr. David Carrol's group at Wake Forest University. The MWNTs were purified and cut into 900 nm length. In order to cut the MWNTs, Raw (15mg) MWNTs were mixed with 98% sulfate acid and nitric acid solution in 3:1 ratio and sonicated for 20 hrs. This resulted in MWNTs predominantly 900 nm. A 0.2 μm Teflon filter was used to filter and neutralize the acid solution by adding DI water and continuing to filter for one or two days. The filtered MWNTs were dried in an oven at 80 ^{0}C to 90 ^{0}C degree for 2-3 days.

Before using these MWNT samples for cellular uptake and distribution measurements, TEM images were captured to verify synthesis of MWNTs and their purity. In order to make For this measurement, MWNTs were dissolved in an organic solvent (ethanol) which has higher volatility and three concentrations (0.1 mg/ml, 0.05mg/ml, and 0.01mg/ml) were made. From each sample, a drop of ethanol was put on the top of the Copper grids with 200 meshes and dried with air. When the samples were ready they were put into the TEM (Philips EM420) and MWNTs were imaged. Of the different concentrations of MWNTs in ethanol, only 0.01 mg/ml were able to be imaged. Samples with a higher concentration formed a thick layer on the TEM grids, which prevented to imaging of MWNTs. During the experiment, 100KV was applied by the TEM to image non-biological samples. MWNTs were quite pure with the presence of traces of iron catalyst as shown by the dark spots (Figure.8.1 A-B). Diameters of MWNTs varied from 40-60 nm.

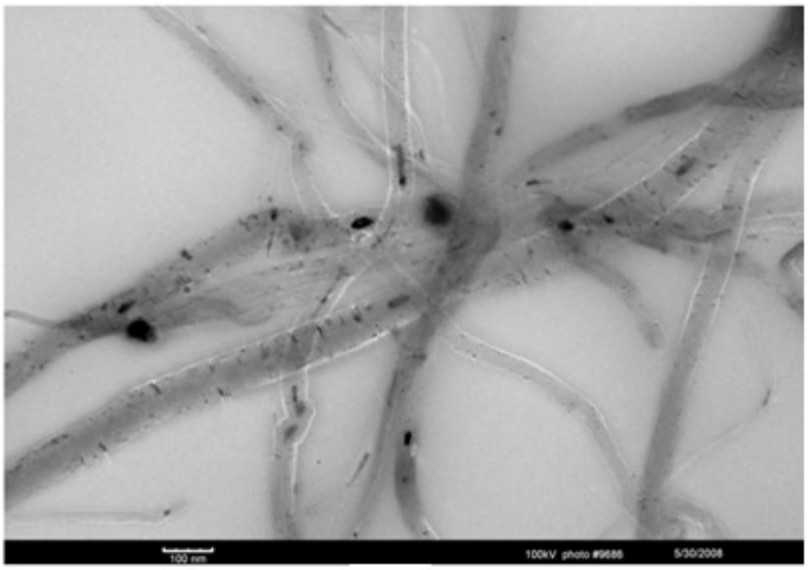

(A)

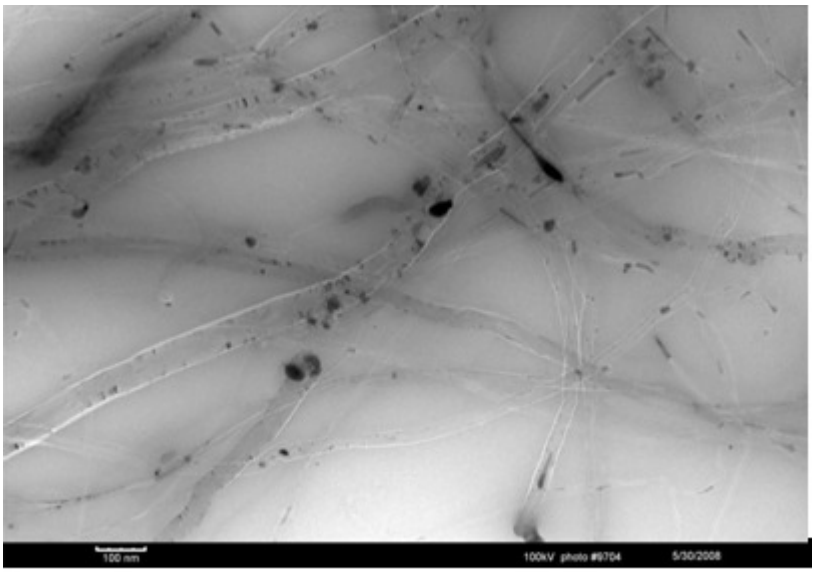

(B)

Figure 8.1: TEM images of two MWNT samples at magnifications of 100000 (A) and 75000 (B)

8.3.2. *In vitro* experiment

MWNTs are naturally hydrophobic and they are not soluble in a polar solvent like water. In order to make them water soluble, CNTs were made hydrophilic by functionalizing their outer surfaces by 1% w/v concentration of pluronic water, which forms a non-covalent hydrophilic

layer around the CNTs without changing any thermal, optical, and mechanical properties. CNTs were put into the pluronic-water solutions and sonicated for 20-30 minutes to make a desired concentration (0.1 mg/ml).

TEM imaging was utilized to investigate the intracellular uptake and distribution of MWNTs within the PC3 cells. MWNTs with concentration of 0.1 mg/ml in cell media were incubated with PC3 cell line for 2 hrs, 4 hrs, 6 hrs, 8 hrs, and 24 hrs. After a desired period of incubation a Karnovsky fixative (aldehyde) was introduced to fix the cells after which cells were resuspended in cell media. The fixed cells were vortexed for 5 min at 3000 rpm to form a soft pellet. Fixative was gently pulled off without disturbing the cell pellet. The pallet was washed 4/5 times with buffer solution to remove all fixative. A molten agar (58 ^{0}C) was added to cells and quickly resuspended after spinning for 5 min at 3000 rpm. The samples were refrigerated for 5 min to solidify. The solid samples were sectioned using microtome into about 100 nm slices for TEM imaging.

Figure 8.2-8.4 depicts TEM images of the intracellular distribution following 2 hrs, 6 hrs, 8 hrs, and 24 hrs incubation of MWNTs with cells. TEM images show clear evidence of internalization of MWNTs inside cells. TEM images of cell morphology are described in Figure.8.2 A-B, showing different sections of undamaged cells. The images were taken at 4000X magnification where MWNTs were not visible. A very clear evidence of internalization of MWNTs into cells is apparent in Figure. 8.3 A-B, where MWNTs were observed around cell vacuoles. After 2 hrs of incubation, a significant number of MWNTs were already observed within cells around the nuclear membrane (Figure. 8.4 A). With increasing incubation periods (4 hrs, 6 hrs, and 24 hrs), larger numbers of MWNTs were observed inside cellular vacuoles and nuclei (Figure. 8.4 B-D). A figure of MWNT distribution at 4 hrs is not shown here. Identical intracellular uptake trends were observed for *in vivo* analysis, described in the following section.

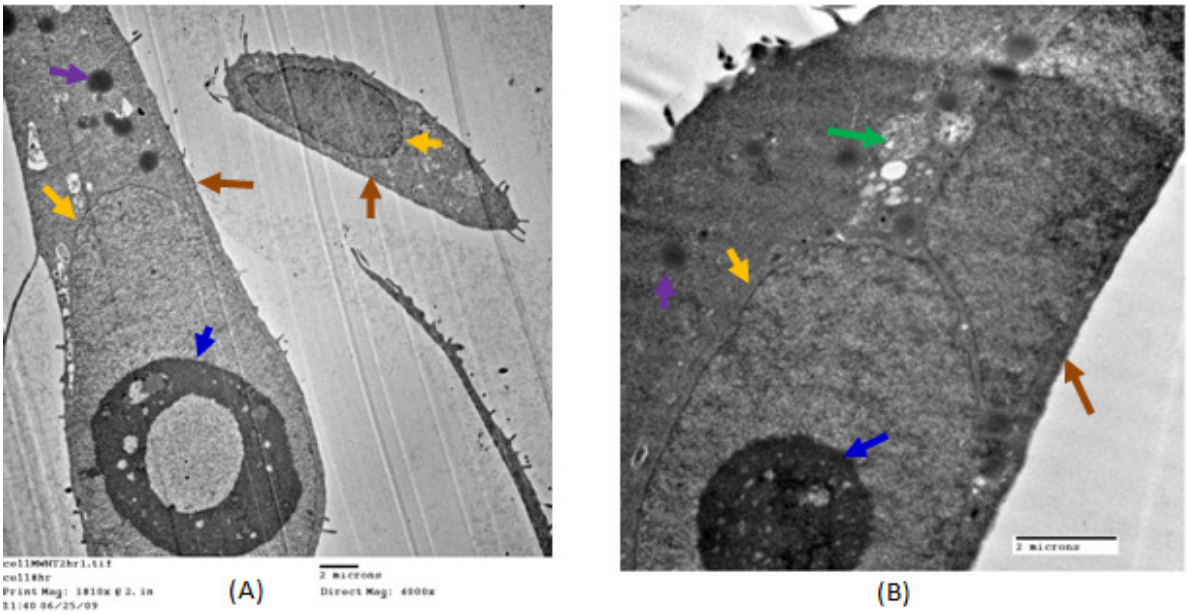

Figure 8.2: TEM images (A and B) of cells with MWNTs showing cell morphology with 4000X direct magnification, where brown arrows indicate cell membranes, yellow arrows indicate nuclear membranes, green arrows indicates vacuoles, blue arrows indicate nucleoli, and violet arrows indicate lysosomes

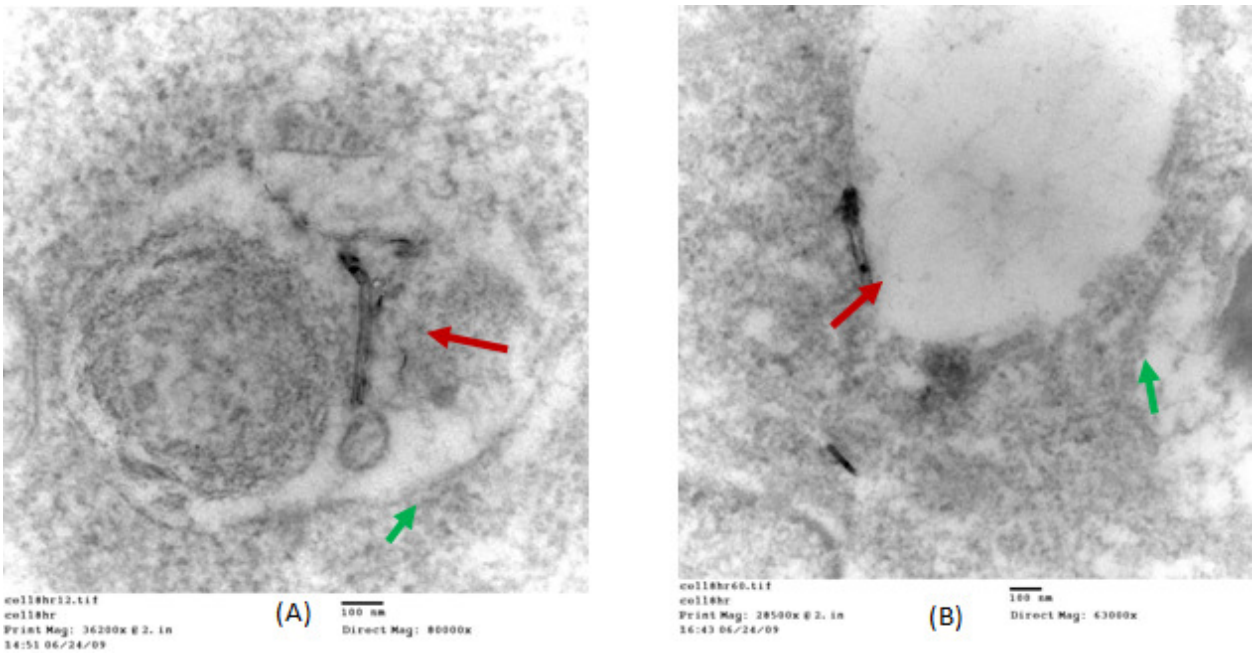

Figure 8.3: MWNTs (designated by red arrows) are inside cell vacuoles (denoted by green arrows). TEM image were captured at 63000X magnification

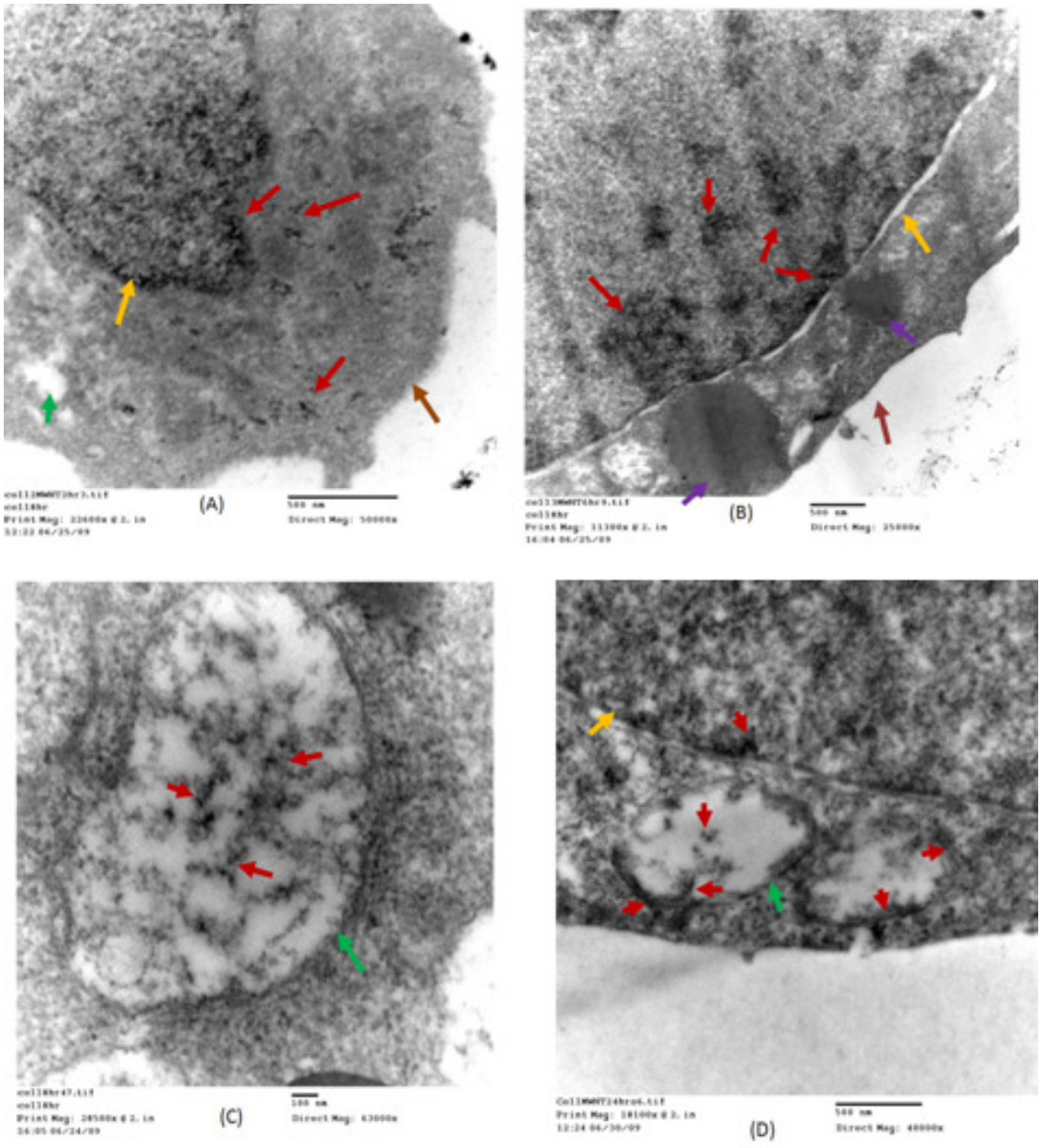

Figure 8.4: TEM images of PC3 cells following MWNT incubation periods of (A) 2 hr, (B) 6 hr, (C) 8 hr, and (D) 24 hrs. MWNTs were observed inside cell vacuoles (C-D), within nuclear membranes (A-D), and around nuclei (A,B, and D) where they are randomly distributed. Note the arrows indicating cell membrane (brown), nuclear membrane (yellow), vacuoles (green), and MWNT aggregates (red)

8.3.3. MWNT distribution in Phantom

In order to make a tissue representative phantom, sodium alginate Protanal LF 10/60 (FMC Biopolymer, Drammen, Norway) was mixed with MWNT solutions and a low viscosity

alginate with a mean guluronate / mannuronate (G/M) ratio of 70% and mean molecular weight of 180 kDa. Sodium alginate was stirred vigorously with MWNT-pluronic water to a 3% w/v concentration (3g / 100 ml) for 1 hour and the desired final concentrations of MWNTs in alginate solution were made. The final solution was cross linked with calcium chloride solution for 1 hr [108-109]. Tissue phantom samples were made with diameter of 20 mm and thickness of 2 mm.

MWNT-Phantom composites were cut into about 100 nm sections at varying depths with the a microtome to allow imaging with transmission electron microscopy (TEM). MWNT distribution within the phantoms was imaged for each section using a high resolution TEM (Zeiss 10CA made by Carl Zeiss, Inc.). The presence of MWNTs in the phantom can be distinctly identified as dark cylinders within the alginate matrix in (fig. 8.5 A-B). The distribution of MWNTs was predominantly observed to be evenly dispersed and randomly distributed throughout the phantom. Infrequent clusters or clumps of MWNTs with diameters on the order of several hundred nanometers were also noted. The diameter of individual MWNTs varied from 40-60 nm (fig. 8.6 A-B).

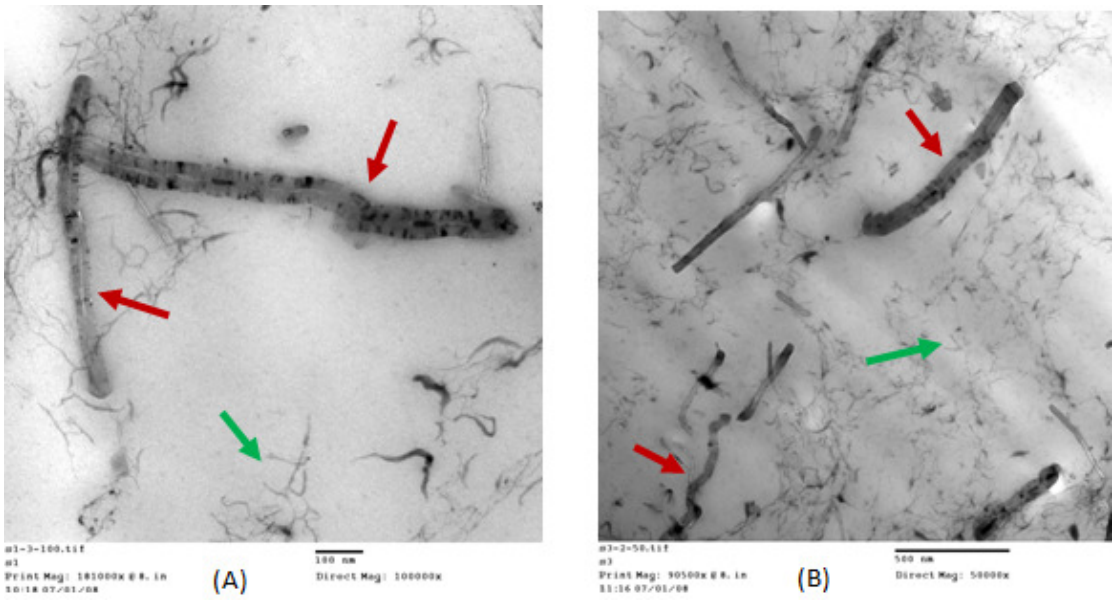

Figure 8.5: MWNTs in sodium alginate phantom (A and B). Red arrows indicate MWNTs and green arrows indicate sodium alginate fibers. Magnification of A and B were 100000X and 50000X respectively

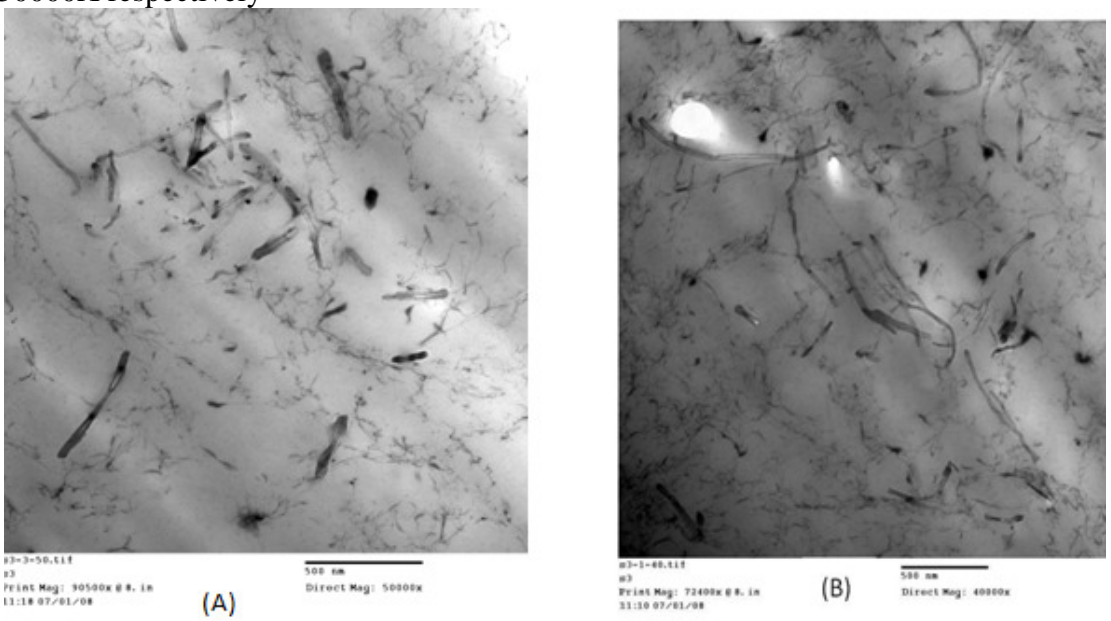

Figure 8.6: MWNTs are uniformly distributed in the phantom (A, and B). A and B are images at different depths with the phantom. The images were taken at 40000X magnifications

8.3.4. *In vivo* experiment

MWNTs (0.1mg/ml, length 900nm-1500nm, and diameter 20nm-90nm) were injected into PC3 tumors, grown on the back surface of four mice. Mice were sacrificed after 2hrs, 5hrs,

24 hrs and 48hrs following injection. The tumors were removed and processed with Karnovsky fixative. The tumors were sectioned into 30nm-50nm thin slices with a microtome. Three positions within the tumors; top, middle, and bottom were sectioned. The sections were picked up by copper grids with 200 meshes. Copper grids were stored in 100% ethanol before the sections were put onto the grids and dried in air on filter paper before use. At least five samples were made from each slice of the tumors. The grids were placed in a Petri dish and stained with 2% Uranyl acetate for 12 min to increase TEM image contrast. The samples were rinsed with DM-water and dried after staining. When the samples were ready they were put into the TEM sample holder and imaged to locate MWNTs. The voltage used for biological samples was 60 KV. Higher voltages may destroy biological samples. Two cells in the tissue showing their nuclei were shown in Figure.8.8 showing that cells are not damaged during sectioning. MWNT-imaged were found in cells after 2 hrs following injection (Figure. 8.8-8.11A). At this time, they were observed in the cell cytoplasm (Figure. 8.8 A-B), cell membrane (Figure. 8.9 A-B), nucleus (Figure. 8.10 A-B), and vacuole (Figure. 8.11 A-B). Some MWNTs were observed orthogonal to the cell membrane, which indicated MWNTs were trying to enter the cells (Figure 8.9 A-B). In this case some portion of MWNTs was inside the cell membrane. Figure 8.10 A-B provide clear evidence that MWNTs went inside the cell nucleus.

Similar images were found for 5 hrs, 12 hrs, 24 hrs, and 48 hrs following MWNT injection. Figure 8.10 B and Figure. 8. 11 B show MWNTs present in the nucleus and cell vacuole after 5 hrs and 24 hrs following injection of MWNTs. However, for longer period of time, more MWNTs accumulated in cell vacuoles as shown in Figure. 8.11 A-B, where few MWNTs were observed in cell vacuoles for 2 hrs (Figure. 8.11 A). Many MWNTs accumulated in vacuoles at 24 hrs (Figure. 12 B).

The distribution study and the cellular uptake of MWNTs will assist with creation of a computational model for CNT-Tissue composite which will be described in chapter 9.

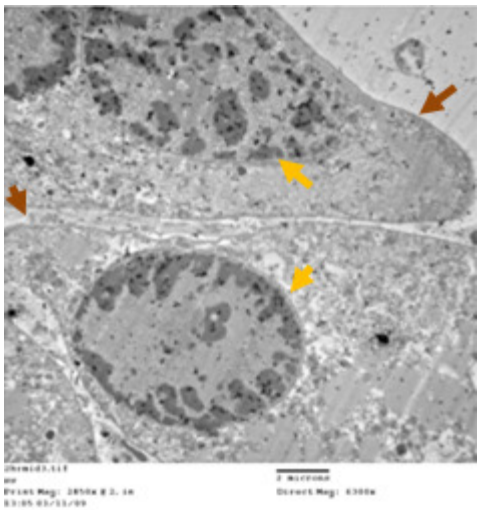

Figure 8.7: TEM image of a tissue section with direct magnification 6300X. In the figure cells have nucleus (yellow arrow) in the middle with encircled by cell membrane (brown arrow). No MWNTs were visible at this magnification. The section was taken from 2 hrs sample from the middle of the tumor

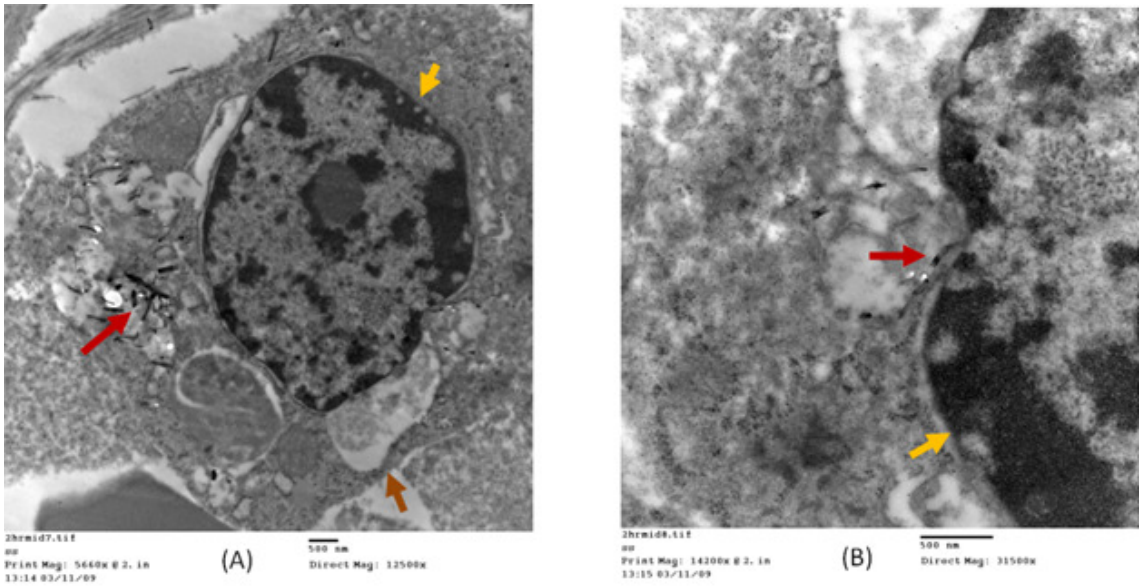

Figure 8.8: MWNTs are inside the cell membrane but outside the nucleus. Image was taken with direct magnification of 12500X (A) and 31500X (B)

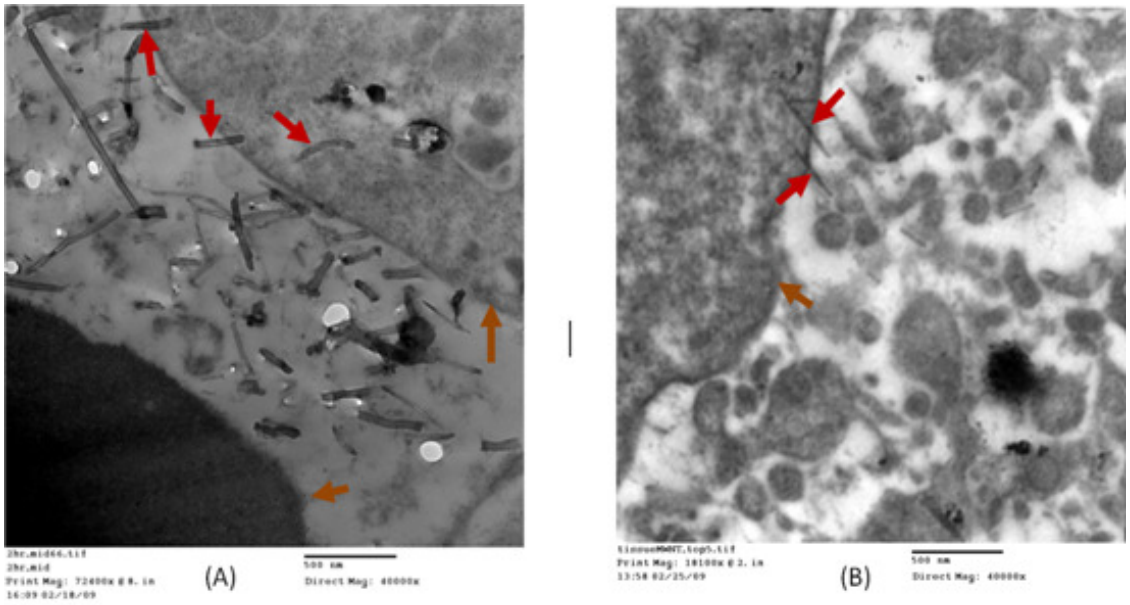

Figure 8.9: MWNTs are outside cells (A). Some MWNTs are perpendicular to the cell membrane (A and B) indicating that they are trying to enter the cell. Images were taken at 40000 magnifications

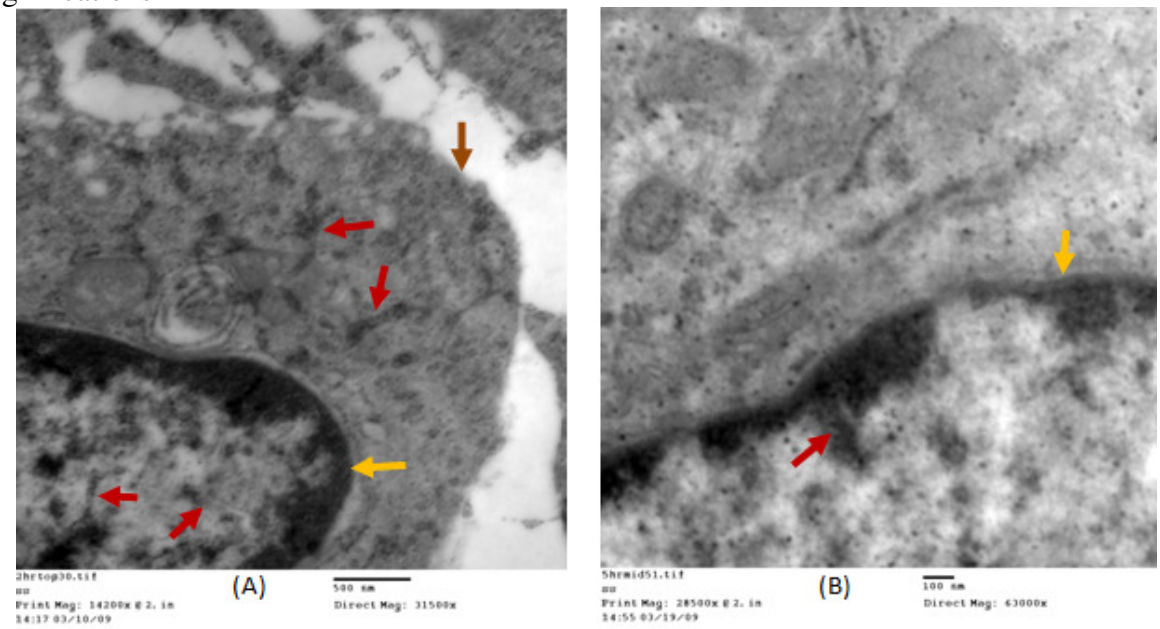

Figure 8.10: MWNTs are inside cell membrane (A), nucleus (A-B). Brown arrow and yellow arrow indicate cell membrane and nuclear membrane respectively

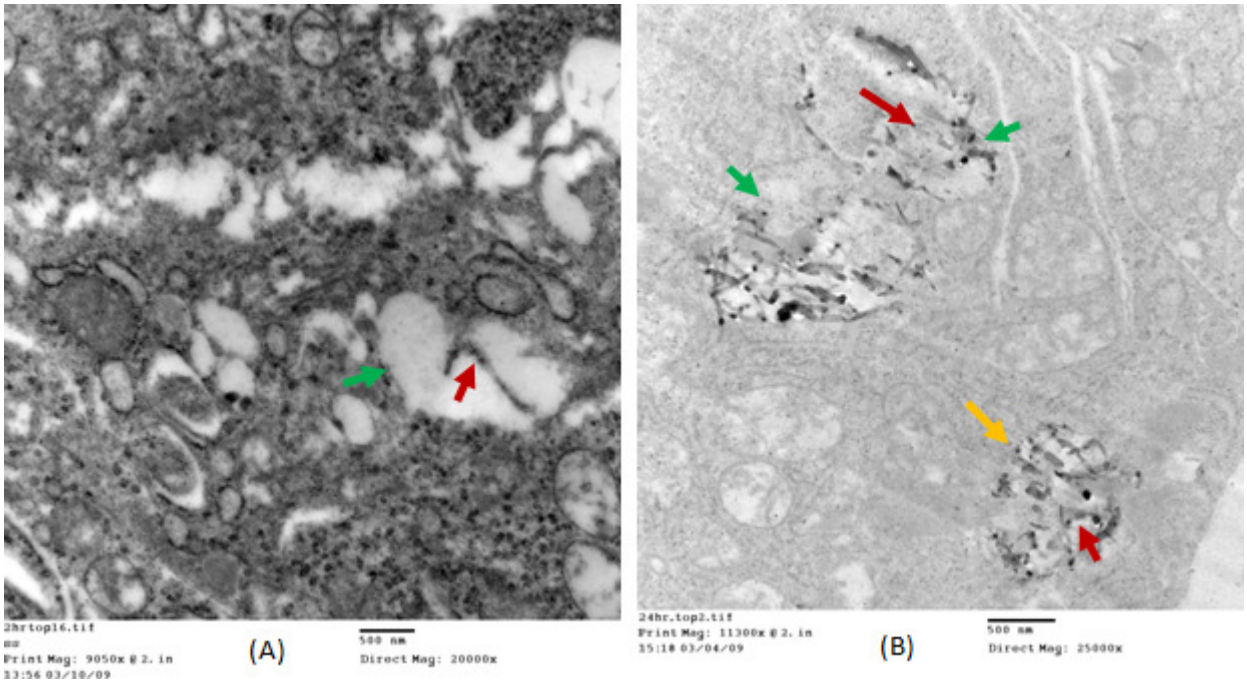

Figure 8.11: For 2 hr sample few MWNTs are found inside cell vacuoles (A), for longer period of times (24 hrs sample) many MWNTs are in cell vacuoles (B)

8.4. Conclusion

The time dependent cellular uptake and distribution of MWNTs *in vitro* (cells and phantoms), and *in vivo* (mouse tumors) gave clear evidence of internalization of MWNTs in cells for both *in vitro* and *in vivo* measurements. MWNTs were found randomly distributed everywhere in the phantom and in cells. From the TEM study, the distribution of MWNTs was predominantly observed to be evenly dispersed and randomly distributed throughout the phantom. MWNT distribution were found similar and uniformly distributed in both *in vitro* and *in vivo* study. Though in nano/micro scale, MWNT distribution sometime vary in cells (longer period of time has more MWNTs in vacuole than shorter periods), in macro scale the distribution can be considered as uniform.

However, it is difficult to conclude the macroscale nature of the distribution and quantify CNT concentration *in vitro* and *in vivo* by only TEM. To overcome these difficulties the following future studies need to be conducted.

8.5. Future study

The preliminary study with TEM provided a clear picture of internalization of MWNTs in cells, tissue representative phantoms, and mice tumors. Similar TEM study will be conducted

for other CNTs (SWNTs and SWNHs) in cells, phantom, and mice tumors. However, TEM images only provide qualitative information about cellular uptake and distribution of CNTs at the nano/micro scale and it is difficult to quantify transient CNTs concentration at different times. In order to quantify cellular uptake and provide a greater understanding of the CNT distribution in cells, phantoms, and tumors, the following studies need to be performed:

8.5.1. Raman spectroscopy study

The distribution of varying types of CNTs (MWNTs, SWNTs, and SWNHs) in cells, phantom, and tumors will be measured with Raman spectroscopy. This method will quantify the time dependent CNT concentration in cells, phantom, and tumors.

A Raman spectrometer can detect the presence of any materials in a sample describing their chemical composition by measuring particle size and concentration. In this spectroscopy measurement a sample is excited by a certain wavelength of laser light corresponding to the chemical composition of the sample. CNTs can be excited at wavelength of 785 nm and 532 nm [114]. The laser irradiation in a uniform area induces intense Raman scattering and gives a strong G band spectrum or Raman shift. The G band describes the nature of particles in the sample. The G band can determine the diameter and concentration of particles present in the samples.

A calibration curve will be generated with known concentrations of varying types of CNTs in water. In order to generate this calibration curve, CNTs in water with known concentrations will be placed in capillary tubes (volume 2 μL) and the Raman spectra will be measured for the each concentrations. At least four samples will be made for each concentration and the Raman counts will be averaged for each concentration. A calibration curve will be generated for each type of CNT after plotting Raman counts with respect to CNT concentration. Cell samples or tissue samples with unknown concentrations of varying types of CNTs will be placed into the Raman spectrometer to measure the Raman count for that sample. After comparing with the calibration curve the actual concentration will be measured. Raman intensities for CNTs in water, buffer solution, cell media, cells, and tissue are same [77]. Therefore, we can compare the Raman intensities of CNTs in cells or in tissue with the calibration curve of CNTs in water.

8.5.1. Distribution study with confocal microscopy

Confocal image study will be another important study in order to visualize the time dependent CNT distributions in cells, phantom, and mice tumors. This study will be conducted for varying types of CNTs (MWNTs, SWNTs, and SWNHs) functionalized with fluorescent particles like quantum dots (QDs).

QDs are used as fluorescent particle because they emit light in the wavelength range of 580 nm-630 nm depending on the size of QDs. CNTs will be surface functionalized with QDs to permit imaging of CNTs. In order to functionalize CNTs with QDs, CNTs and succinic peroxide are processed with high speed vacuum method (HSVM). During this method succinic peroxide breaks into several segments and attached to the surface of CNTs with an open carboxyl group (-COOH). QDs ,which have amine group (-NH_2) attached on the surface, will be processed with 1-ethyl-3-(3 dimethylaminopropyl) carbodiimide hydrochloride (EDC). EDC can conjugate -COOH groups (attached to CNTs) and –NH_2 (attached to QDs) to create a QDs attached to CNTs. After fuctionalization, TEM images will be taken for CNT-QD sample to study the quality of the functionalized CNT-QD (to study how many QDs are attached on the surface of CNTs).

For all samples of CNT-QDs in cells, phantom, and tumors, a Raman spectroscopy study need to be conducted simultaneously to compare the quantitative study of Raman spectroscopy with that of confocal microscopy.

Chapter 9: Computational model

The following article will be submitted in the **Journal of Biomedical Optics** and the article was written based on the format of above mentioned journal.

Computational Model for Carbon Nanotube-mediated Laser Cancer Therapy

Saugata Sarkar[1], Xuanfeng Ding[2], Heather C. Hatcher[2], Andrew Burke[2], Christopher G. Rylander[1,2], Suzy Torti[2], Marissa Nichole Rylander[1,2]

[1]Department of Mechanical Engineering
Virginia Tech, Blacksburg, VA 24061.

[2]School of Biomedical Engineering and Sciences
Virginia Tech-Wake Forest, Blacksburg, VA 24061.

Email: mnr@vt.edu.

Keywords: Cancer therapy, Carbon nanotubes, oncology, tissue phantom, kidney tumor, hyperthermia.

9.1. Abstract

Development of effective cancer therapies utilizing nanoparticles and laser based treatment require an understanding of the resulting temperature distribution and tumor response. We developed a computational model to predict the temperature response of tissue representative phantoms and RENCA kidney tumors to inclusion of multi-walled carbon nanotubes (MWNTs) and external irradiation with a continuous wave laser. Optical and thermal properties of tissue phantoms with MWNT inclusion served as inputs to the Penne's bioheat equation from which temperature was determined with finite element methods. The accuracy of the computational model was verified by comparing experimentally measured and model predicted temperature for tissue phantoms and RENCA kidney tumors with and without MWNT inclusion (concentration 0.1 mg/ml, length~900 nm, diameter 40-60 nm) which were externally laser irradiated by a continuous beam Nd-YAG laser with wavelength 1064 nm and irradiance of 3-4.5 W/cm^2, and heating time of 30 and 90 sec. Inclusion of MWNTs in the phantoms and mice tumors dramatically raised the temperature to ~59 ^{0}C and ~77 ^{0}C respectively for 90 sec and 30 sec laser heating. However, without MWNT inclusion of phantoms and tumors the temperature was

determined to be ~52 ^{0}C and ~61 ^{0}C for the same heating duration. The comparison between model predicted and experimentally measured temperatures of phantoms are 59 ^{0}C and 52 ^{0}C in the pocket area and 50 ^{0}C and 41 ^{0}C outside the pocket (2 mm away) respectively. For tumors with MWNTs, model predicted and experimentally measured temperatures are 77 ^{0}C and 76 ^{0}C, and without MWNTs they are 61 ^{0}C and 47 ^{0}C respectively. The discrepancy between our model-predicted temperature and experimentally measured temperature most likely can be attributed to variation between the position at which the model and the experiment determined temperature. The computational model determined the temperature at the center of the laser beam however, the position of experimental measurement of temperature is uncertain. Both experimental and modeling techniques will be refined to account for this difference.

9.2. Introduction

Laser therapy can provide a minimally invasive treatment alternative to surgical resection of tumors. However, the effectiveness of a laser cancer therapy is limited due to nonspecific heating of target tissue and diffusion limited thermal deposition which often leads to healthy tissue injury and extended treatment durations. These therapies can be further compromised due to induction of molecular chaperones called heat shock proteins (HSPs) in tumor regions where non-lethal temperature elevation occurs. HSP upregulation in cancer cells can lead to enhanced tumor cell viability and tumor recurrence [2-4] and provide resistance to subsequent chemotherapy and radiation treatments which are typically used in combination with the initial hyperthermia treatment [2,4-7,13-14,88]. Therefore, more effective laser therapy may be achieved through enhanced thermal deposition, improved heating selectivity, reduced treatment times and thermal dose, confined tumor injury, and elimination of HSP expression by elevating temperature in the tumor.

Multi-walled carbon nanotubes (MWNTs) have received enormous attention recently for their potential role as heat delivery vehicles for laser ablation of tumors [22-24,31,33,96-97]. MWNTs possess two or more concentric tubes with diameters of 5.0-100 nm and lengths of 1-50 microns [28-32]. MWNTs possess significant ability to absorb electromagnetic signals in the near infrared region (NIR) (700-1100 nm) due to their antenna properties and subsequently generate heat [35,37]. Incorporating MWNTs into the tumor can enhance laser therapy effectiveness potentially by 1) increasing light absorption by tissue since MWNTs increase the

absorption coefficient of tissue [144] and 2) increasing thermal diffusion by increasing the overall thermal conductivity of tissue through inclusion of highly conductive MWNTs [145].

Despite the promise of MWNT-mediated laser therapies, treatment planning models are necessary to determine optimal MWNT properties and laser parameters to effectively cause targeted tumor destruction. Computational models have been developed by others to predict tissue response to laser irradiation [82-84,146-147]. Rylander *et al* has previously developed treatment planning models for prostate cancer laser therapy capable of predicting and optimizing temperature, thermal injury, and HSP expression based on measured data [85,87-89,148-149]. However, existing models of photothermal heating of tissue embedded with nanoparticles is limited.

This paper describes the first stage development of a new treatment planning model for predicting the temperature response to inclusion of MWNTs in laser therapy and experimental validation of this model using tissue representative phantoms and kidney tumors. Measured distributions of MWNTs in tumors and phantoms provided the basis for defining the finite element system geometry of the phantom and tumor containing MWNTs for our computational model. Measured optical and thermal properties of tissue phantoms containing MWNTs served as critical inputs to the model. The temperature prediction by the model was compared to experimentally measured temperature in tissue phantoms and tumors containing MWNTs which were laser irradiated.

9.3. Materials and methodology

9.3.1. Experimental System and Computational Model Geometry

Two types of experimental systems were utilized to develop and experimentally validate the computational models: tissue phantoms and *in vivo* RENCA tumors. Both systems will be described initially to inform the reader of the basis for model creation.

9.3.1.1. Tissue Phantoms

The first experimental system consisted of a sodium alginate phantom (diameter 20 mm, thickness 20 mm) incorporated with a pocket (diameter 5 mm, thickness 20 mm) containing MWNTs (0.1 mg/ml) located 4 mm below the outer surface of the phantom (Figure 1). The

pocket allowed confinement of the MWNTs to a specific region. To create the tissue phantoms, sodium alginate Protanal LF 10/60 (FMC Biopolymer, Drammen, Norway) was stirred vigorously with deionized water to a 3% w/v concentration (3g / 100 ml) for 45 min. The alginate was sterile filtered through a 0.45 μm membrane. In another solution of sodium alginate, MWNTs were mixed uniformly to yield a concentration of 0.1 mg/ml which was cross-linked using 80 mM calcium chloride for 1 h. This allowed creation of a solid phantom-MWNT composite with 5 mm diameter and 20 mm thickness, which we will refer to as the MWNT pocket. The pocket containing a high concentration of MWNTs was then placed into liquid sodium alginate solution (without MWNTs) and cross-linked for several hours in 80 mM calcium chloride. This resulted in a solid phantom of 20 mm diameter and 20 mm thickness with a MWNT pocket embedded within (Figure 9.1).

MWNTs for tissue phantoms and tumors (described subsequently) were synthesized and purified (> 95%) by Wake Forest university (Dr. David Carroll's lab). The purity of MWNTs was confirmed by transmission electron microscopy (TEM) and thermogravimetric analysis (TGA).Tissue phantoms can be synthesized to possess optical properties identical to real tissue according to our previous work utilizing sodium alginate, microspheres, and talc powder [144], Phantoms were used as a representative tissue model since they have similar thermal and optical properties to human tissue [22,123]. Tissue phantoms were used to provide a representative three dimensional tissue volume for initial measurement of temperature associated with MWNT inclusion and laser irradiation, measurement of MWNT distribution, and computational model validation. Although utilizing tissue phantoms does not account for the complex transport properties intrinsic to real tissue it provides an initial estimate of MWNT transport in tissue to assist with model development. Tissue phantoms will be externally irradiated as described in the model validation section subsequently.

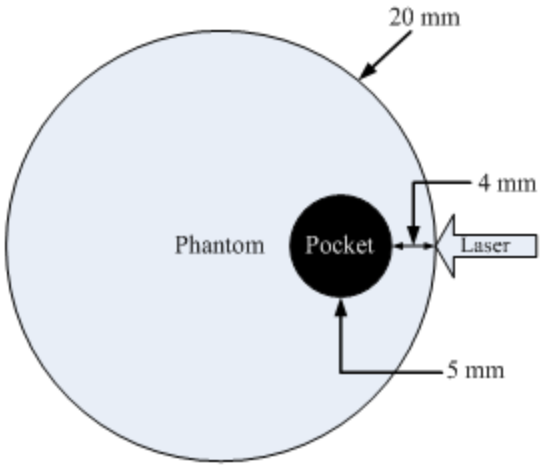

Figure 9.1: Schematic diagram of phantom

9.3.1.2. Tissue phantom computational model

A representative phantom geometry was generated by Hypermesh® assuming MWNT distribution in the pocket area was homogeneous (Figure 9.2). A symmetric cross section of the phantom (both sides of the phantom with laser in the middle) in the radial direction was the geometry considered. The phantom possessed a diameter of 20 mm and thickness of 2 mm. Due to symmetry on the top and bottom of the phantom an adiabatic boundary condition (Neumann, heat flux=0) was applied. On the edge a mixed boundary condition was applied which was represented as $K \cdot \partial T / \partial n = h(T_s - T_\infty)$, where K is thermal conductivity of phantom, T_s is the surface temperature, and T_∞ is the ambient temperature. The phantom was externally laser was irradiated near the pocket area as shown in Figure 9.2.

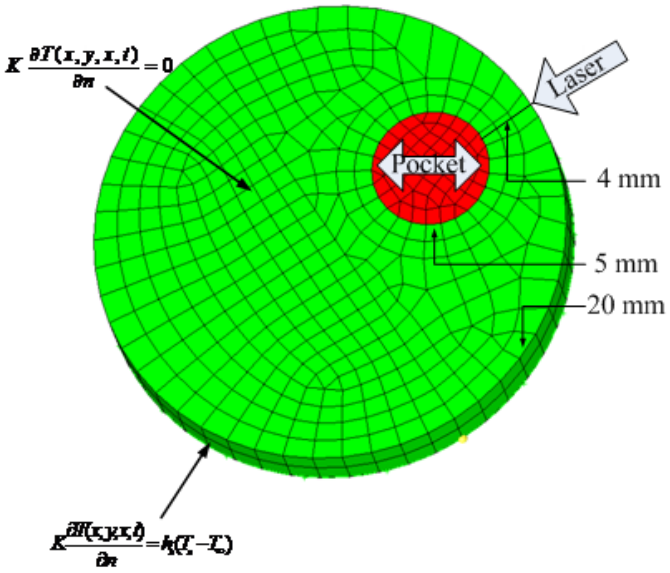

Figure 9.2: System geometry of phantom model

The geometry was imported into the ProPHLEX® (Altair Engineering) platform, which is an *h-p* adaptive, finite element package. This software allows determination of the temperature distribution during laser heating and study of the sensitivity of the thermal behavior to manipulation of individual source parameters. ProPHLEX® also permits specification of equations and boundary conditions, definition of the system including irregular geometrical domains, optimization of the finite element mesh, running of the simulation, and visualization of the temperature distribution. This software was previously utilized by Rylander *et al.* to simulate temperature distribution in prostate tumors following laser irradiation [87-88].

9.3.1.3. Tumor experimental model

The second experimental system consisted of a RENCA kidney tumor implanted subcutaneously on the back surface of a female athymic mouse. To create the tumors, RENCA tumor fragments measuring 2 mm^3 were transplanted into the flanks of mice. After 7 days tumor size was grown to 20 mm diameter and 50 µl of MWNT solution was injected at 4/5 points into tumors (total 100 µg of MWNTs) in order to create a uniform MWNT distribution (Figure 9.3). To allow experimental validation of the model, the tumor will be externally laser irradiated (irradiance 3 W/cm^2 and beam diameter 10 mm) for 30 seconds) at 20 hours after injection of MWNTs as described subsequently.

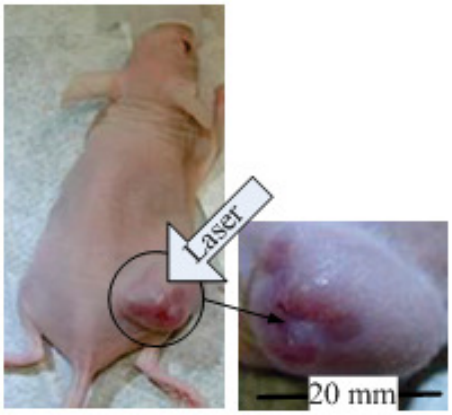

Figure 9.3: RENCA tumor with MWNTs

9.3.1.4. Tumor computational model

Based on the experimental tumor system, a representative tumor system geometry was created with Hypermesh®. In this model MWNT distribution was considered homogeneous throughout the tumor. Based on the symmetry of the system and desire for computational efficiency, a quarter sphere geometry was created to represent the tumor system. A mixed boundary condition was applied to the tumor surface representing the convective condition due to air exposure. Due to symmetry, an adiabatic boundary (Neumann) condition was applied to the vertical surface and a fixed temperature (37 ^{0}C, blood temperature) boundary condition was applied to the bottom of the tumor. A continuous wave laser (irradiance 3 W/ cm^2 and beam diameter 10 mm) will externally irradiate the tumor as represented in Figure 9.4 for experimental validation as described subsequently.

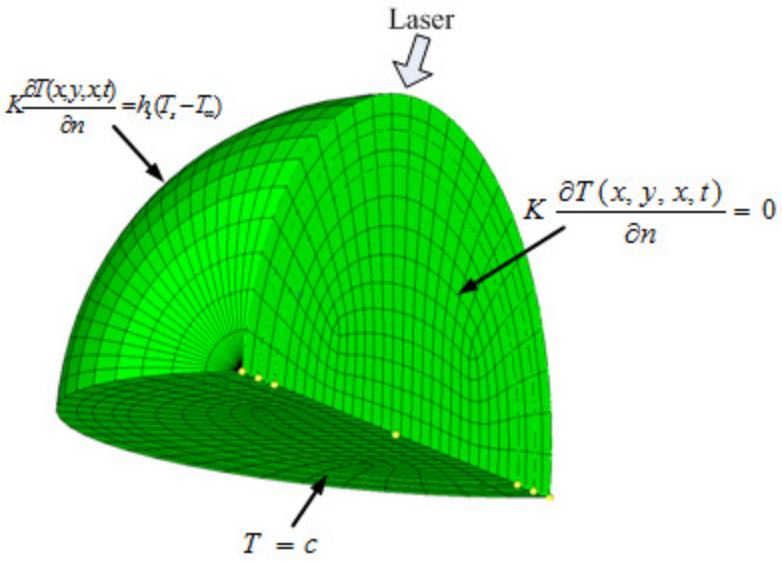

Figure 9.4: System geometry of tumor model

9.3.2. Penne's bio-heat equation

The temperature distribution of tissue was modeled with the Pennes' Bioheat equation (Equation 9.1) which incorporates expressions for the thermal effects of local blood perfusion and laser energy absorption [48].

$$\rho_t c_t \frac{\partial T}{\partial t} = \nabla \cdot [k(T)\nabla T] - \omega_b(T) c_b (T - T_a) + Q(\vec{r}, t) \tag{9.1}$$

where ρ_t , c_t , T_a, and c_b are the density and specific heat of the tissue, arterial blood temperature, and specific heat of the blood, respectively. The temperature dependent blood perfusion rate within the tumor is denoted as ω_b and is represented in Equation 9.2 [80].

$$\omega_b = \begin{Bmatrix} 0.833 & T < 37 \\ 0.833 - (T-37)^{4.8}/5.438\times10^3 & 37 \le T \le 42 \\ 0.416 & T > 42 \end{Bmatrix}, \text{kg/s.m}^3 \tag{9.2}$$

Due to the absence of blood perfusion in the phantom, ω_b was neglected. The optical and thermal input parameters to the Pennes' model to compute temperature distribution in the phantom and tumor model are tabulated in Table 9.1. The thermal conductivity values were previously measured by our group for phantoms with and without MWNTs using a hot wire probe method

[145]. The optical properties were determined using spectraphotometer measurements and the inverse adding doubling method for phantoms with and without MWNTs as previously described [144]. All properties were measured for the MWNT concentration of 0.1 mg/ml.

Table 9.1: Input parameters of computational model (MWNT-Phantom composites 0.1 mg/ml)

Parameters	Symbol	Phantom/Tumor only	Phantom/Tumor with MWNTs
Thermal conductivity	K	0.5737 $W/m \cdot K$	0.9495 W/m·K
Absorption coefficient	μ_a	0.0138 mm^{-1}	0.423 mm^{-1}
Scattering coefficient	μ_s	1.1382 mm^{-1}	1.985 mm^{-1}
Anisotropy coefficient	g	0.9877	0.926
Density of tissue	ρ_t	1045 kg/m^3	1045 kg/m^3
Density of blood	ρ_b	1058 kg/m^3	1058 kg/m^3
Specific heat of tissue	c_t	3600 $J/kg \cdot K$	3600 $J/kg \cdot K$
Arterial blood temperature	T_a	310 ^0K	310 ^0K

Heat source, Q associated with laser heating is expressed in Equation 9.3 [12,17,150].

$$Q = \mu_a \Phi(\vec{r}, t) \tag{9.3}$$

where, μ_a is the absorption coefficient of the phantom/tumor and $\Phi(\vec{r}, t)$ is the fluence rate, determined by Monte Carlo approach [17,60]. In order to solve Equation 9.1 a weak form of finite element model (FEA) was computed using the FEA software ProPHLEX®, which allows determination of the temperature.

9.4. Experimental results

9.4.1. Distribution study of MWNTs

The distribution of MWNTs within the tissue has a dramatic impact on the photothermal heat generation and diffusion. In order to accurately model the distribution of MWNTs, we experimentally verified the MWNT distribution in tissue representative phantoms and tumors with transmission electron microscopy (TEM).

9.4.1.1. Tissue Phantoms

We measured the distribution of MWNTs in the pocket and surrounding alginate with TEM to confirm our assumption of uniform MWNT distribution. Phantoms were sectioned into 500-600 nm thick slices by a microtome. The slices were placed on copper coated TEM grids with 200 meshes for TEM imaging. TEM images of the MWNT distribution within the MWNT pocket area and surrounding periphery are shown in Figure 9.5 A-B. TEM images were taken from the top, middle, and the bottom portion of the pocket area with five images acquired from each region. TEM images showed MWNTs to be evenly dispersed and randomly distributed with minor clustering. There was very little variability for different sections from the pocket with a representative image shown in Figure 9.5A. TEM images of the region outside the pocket indicated that here were no MWNTs in that region (Figure 9.5B).

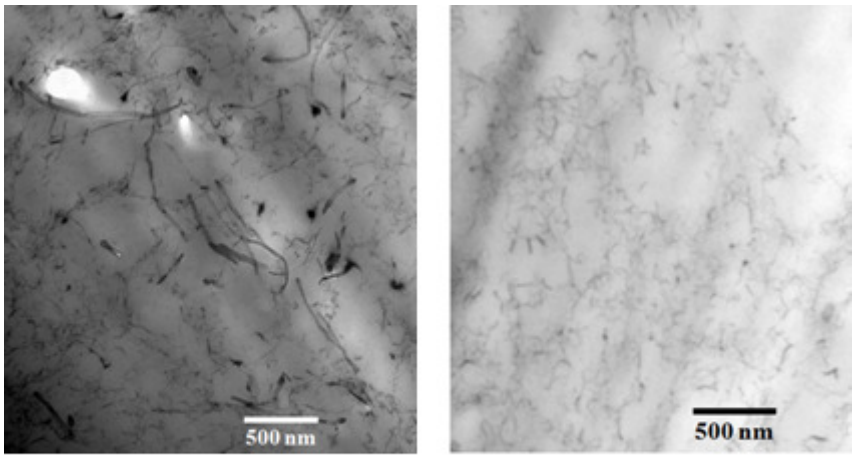

Figure 9. 5: TEM image of phantom in the pocket area (A). TEM image of phantom outside of the pocket area (B)

9.4.1.2. *in vivo* tumors

To confirm the MWNT distribution *in vivo*, TEM images were taken of the tumor for a range of post-injection times (2-48 hrs). MWNTs (0.1mg/ml, length 900nm-1500nm, and diameter 40nm-60nm) were injected into RENCA tumors grown on the back surface of four mice. Mice were sacrificed after 2, 5, 24, and 48 hrs following MWNT injection. The tumors were removed and processed with Karnovsky fixative. The tumors were sectioned into 30-50

nm thin slices with a microtome. Three positions within the tumors; top, middle, and bottom were sectioned. The sections were picked up by copper grids with 200 meshes. Copper grids were stored in 100% ethanol before the sections were put onto the grids and dried in air on filter paper before use. At least five samples were made from each slice of the tumors. The grids were placed in a Petri dish and stained with 2% Uranyl acetate for 12 min to increase TEM image contrast. The samples were rinsed with DM-water and dried after staining. When the samples were ready they were put into the TEM sample holder and imaged to locate MWNTs. The voltage used for biological samples was 60 KV to prevent damage to the samples.

Figure 9.6A shows two cells within the tumor tissue with intact nuclei in indicating cells are not damaged during tissue sectioning. In order to gain more of a microscale perspective of the MWNT distribution, a TEM image of the tissue was captured at 4000X. However, due to the low magnification of this image MWNTs are not visible in the cells. However, uniform distributions of MWNTs were observed in the cytoplasm, nucleus, and cell vacuole (figure 9.6 B) for all samples and times. The red, brown, and yellow arrows indicate MWNTs, cell membrane, and nuclear membrane respectively. Numerous MWNTs were also observed outside the cells between cell membranes (Figure 9.6 C). In figure 9.6 C-D, some MWNTs were observed penetrating the cell membrane. Similar MWNT distributions were observed in the top, middle, and bottom sections of the tumors for time point of 2-48 hrs. As a conclusion from Figure 9.6A-D, it can be described MWNTs are uniformly distributed in the tumor tissue.

Based on the TEM study, we found that the distribution of MWNTs in both phantoms and tumors were fairly uniform from a macroscale perspective. Therefore our assumption of uniform MWNT distribution in the phantom pocket and throughout the tumor in the computational model was acceptable.

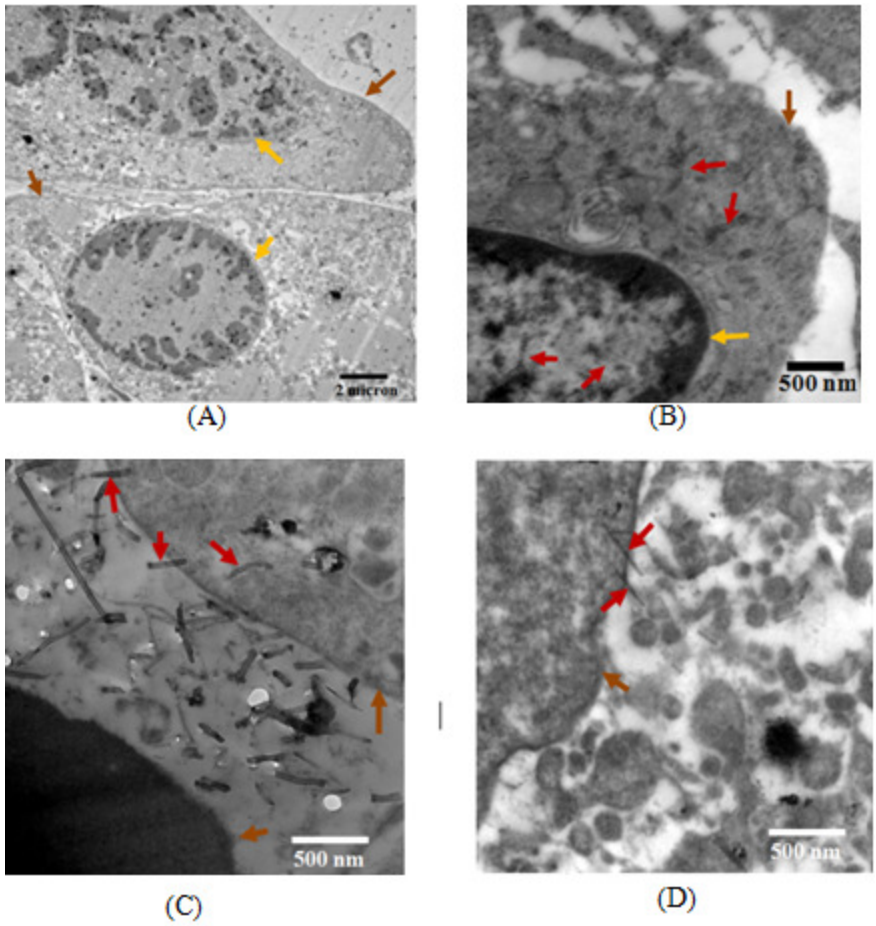

Figure 9. 6: TEM images of tumor cells with MWNTs with magnification of 4000x. (A). MWNTs are inside cell cytoplasm and nucleus at 31500x magnification (B). MWNTs are outside cells (C). MWNTs are trying to go inside cells (C-D) at 40000x magnification

9.5. Computational results

9.5.1 Phantom model prediction

Temperature was predicted for tissue phantoms alone and containing MWNTs following external laser irradiation by a continuous wave, ytterbium fiber laser, YLD-5-1064-LP (IPG Photonics) (wavelength 1064 nm, beam diameter 10 mm) with an irradiance 4.6 W/cm^2 for 90 sec. The input parameters, used to solve the computational model were listed in Table 9.1. The fluence distribution was calculated using Monte Carlo simulation. The irradiance was 2.55 W/cm^2 at 4 mm below the surface of phantom. The laser power loss was 40% at that position.

The temperature distribution for the phantom without MWNTs is shown in Figure 9.7A. The temperature elevation measured near the laser probe was 52^0C after 90 sec of heating. The laser has a Gaussian distribution with maximum laser intensity in the middle of the beam.

Inclusion of MWNTs dramatically enhanced the thermal deposition (Figure 9.7B) due to higher absorption coefficient of Phantom-MWNT composite of the pocket area. As a result higher temperature elevation occurred in the phantom containing MWNTs compared to the phantom without MWNTs. After 90 sec, the maximum temperature elevation in the pocket area (Phantom-MWNT) was determined to be 59 ^{0}C. However, outside the pocket area (where temperature was probed during the experimental model) temperature elevation was determined to be 50^{0}C for the same period of laser heating.

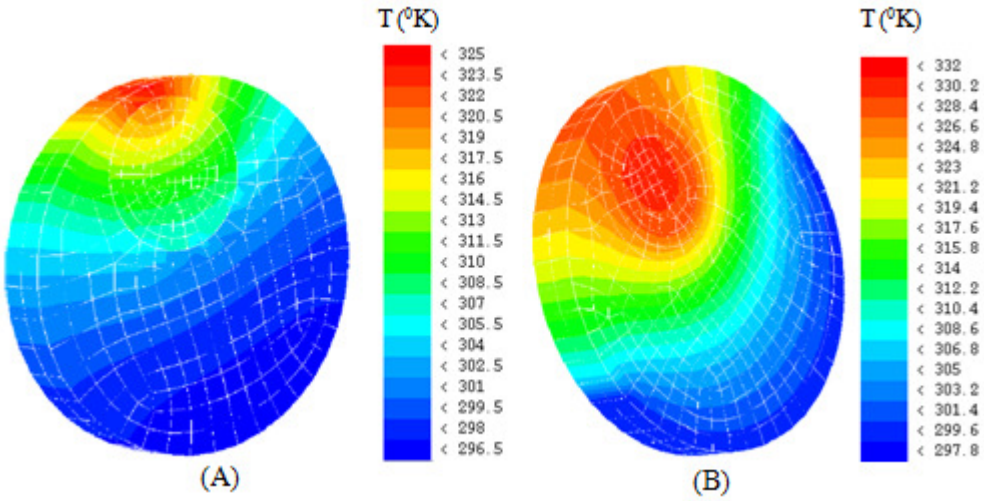

Figure 9.7: Temperature contour of phantom without MWNTs (A) and phantom with MWNTs (B).

9.5.2 Phantom Model Validation

To allow experimental validation of the phantom computational model, identical experimental conditions were used to allow comparison between model and experimentally measured temperature. Since the phantom contains a pocket of MWNTs, the laser power was measured by a power meter. The laser irradiance was determined to be 2.53 W/cm^2 4 mm below the surface which indicates the power loss was 44% compared to the incident laser power.

The phantom temperature was measured by MR thermometry using proton resonance MR temperature mapping protocol [23,151-152] during laser irradiation (4.6 W/cm^2) for 90 sec. Figure 9.8A shows the phantom with the MWNT pocket and the laser position. The temperature distribution was measured by MR thermometry as shown in Figure 9.8B. The time dependent

temperature profiles measured in the MWNT pocket and 2 mm away from the surface of the pocket are represented in Figure 9.8C. After 90 sec of laser heating temperature elevation was determined to be 52 ^{0}C in the pocket area and 41 ^{0}C outside the pocket area. The comparison between model predicted and experimentally measured temperatures of phantoms are 59 ^{0}C and 52 ^{0}C in the pocket area and 50 ^{0}C and 41 ^{0}C outside the pocket (2 mm away) respectively (Figure 9.9). Due to the significant light absorption by MWNTs, temperature in the pocket area is much higher compared to the surrounding phantom area without MWNTs. At this time, we are uncertain of the exact tumor position from which Figure 9.8 C was measured experimentally. However, our computational model determined temperature at a position near the center of the laser probe. In order to remedy this discrepancy between the model predicted and experimentally measured temperature, the location of experimental measurement will be clarified to allow accurate comparison between these two methods. If following clarification of measurement position there is still a discrepancy between the measured and model predicted temperature, these techniques will be further refined.

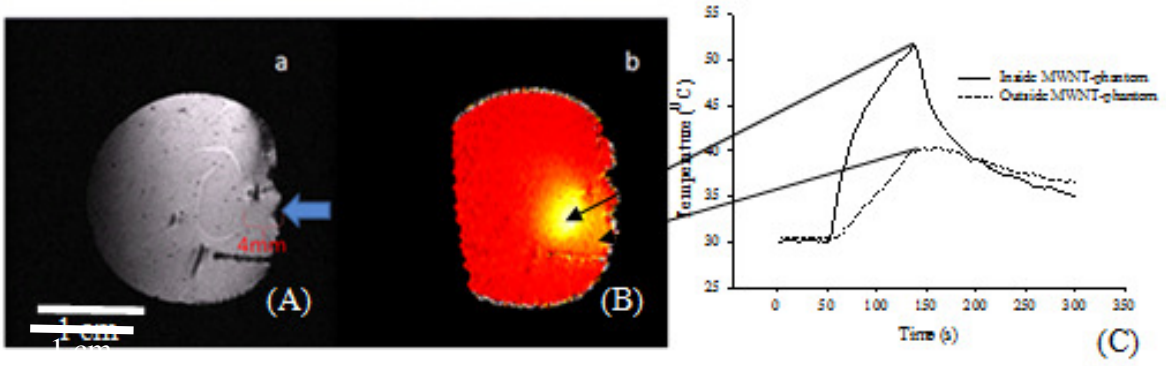

Figure 9.8: phantom with MWNTs showing laser direction (A). MRTI temperature data was showing in (B) and (C)

The calculated irradiance was compared with experimentally measured irradiance (2.53 W/cm^2, power loss 44%) and found to be close. This comparison validated the Monte Carlo simulation for our experiment. Temperature profiles determined by the computational model for phantoms containing MWNTs were compared with the temperature measured by our experimental model in order to validate our computational model (Figure 9.9). Though the position of the temperature probe in the experimental model is unknown, we probed the predicted temperature of our computational model in the middle of pocket and 2 mm outside of the pocket. The difference between the computationally predicted temperature and

experimentally predicted temperature arose because the accurate probing point of experimental model was unknown.

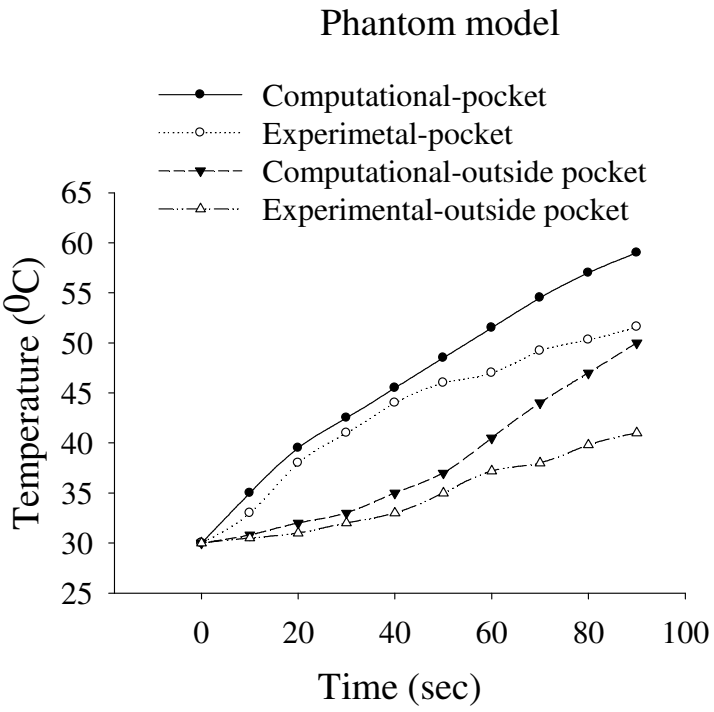

Figure 9.9: Comparison of temperature in the phantom predicted by the computational model and experimentally measured

9.5.3. Tumor computational model

Two types of tumor systems were designed for validation of the computational model, 1) tumor without MWNTs, 2) tumor with MWNTs injected uniformly as described earlier in section 9.4.1 . For both systems, the 20 mm diameter tumor was irradiated with an identical laser as described for the phantom experiments (irradiance 3 W/ cm^2 and beam diameter 10 mm) for 30 sec. The model predicted temperature distribution for the tumor without MWNTs is shown in Figure 9.9 A following 30 sec of heating with a maximum temperature elevation of 334 K near the laser probe. Temperature was probed near to the center of laser beam. After 30 sec maximum temperature elevation was found 61 ^{0}C for the tumor without MWNTs (Figure 9.10A).

The temperature distribution for the tumor with MWNT inclusion is shown in Figure 9. 10B depicting a much larger region experiencing significant temperature elevation. The

maximum temperature elevation near the laser probe was 77 ^{0}C which is significantly higher than the phantom without MWNTs.

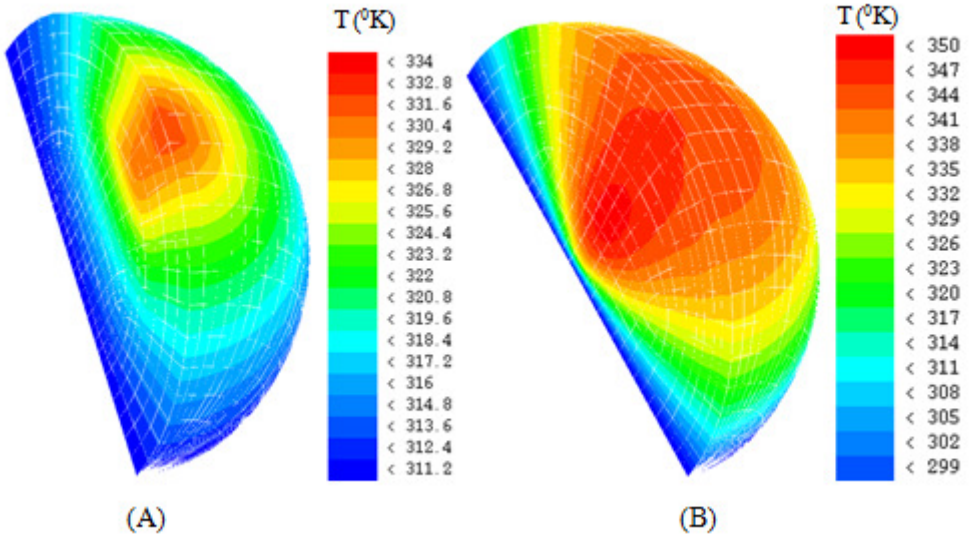

Figure 9.10: Temperature contour of tumor only (A) and tumor with MWNTs following laser irradiation (B).

9.5.4. Tumor experimental model

To validate the temperature prediction provided by the computational model, identical conditions were conducted experimentally. A continuous wave laser (irradiance 3 W/ cm^2 and beam diameter 10 mm) externally irradiated the RENCA kidney tumors and MRTI was utilized to measure the temperature distribution. (Figure 9.11). Tumors without MWNTs and with MWNTs experienced temperature elevation of 47 ^{0}C and 76 ^{0}C after 30 sec of laser heating respectively (Figure 9.11 C).

The computationally determined temperature profile was compared with experimental values in Figure 9.12. Both temperature profiles are quite similar. Model predicted and experimentally measured temperatures are 77 ^{0}C and 76 ^{0}C, and for without MWNTs they are 61 ^{0}C and 47 ^{0}C respectively. The discrepancy between the model predicted and experimentally predicted temperature may have arisen due to lack of knowledge regarding the location of temperature measurement in the experiments as described earlier for the phantom experiments. Furthermore, the experimental measurement determined the average temperature whereas the

model predicted the maximum temperature. The experimental measurement technique will be subsequently modified to facilitate better comparison with the model.

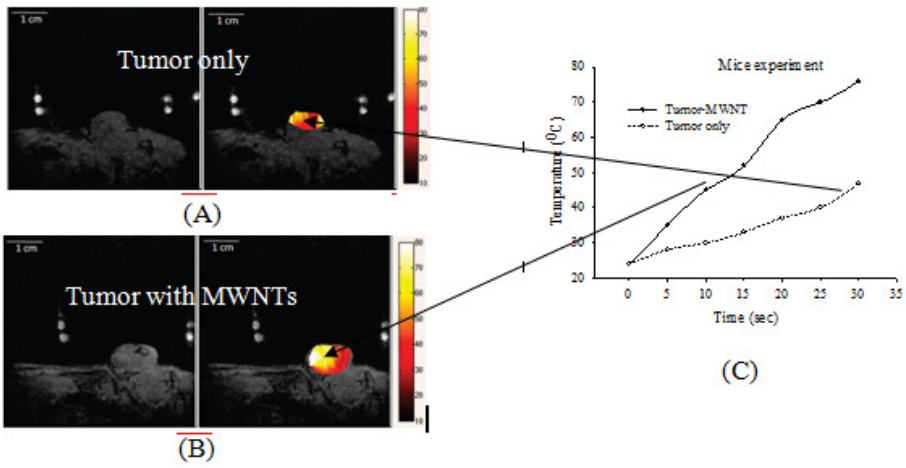

Figure 9. 11: Tumor and corresponding temperature distribution without MWNTs (A) and with MWNTs following laser heating (irradiance 3 W/m^2) for 30 sec (B). MRTI measured temperature profile after 30 sec laser heating (C)

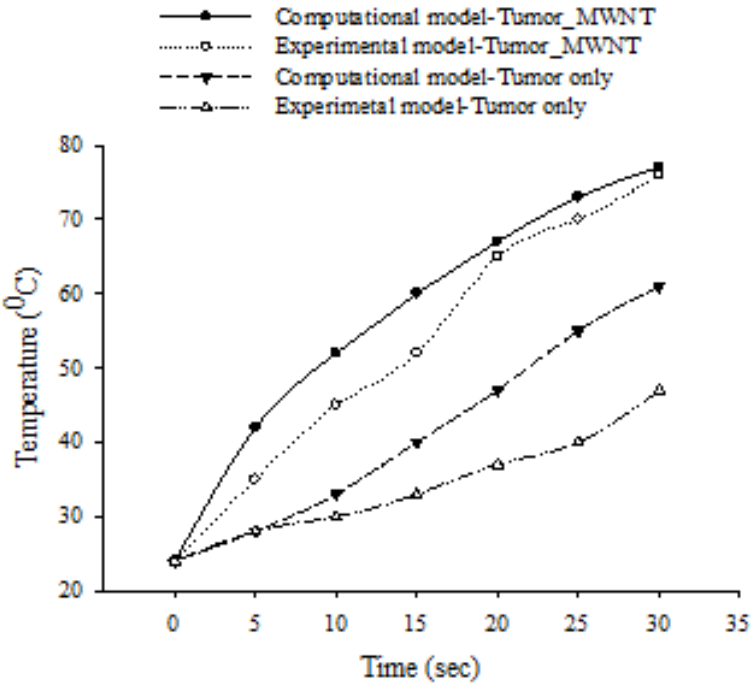

Figure 9.12: Comparison of temperature of tumor of computational model with experimental model

9.6. Discussion

In this study, two computational models for predicting the temperature response of phantoms and tumors with and without inclusion of MWNTs in response to laser irradiation were compared with experimentally measured temperature profiles.

9.6.1. Distribution study

In order to create a more realistic computational model, knowledge of the distribution of MWNTs in phantoms and tumors is critical. Our TEM images showed MWNTs in the phantom and tumors are uniformly distributed for various periods of times (2-48h). MWNTs were found inside and outside of tumor cells over these periods of time. Numerous MWNTs were observed in the cell cytoplasm, vacuole, nucleus, and cell membranes. Previous literature has also showed uptake of MWNTs and SWNTs in the cell nucleus and cytoplasm by TEM imaging and light microscopy [73,153]. Our distribution study in tissue representative phantom was the first study and MWNTs were found to be randomly distributed.

9.6.2. Comparison of experimental and computational study

Based on our distribution study, we developed computational models of phantoms and tumors considering with MWNTs homogeneously distributed. We used Penne's bioheat equation to determine the temperature distribution in response to laser heating before and following MWNT inclusion. The Penne's equation has been used successfully to determine the temperature distribution as verified by experimental measurements with MRTI thermometry [87-90]. Rylander *et al*. developed a computational model of tumor response to laser therapy using Penne's bioheat equation and determined the model predicted temperature was close to MRTI measured temperature [88].

The accuracy of our computational model can be attributed to accurate specification of MWNT distribution and optical and thermal properties which were determined based on experimental measurements. In our model, Penne's bioheat equation requires light absorption coefficient and thermal conductivity of phantom/tumor with MWNT composite which are unavailable in literatures. In our previous studies we measured absorption coefficients and thermal conductivity of tissue representative phantom-MWNT composites [144-145] and used as input parameters in the Penne's bioheat equation to predict temperature accurately. However in

our computational and experimental model (phantoms and tumors), model predicted temperature profile and experimentally measured temperature profile were significantly different from one another. This discrepancy arose because the exact location for experimental measurement was unknown whereas the model determined temperature at a specific position. Variance between the location of temperature determined for by experimental and computational methods has a significant impact. It is mandatory to know the accurate position of temperature in order to compare the computational and experimental model temperature. Prior to publication of this research, clarification of the location of experimental measurement and refinement of experimental and computational techniques will be conducted.

Computational models showed temperature to significantly increase after inclusion of MWNTs compared to phantoms and tumors without MWNT inclusion (Figure 9.7 and 9.10). A similar phenomena was verified by experimental measurements by MRTI which showed higher temperature elevation in the phantom and tumor with MWNT inclusion compared to cases without MWNT inclusion (Figure 9.8 and 9.11). The increased temperature elevation associated with MWNT inclusion can be attributed to increases in phantom and tumor absorption coefficient due to the presence of MWNTs. The antenna properties of MWNTs cause them to enhance the overall absorptivity of the phantom/tissue thereby increasing heat generation [34-37].Prior literature has also confirmed MWNTs to increase thermal deposition by absorbing laser light in NIR laser resulting in significant tumor destruction [22-24]. Introduction of MWNTs in phantoms and tissue also increased the overall thermal conductivity allowing enhanced heat diffusion [145].

9.7. Conclusion

A finite element computational treatment planning model was developed that enables prediction of the temperature distributions in laser irradiated tissue phantoms and tumors containing MWNT inclusion. Measured distributions of MWNTs within tissue representative phantoms and RENCA tumors were used to create accurate computational representations of geometry. The computational model was based on experimentally measured optical and thermal properties of phantoms containing MWNTs. The accuracy of the computational modelswas successfully validated with experimentally measured temperature in laser irradiated phantoms

and tumors with MWNT inclusion. Future work will include development of computational models for predicting HSP expression and damage in response to laser irradiation of phantoms and tumors with MWNT inclusion. Future models will also incorporate the ability to account for unique CNT properties (type, diameters, lengths, and concentration of MWNTs within the tissue) and laser parameters (wavelength, power, pulse duration, and fiber orientation) to determine ideal laser parameters and MWNT properties to achieve the desired patient specific response. All computational models will be experimentally validated using animal studies. Ultimately, utilization of this predictive model will enable a physician to investigate the tissue response to candidate treatments to better tailor a patient specific therapy to achieve maximum tumor destruction, minimal healthy tissue injury, and eliminate tumor recurrence.

9.8. Acknowledgement

This research was funded by the National Science Foundation Award CBET-0731108 and National Institutes of Health Award RO1CA12842. The content is solely the responsibility of the authors and does not necessarily represent the official views of the National Science Foundation or the National Institutes of Health.

10. References

1. Gittes RF. Carcinoma of the prostate. New England Journal of Medicine 1991; 324(4):236-245.
2. Kiang JG, Tsokos GC. Heat shock protein 70 kDa: Molecular biology, biochemistry, and physiology. Pharmacology & Therapeutics 1998; 80(2):183-201.
3. Tomei LD, and Cope, F.O., eds. Apoptosis: The Molecular Basis of Cell Death. Plainview, NY: Cold Spring Harbor Laboratory Press. 1991.
4. Calderwood SK, Khaleque MA, Sawyer DB, Ciocca DR. Heat shock proteins in cancer: chaperones of tumorigenesis. Trends in Biochemical Sciences 2006; 31(3):164-172.
5. Gibbons NB, Watson RWG, Coffey RNT, Brady HP, Fitzpatrick JM. Heat-shock proteins inhibit induction of prostate cancer cell apoptosis. Prostate 2000; 45(1):58-65.
6. Levine AJ, Momand J, Finlay CA. The p53 tumor suppressor gene. Nature 1991; 351(6326):453-456.
7. Soti C, Nagy E, Giricz Z, Vigh L, Csermely P, Ferdinandy P. Heat shock proteins as emerging therapeutic targets. British Journal of Pharmacology 2005; 146(6):769-780.
8. Georgopoulos C, Welch WJ. Role of the major heat-shock proteins as molecular chaperones. Annual Review of Cell Biology 1993; 9:601-634.
9. Martin J, Horwich AL, Hartl FU. Prevention of protein denaturation under heat-stress by the chaperonin hsp60. Science 1992; 258(5084):995-998.
10. Wiech H, Buchner J, Zimmermann R, Jakob U. HSP90 chaperones protein folding invitro. Nature 1992; 358(6382):169-170.
11. Ciocca DR, Clark GM, Tandon AK, Fuqua SAW, Welch WJ, McGuire WL. Heat-shock protein-HSP70 in patients with axillary lymph node-negative breast-cancer - prognostic implications. Journal of the National Cancer Institute 1993; 85(7):570-574.
12. Rylander MN, Feng YS, Zhang YJ, Bass J, Stafford RJ, Volgin A, Hazle JD, Diller KR. Optimizing heat shock protein expression induced by prostate cancer laser therapy through predictive computational models. Journal of Biomedical Optics 2006; 11(4).
13. Madersbacher S, Grobl M, Kramer G, Dirnhofer S, Steiner GE, Marberger M. Regulation of heat shock protein 27 expression of prostatic cells in response to heat treatment. Prostate 1998; 37(3):174-181.

14. Roigas J, Wallen ES, Loening SA, Moseley PL. Effects of combined treatment of chemotherapeutics and hyperthermia on survival and the regulation of heat shock proteins in dunning R3327 prostate carcinoma cells. Prostate 1998; 34(3):195-202.
15. Zhao BZ, Bilski PJ, He YY, Feng L, Chignell CF. Photo-induced reactive oxygen species generation by different water-soluble fullerenes (C-60) and their cytotoxicity in human keratinocytes. Photochemistry and Photobiology 2008; 84(5):1215-1223.
16. Campbell ID, Dwek RA. Biological spectroscopy. Menlo Park, Calif.: Benjamin/Cummings Pub. Co. 1984.
17. Welch AJ, Gemert, M. Optical-Thermal Response of Laser Irradiated Tissue: Plenum press. 1995.
18. Anderson RR, Parrish JA. The optics of human-skin. Journal of Investigative Dermatology 1981; 77(1):13-19.
19. Gun'kin I, Loginova N. Effect of nature of organic solvent on the absorption spectrum of C60 fullerene. Russian Journal of General Chemistry 2006; 76(12):1911-1913.
20. Hirsch LR, Stafford RJ, Bankson JA, Sershen SR, Rivera B, Price RE, Hazle JD, Halas NJ, West JL. Nanoshell-mediated near-infrared thermal therapy of tumors under magnetic resonance guidance. Proceedings of the National Academy of Sciences of the United States of America 2003; 100(23):13549-13554.
21. Levi-Polyachenko NH, Carroll DL, Stewart JH. Applications of Carbon-Based Nanomaterials for Drug Delivery in Oncology. 2008:223-266.
22. Sarkar S, Fisher J, Rylander C, Rylander MN. Photothermal Response of Tissue Phantoms Containing Multi-Walled Carbon Nanotubes. Journal of Biomechanical Engineering 2010; 132(4):044505.
23. Burke A, Ding XF, Singh R, Kraft RA, Levi-Polyachenko N, Rylander MN, Szot C, Buchanan C, Whitney J, Fisher J, Hatcher HC, D'Agostino R, Kock ND, Ajayan PM, Carroll DL, Akman S, Torti FM, Torti SV. Long-term survival following a single treatment of kidney tumors with multiwalled carbon nanotubes and near-infrared radiation. Proceedings of the National Academy of Sciences of the United States of America 2009; 106(31):12897-12902.

24. Torti SV, Byrne F, Whelan O, Levi N, Ucer B, Schmid M, Torti FM, Akman S, Liu J, Ajayan PM, Nalamasu O, Carroll DL. Thermal ablation therapeutics based on CNx multi-walled nanotubes. International Journal of Nanomedicine 2007; 2(4):707-714.
25. Iijima S. Helical microtubules of graphitic carbon. Nature 1991; 354(6348):56-58.
26. Kam NWS, O'Connell M, Wisdom JA, Dai HJ. Carbon nanotubes as multifunctional biological transporters and near-infrared agents for selective cancer cell destruction. Proceedings of the National Academy of Sciences of the United States of America 2005; 102(33):11600-11605.
27. Bassil A, Puech P, Tubery L, Bacsa W, Flahaut E. Controlled laser heating of carbon nanotubes. Applied Physics Letters 2006; 88(17).
28. Dresselhaus MS, G. Dresselhaus, and P. C. Eklund. Science of fullerenes and carbon nanotubes. San Diego: Academic Press. 1996.
29. Adams TA. Physical properties of carbon nanotubes. 2000.
30. Daenen MJM. Wondrous World of Carbon Nanotubes. 2003.
31. Miyako E, Nagata H, Hirano K, Sakamoto K, Makita Y, Nakayama K, Hirotsu T. Photoinduced antiviral carbon nanohorns. Nanotechnology 2008; 19(7).
32. Miyawaki J, Yudasaka M, Azami T, Kubo Y, Iijima S. Toxicity of single-walled carbon nanohorns. Acs Nano 2008; 2(2):213-226.
33. Sun X, Yu RQ, Xu GQ, Hor TSA, Ji W. Broadband optical limiting with multiwalled carbon nanotubes. Applied Physics Letters 1998; 73(25):3632-3634.
34. Burke PJ, Li SD, Yu Z. Quantitative theory of nanowire and nanotube antenna performance. Ieee Transactions on Nanotechnology 2006; 5(4):314-334.
35. Hanson GW. Fundamental transmitting properties of carbon nanotube antennas. Ieee Transactions on Antennas and Propagation 2005; 53(11):3426-3435.
36. Kempa K, Rybczynski J, Huang ZP, Gregorczyk K, Vidan A, Kimball B, Carlson J, Benham G, Wang Y, Herczynski A, Ren ZF. Carbon nanotubes as optical antennae. Advanced Materials 2007; 19(3):421-+.
37. Wang Y, Kempa K, Kimball B, Carlson JB, Benham G, Li WZ, Kempa T, Rybczynski J, Herczynski A, Ren ZF. Receiving and transmitting light-like radio waves: Antenna effect in arrays of aligned carbon nanotubes. Applied Physics Letters 2004; 85(13):2607-2609.

38. Levi-Polyachenko N, Carroll, D.L., and Stewart, J.H. Applications of Carbon-Based Nanomaterials for Drug Delivery in Oncology Cataldo F, and Ros, T.D., editor. Netherlands: Springer. 2008.
39. Brown E, Hao L, Gallop JC, Macfarlane JC. Ballistic thermal and electrical conductance measurements on individual multiwall carbon nanotubes. Applied Physics Letters 2005; 87(2).
40. Hone J, Whitney M, Zettl A. Thermal conductivity of single-walled carbon nanotubes. 1998 Jul 12-18 Jun; Montpellier, France. Elsevier Science Sa. p 2498-2499.
41. Eletskii AV. Transport properties of carbon nanotubes. Phys Usp 2009; 52(3):209-224.
42. Fujii M, Zhang X, Xie H, Ago H, Takahashi K, Ikuta T, Abe H, Shimizu T. Measuring the Thermal Conductivity of a Single Carbon Nanotube. Physical Review Letters 2005; 95(Copyright (C) 2009 The American Physical Society):065502.
43. Yi W, Lu L, Dian-lin Z, Pan ZW, Xie SS. Linear specific heat of carbon nanotubes. Physical Review B 1999; 59(Copyright (C) 2009 The American Physical Society):R9015.
44. Hone J, Whitney M, Zettl A. Thermal conductivity of single-walled carbon nanotubes. Synthetic Metals 1999; 103(1-3):2498-2499.
45. Holmes KR, Chen, MM. Local thermal conductivity of Para-7 fibrosarcoma in hamster. 1979 Advances in Bioengineering 1979:147-149.
46. Valvano JW, Cochran JR, Diller KR. Thermal-conductivity and diffusivity of biomaterials measured with self-heated thermistors. International Journal of Thermophysics 1985; 6(3):301-311.
47. Nan CW, Liu G, Lin YH, Li M. Interface effect on thermal conductivity of carbon nanotube composites. Applied Physics Letters 2004; 85(16):3549-3551.
48. Pennes HH. Analysis of tissue and arterial blood temperatures in the resting human forearm (Reprinted from Journal of Applied Physiology, vol 1, pg 93-122, 1948). Journal of Applied Physiology 1998; 85(1):5-34.
49. Bhattacharya A, Mahajan RL. Temperature dependence of thermal conductivity of biological tissues. Physiological Measurement 2003; 24(3):769-783.
50. Cohen ML. Measurement of the thermal properties of human skin. A review. J Investig Dermatol 1977; 69(3):333-338.

51. Ducharme MB, Tikuisis P. In vivo thermal conductivity of the human forearm tissues. J Appl Physiol 1991; 70(6):2682-2690.
52. Liang XG, Ge XS, Zhang YP, Wang GJ. A convenient method of measuring the thermal-conductivity of biological tissue. Physics in Medicine and Biology 1991; 36(12):1599-1605.
53. Poppendiek HF, Randall R, Breeden JA, Chambers JE, Murphy JR. Thermal conductivity measurements and predictions for biological fluids and tissues. Cryobiology; 3(4):318-327.
54. Yi* M, Panchawagh HV, Podhajsky RJ, Mahajan RL. Micromachined Hot-Wire Thermal Conductivity Probe for Biomedical Applications. Biomedical Engineering, IEEE Transactions on 2009; 56(10):2477-2484.
55. Hill JE, Leitman, J.D., Sunderland, J.E. Thermal conductivity of various meats. Food Technology 1967; 21:1143-1148.
56. Zhang HF, He LQ, Cheng SX, Zhai ZT, Gao DY. A dual-thermistor probe for absolute measurement of thermal diffusivity and thermal conductivity by the heat pulse method. Measurement Science & Technology 2003; 14(8):1396-1401.
57. Arkin H, Holmes KR, Chen MM, Bottje WG. Thermal Pulse Decay Method for Simultaneous Measurement of Local Thermal Conductivity and Blood Perfusion: A Theoretical Analysis. Journal of Biomechanical Engineering 1986; 108(3):208-214.
58. Bhavaraju NC, Cao H, Yuan DY, Valvano JW, Webster JG. Measurement of directional thermal properties of biomaterials. Biomedical Engineering, IEEE Transactions on 2001; 48(2):261-267.
59. Gummow RJ, Sigalas I. Generalised hot-wire technique for high pressure thermal conductivity measurements. Journal of Physics E: Scientific Instruments 1988; 21(5):442.
60. Wang LV, and Wu, H. Biomedical Optics Principles and Imaging. New Jersey: Wiley and Sons, Inc. 2007.
61. Esteban Ó, Marvá F, Martínez-Antón JC. Optical constants of a sodium alginate polymer in the UV-vis range. Optical Materials 2009; 31(4):696-699.
62. Patterson EM, Shelden CE, Stockton BH. Kubelka-munk optical-properties of a barium-sulfate white reflectance standard. Applied Optics 1977; 16(3):729-732.

63. Wei HJ, Xing D, Wu GY, Gu HM, Lu FJ, Jin Y, Li XY. Differences in optical properties between healthy and pathological human colon tissues using a Ti : sapphire laser: an in vitro study using the Monte Carlo inversion technique. Journal of Biomedical Optics 2005; 10(4).
64. Firbank M, Hiraoka M, Essenpreis M, Delpy DT. Measurement of the optical-properties of the skull in the wavelength range 650-950 nm. Physics in Medicine and Biology 1993; 38(4):503-510.
65. Troy TL, Thennadil SN. Optical properties of human skin in the near infrared wavelength range of 1000 to 2200 nm. Journal of Biomedical Optics 2001; 6(2):167-176.
66. Prahl SA, Vangemert MJC, Welch AJ. Determining the optical-properties of turbid media by using the adding-doubling method. Applied Optics 1993; 32(4):559-568.
67. Yamakoshi Y, Umezawa N, Ryu A, Arakane K, Miyata N, Goda Y, Masumizu T, Nagano T. Active oxygen species generated from photoexcited fullerene (C-60) as potential medicines: O-2(-center dot) versus O-1(2). Journal of the American Chemical Society 2003; 125(42):12803-12809.
68. Tagmatarchis N, Kato H, Shinohara H. Novel singlet oxygen generators: the nature and the number of trapped metal atoms in endohedral metallofullerenes M@C-82 (M=Dy, Gd, La) and Dy-2@C-2n (2n=84-94). Physical Chemistry Chemical Physics 2001; 3(15):3200-3202.
69. Wang SZ, Gao RM, Zhou FM, Selke M. Nanomaterials and singlet oxygen photosensitizers: potential applications in photodynamic therapy. Journal of Materials Chemistry 2004; 14(4):487-493.
70. Yanagi K, Okubo S, Okazaki T, Kataura H. Endohedral metallofullerenes as strong singlet oxygen quenchers. Chemical Physics Letters 2007; 435(4-6):306-310.
71. Karsson J. Introduction to nutraology and radical formation. In: *Antioxidants and Exercise* Illinois Human Kinetics Press, 1997. 1-143 p.
72. WikipediA. Haber-Weiss reaction.
73. Cheng C, Muller KH, Koziol KKK, Skepper JN, Midgley PA, Welland ME, Porter AE. Toxicity and imaging of multi-walled carbon nanotubes in human macrophage cells. Biomaterials 2009; 30(25):4152-4160.

74. Monteiro-Riviere NA, Nemanich RJ, Inman AO, Wang YYY, Riviere JE. Multi-walled carbon nanotube interactions with human epidermal keratinocytes. Toxicology Letters 2005; 155(3):377-384.

75. Yehia HN, Draper RK, Mikoryak C, Walker EK, Bajaj P, Musselman IH, Daigrepont MC, Dieckmann GR, Pantano P. Single-walled carbon nanotube interactions with HeLa cells. Journal of Nanobiotechnology 2007; 5:Article No.: 8.

76. Cui DX, Tian FR, Ozkan CS, Wang M, Gao HJ. Effect of single wall carbon nanotubes on human HEK293 cells. Toxicology Letters 2005; 155(1):73-85.

77. Liu Z, Davis C, Cai WB, He L, Chen XY, Dai HJ. Circulation and long-term fate of functionalized, biocompatible single-walled carbon nanotubes in mice probed by Raman spectroscopy. Proceedings of the National Academy of Sciences of the United States of America 2008; 105(5):1410-1415.

78. Webster S, Maultzsch J, Thomsen C, Liu J, Czerw R, Terrones M, Adar F, John C, Whitley A, Carroll DL. Raman characterization of nitrogen doped multiwalled carbon nanotubes. In: Bernier P, Carroll D, Kim GT, Roth S, editors. Materials Research Society Symposium Proceedings; 2003 Apr 22-25; San Francisco, Ca. Materials Research Society. p 129-134. (Materials Research Society Symposium Proceedings).

79. Xu JF, Xiao M, Czerw R, Carroll DL. Optical limiting and enhanced optical nonlinearity in boron-doped carbon nanotubes. Chemical Physics Letters 2004; 389(4-6):247-250.

80. Lang J, Erdmann B, Seebass M. Impact of nonlinear heat transfer on temperature control in regional hyperthermia. Ieee Transactions on Biomedical Engineering 1999; 46(9):1129-1138.

81. Zhu D, Luo QM, Zhu GM, Liu W. Kinetic thermal response and damage in laser coagulation of tissue. Lasers in Surgery and Medicine 2002; 31(5):313-321.

82. Beop-Min K, Jacques SL, Rastegar S, Thomsen S, Motamedi M. Nonlinear finite-element analysis of the role of dynamic changes in blood perfusion and optical properties in laser coagulation of tissue. Selected Topics in Quantum Electronics, IEEE Journal of 1996; 2(4):922-933.

83. Anvari B, Rastegar S, Motamedi M. Modeling of intraluminal heating of biological tissue: implications for treatment of benign prostatic hyperplasia. Biomedical Engineering, IEEE Transactions on 1994; 41(9):854-864.

84. Mohammed Y, Verhey J. A finite element method model to simulate laser interstitial thermo therapy in anatomical inhomogeneous regions. BioMedical Engineering OnLine 2005; 4(1):2.

85. Rylander MN, Diller KR, Wang SH, Aggarwal SJ. Correlation of HSP70 expression and cell viability following thermal stimulation of bovine aortic endothelial cells. Journal of Biomechanical Engineering-Transactions of the Asme 2005; 127(5):751-757.

86. Feng Y, Fuentes D, Hawkins A, Bass JM, Rylander MN. Optimization and real-time control for laser treatment of heterogeneous soft tissues. Computer Methods in Applied Mechanics and Engineering 2009; 198(21-26):1742-1750.

87. Rylander MN, Feng Y, Bass J, Diller KR. Heat shock protein expression and injury optimization for laser therapy design. Lasers in Surgery and Medicine 2007; 39(9):731-746.

88. Rylander MN, Feng Y, Zhang Y, Bass J, Stafford RJ, Volgin A, Hazle JD, Diller KR. Optimizing heat shock protein expression induced by prostate cancer laser therapy through predictive computational models. Journal of Biomedical Optics 2006; 11(4):041113.

89. Oden JT, Diller KR, Bajaj C, Browne JC, Hazle J, Babuška I, Bass J, Demkowicz L, Feng Y, Fuentes D, Prudhomme S, Rylander MN, Stafford RJ, Zhang Y. Development of a Computational Paradigm for Laser Treatment of Cancer. In: Alexandrov V, van Albada G, Sloot P, Dongarra J, eds. Computational Science – ICCS 2006. Volume 3993, Lecture Notes in Computer Science: Springer Berlin / Heidelberg. 2006:530-537.

90. Oden JT, Diller KR, Bajaj C, Browne JC, Hazle J, Babuska I, Bass J, Biduat L, Demkowicz L, Elliott A, Feng Y, Fuentes D, Prudhomme S, Rylander MN, Stafford RJ, Zhang Y. Dynamic data-driven finite element models for laser treatment of cancer. Numerical Methods for Partial Differential Equations 2007; 23(4):904-922.

91. Poppendiek H.F. RR, Breeden J.A., Chambers J.E., Murphy J.R. Thermal conductivity measurements and predictions for biological fluids and tissues. Cryobiology 1966; 3(5):318-327.

92. Ishii K, Kimura A, Awazu K. Optical properties of tissues after laser treatments in the wavelength range of 350-1000 nm - art. no. 69912F. In: Popp J, Drexler W, Tuchin VV, Matthews DL, editors. Proceedings of the Society of Photo-Optical Instrumentation

Engineers (Spie); 2008 Apr 08-10; Strasbourg, FRANCE. p F9912-F9912. (Proceedings of the Society of Photo-Optical Instrumentation Engineers (Spie)).

93. Rafii-Tabar H. Computational physics of carbon nanotubes. Cambridge, UK: Cambridge University Press. 2008.

94. Fan X, et al. Isolation of carbon nanohorn assemblies and their potential for intracellular delivery. Nanotechnology 2007; 18(19):195103.

95. Iijima S, Yudasaka M, Yamada R, Bandow S, Suenaga K, Kokai F, Takahashi K. Nano-aggregates of single-walled graphitic carbon nano-horns. Chemical Physics Letters 1999; 309(3-4):165-170.

96. Miyako E, et al. Near-infrared laser-triggered carbon nanohorns for selective elimination of microbes. Nanotechnology 2007; 18(47):475103.

97. Zhang M, Murakami T, Ajima K, Tsuchida K, Sandanayaka ASD, Ito O, Iijima S, Yudasaka M. Fabrication of ZnPc/protein nanohorns for double photodynamic and hyperthermic cancer phototherapy. Proceedings of the National Academy of Sciences of the United States of America 2008; 105(39):14773-14778.

98. Merabia S, Shenogin S, Joly L, Keblinski P, Barrat J-L. Heat transfer from nanoparticles: A corresponding state analysis. Proceedings of the National Academy of Sciences 2009:-.

99. Huxtable ST, Cahill DG, Shenogin S, Xue L, Ozisik R, Barone P, Usrey M, Strano MS, Siddons G, Shim M, Keblinski P. Interfacial heat flow in carbon nanotube suspensions. Nat Mater 2003; 2(11):731-734.

100. Nan C-W, Birringer R, Clarke DR, Gleiter H. Effective thermal conductivity of particulate composites with interfacial thermal resistance. Journal of Applied Physics 1997; 81(10):6692-6699.

101. Bryning MB, Milkie DE, Islam MF, Kikkawa JM, Yodh AG. Thermal conductivity and interfacial resistance in single-wall carbon nanotube epoxy composites. Applied Physics Letters 2005; 87(16):161909.

102. Clancy TC, Gates TS. Modeling of interfacial modification effects on thermal conductivity of carbon nanotube composites. Polymer 2006; 47(16):5990-5996.

103. Gao L, Zhou X, Ding Y. Effective thermal and electrical conductivity of carbon nanotube composites. Chemical Physics Letters 2007; 434(4-6):297-300.

104. Warheit DB, Laurence BR, Reed KL, Roach DH, Reynolds GAM, Webb TR. Comparative Pulmonary Toxicity Assessment of Single-wall Carbon Nanotubes in Rats. Toxicol Sci 2004; 77(1):117-125.
105. Blackwell JH. A Transient-Flow Method for Determination of Thermal Constants of Insulating Materials in Bulk Part I---Theory. Journal of Applied Physics 1954; 25(2):137-144.
106. Carslaw HS, Jaeger JC. Conduction of heat in solids. Oxford,: Clarendon Press. 1959. 510 p. p.
107. Nix G.H. LGW, Vachon R.I. and Tanger G.E. Direct determination of thermal diffusivity and conductivity with a refined line-source technique. Process in Aeronautics and Astronautics: Thermophysics of Spacecraft and Planetary Bodies 1967; 20:865-878.
108. Lee CSD, Gleghorn JP, Won Choi N, Cabodi M, Stroock AD, Bonassar LJ. Integration of layered chondrocyte-seeded alginate hydrogel scaffolds. Biomaterials 2007; 28(19):2987-2993.
109. Wong M. Alginates in Tissue Engineering. Volume 238. 2003:77-86.
110. Moffat RJ. Describing the uncertainties in experimental results. Experimental Thermal and Fluid Science 1988; 1(1):3-17.
111. Figliola RS, and Beasley, D.E. Theory and design for mechanical measurements. Hoboken, N.J.: John Wiley. 1995.
112. Saltiel C, Manickavasagam S, Menguc MP, Andrews R. Light-scattering and dispersion behavior of multiwalled carbon nanotubes. Journal of the Optical Society of America a-Optics Image Science and Vision 2005; 22(8):1546-1554.
113. Malic E, Hirtschulz M, Milde F, Wu Y, Maultzsch J, Heinz TF, Knorr A, Reich S. Theory of Rayleigh scattering from metallic carbon nanotubes. Physical Review B 2008; 77(4).
114. Rozhin AG, Sakakibara Y, Tokumoto M, Kataura H, Achiba Y. Near-infrared nonlinear optical properties of single-wall carbon nanotubes embedded in polymer film. Thin Solid Films 2004; 464-465:368-372.
115. Casey A, Farrell GF, McNamara M, Byrne HJ, Chambers G. Interaction of carbon nanotubes with sugar complexes. Synthetic Metals 2005; 153(1-3):357-360.

116. Scardaci V, Sun ZP, Wang F, Rozhin AG, Hasan T, Hennrich F, White IH, Milne WI, Ferrari AC. Carbon Nanotube Polycarbonate Composites for Ultrafast Lasers. Advanced Materials 2008; 20(21):4040-+.
117. O'Flaherty SM, Hold SV, Brennan ME, Cadek M, Drury A, Coleman JN, Blau WJ. Nonlinear optical response of multiwalled carbon-nanotube dispersions. Journal of the Optical Society of America B-Optical Physics 2003; 20(1):49-58.
118. Husanu M, Baibarac M, Baltog I. Particular signature of isolated and bundled carbon nanotubes in their Raman spectra. Romanian Reports in Physics 2008; 60(3):691-699.
119. Guo Z, Du F, Ren DM, Chen YS, Zheng JY, Liu ZB, Tian JG. Covalently porphyrin-functionalized single-walled carbon nanotubes: a novel photoactive and optical limiting donor-acceptor nanohybrid. Journal of Materials Chemistry 2006; 16(29):3021-3030.
120. Jeong SH, Kim KK, Jeong SJ, An KH, Lee SH, Lee YH. Optical absorption spectroscopy for determining carbon nanotube concentration in solution. Synthetic Metals 2007; 157(13-15):570-574.
121. Kymakis E, Amaratunga GAJ. Optical properties of polymer-nanotube composites. Synthetic Metals 2004; 142(1-3):161-167.
122. Khudyakov DV, Lobach AS, Nadtochenko VA. Nonlinear optical absorption of single-wall carbon nanotubes in carboxymethylcellulose thin polymer film and its application as a saturable absorber for mode-locking in pulsed Nd:glass laser. Applied Optics 2009; 48(8):1624-1627.
123. Royston DD, Poston RS, Prahl SA. Optical properties of scattering and absorbing materials used in the development of optical phantoms at 1064 nm. Journal of Biomedical Optics 1996; 1(1):110-116.
124. Honda N, Ishii, K., Kimura, A., Sakai, M., and Awazu, K. Determination of optical property changes by laser treatments using inverse adding-doubling method Proceedings of SPIE 2009; 7175(71750Q):1-8.
125. Cheng M-D, et al. Formation studies and controlled production of carbon nanohorns using continuous in situ characterization techniques. Nanotechnology 2007; 18(18):185604.
126. Geohegan D, Puretzky A, Ivanov I, Eres G, Liu Z, Styers-Barnett D, Hu HUI, Zhao BIN, Cui H, Rouleau C, Jesse S, Britt P, Christen H, Xiao KAI, Fleming P, Meldrum AL.

Laser-based synthesis, diagnostics, and control of single-walled carbon nanotubes and nanohorns for composites and biological nanovectors. 2006:205-223.

127. Lualdi M, Colombo A, Farina B, Tomatis S, Marchesini R. A phantom with tissue-like optical properties in the visible and near infrared for use in photomedicine. Lasers in Surgery and Medicine 2001; 28(3):237-243.

128. Hebden JC, Hall DJ, Firbank M, Delpy DT. Time-resolved optical imaging of a solid tissue-equivalent phantom. Appl Opt 1995; 34(34):8038-8047.

129. Kim J, Davé DP, Rylander CG, Oh J, Milner TE. Spatial refractive index measurement of porcine artery using differential phase optical coherence microscopy. Lasers in Surgery and Medicine 2006; 38(10):955-959.

130. Rylander CG, Davé DP, Akkin T, Milner T, Diller KR, Welch AJ. Quantitative phase-contrast imaging of cells with phase-sensitive opticalcoherence microscopy. Opt Lett 2004; 29(13):1509-1511.

131. Hale GM, and Query, M.R. Optical Constants of Water in the 200-nm to 200-µm Wavelength Region. Applied Optics 1973; 12(3):555-563.

132. Niskanen I, Raty J, Peiponen KE. Estimation of effective refractive index of birefringent particles using a combination of the immersion liquid method and light scattering. Applied Spectroscopy 2008; 62(4):399-401.

133. Gates B, Park SH, Xia YN. Tuning the photonic bandgap properties of crystalline arrays of polystyrene beads by annealing at elevated temperatures. Advanced Materials 2000; 12(9):653-+.

134. Beek JF, et al. In vitro double-integrating-sphere optical properties of tissues between 630 and 1064 nm. Physics in Medicine and Biology 1997; 42(11):2255.

135. Vishwanath K, Klein D, Chang K, Schroeder T, Dewhirst MW, Ramanujam N. Quantitative optical spectroscopy can identify long-term local tumor control in irradiated murine head and neck xenografts. Journal of Biomedical Optics 2009; 14(5).

136. Brown JQ, Wilke LG, Geradts J, Kennedy SA, Palmer GM, Ramanujam N. Quantitative Optical Spectroscopy: A Robust Tool for Direct Measurement of Breast Cancer Vascular Oxygenation and Total Hemoglobin Content In vivo. Cancer Res 2009; 69(7):2919-2926.

137. Brennan ME, Coleman JN, Drury A, Lahr B, Kobayashi T, Blau WJ. Nonlinear photoluminescence from van Hove singularities in multiwalled carbon nanotubes. Opt Lett 2003; 28(4):266-268.
138. Arbogast JW, Darmanyan AP, Foote CS, Diederich FN, Whetten RL, Rubin Y, Alvarez MM, Anz SJ. Photophysical properties of sixty atom carbon molecule (C60). The Journal of Physical Chemistry 2002; 95(1):11-12.
139. Orfanopoulos M, Kambourakis S. Chemical evidence of singlet oxygen production from C60 and C70 in aqueous and other polar media. Tetrahedron Letters 1995; 36(3):435-438.
140. Sandra S, Gareth, R., and Lawrence, J. Biomedical EPR, Part B: Methodology, Instrumentation and Dynamics. New York: Kluwer academic publishers. 2005.
141. Hagen WR. Biomolecular EPR spectroscopy. Boca Raton: CRC Press. 2009. xii, 249 p. p.
142. Eijiro M, et al. Near-infrared laser-triggered carbon nanohorns for selective elimination of microbes. Nanotechnology 2007; 18(47):475103.
143. Fenoglio I, Tomatis M, Lison D, Muller J, Fonseca A, Nagy JB, Fubini B. Reactivity of carbon nanotubes: Free radical generation or scavenging activity? Free Radical Biology and Medicine 2006; 40(7):1227-1233.
144. Sarkar S, Gurjarpadhye, A., Rylander, C.G., Rylander, M.N., . Comparison of optical properties of breast tumor phantoms containing SWNTs, MWNTs, and SWNHs. Lasers in surgery and medicine 2010; Under review.
145. Sarkar S, and Rylander, M.N. Measurement of thermal conductivity of carbon nanotube-tissue phantom composites with hot wire probe method. Annals of biomedical engineering 2010; Under review.
146. Roggan A, Mesecke-von Rheinbaben I, Knappe V, Vogl T, Mack M, Germer C, Albrecht D, Muller G. Applicator development and irradiation planning in laser-induced thermotherapy (LITT). Biomedizinische Technik 1997; 42(Suppl):332 - 333.
147. Schwarzmaier HJ, Yaroslavsky IV, Yaroslavsky AN, Fiedler V, Ulrich F, Kahn T. Treatment planning for MRI-guided laser-induced interstitial thermotherapy of brain tumors—The role of blood perfusion. Journal of Magnetic Resonance Imaging 1998; 8(1):121-127.

148. Wang S, Xie W, Rylander N, #160, Marissa, Tucker, W. P, Aggarwal, Shanti, Diller, R. K. HSP70 Kinetics Study by Continuous Observation of HSP-GFP Fusion Protein Expression on a Perfusion Heating Stage. Hoboken, NJ, ETATS-UNIS: Wiley. 2008. 9 p.

149. Feng Y, Fuentes D, Hawkins A, Bass J, Rylander M, Elliott A, Shetty A, Stafford R, Oden J. Nanoshell-mediated laser surgery simulation for prostate cancer treatment. Engineering with Computers 2009; 25(1):3-13.

150. Feng YS, Fuentes D, Hawkins A, Bass J, Rylander MN, Elliott A, Shetty A, Stafford RJ, Oden JT. Nanoshell-mediated laser surgery simulation for prostate cancer treatment. 2006 Jul 16-22 Jan; Los Angeles, CA. p 3-13.

151. Peters RTD, Hinks RS, Henkelman RM. Ex vivo tissue-type independence in proton-resonance frequency shift MR thermometry. Magnetic Resonance in Medicine 1998; 40(3):454-459.

152. Bernstein MA, Fain SB, Riederer SJ. Effect of windowing and zero-filled reconstruction of MRI data on spatial resolution and acquisition strategy. Journal of Magnetic Resonance Imaging 2001; 14(3):270-280.

153. Bottini M, Cerignoli F, Dawson MI, Magrini A, Rosato N, Mustelin T. Full-length single-walled carbon nanotubes decorated with streptavidin-conjugated quantum dots as multivalent intracellular fluorescent nanoprobes. Biomacromolecules 2006; 7(8):2259-2263.

11. Appendix

Dear Mr. Sarkar:

It is our pleasure to grant you permission to use ASME paper "Photothermal Response of Tissue Phantoms Containing Multi- Walled Carbon Nanotubes," by Saugata Sarkar, Jessica Fisher, Christopher Rylander, Marissa Nichole Rylander, Journal of Biomechanical Engineering, Vol. 132, 2010, cited in your letter for inclusion in a Thesis and Dissertation entitled Photothermal Response of Tissue Phantoms Containing Multi- Walled Carbon Nanotubes to be published by Electronic Theses and Dissertations (ETD) with Virginia Tech in the archive located at http://etd.vt.edu/.

As is customary, we ask that you ensure full acknowledgment of this material, the author(s), source and ASME as original publisher on all printed copies being distributed.

Many thanks for your interest in ASME publications.

Sincerely,

Beth Darchi
Permissions & Copyrights
ASME, 3 Park Avenue
New York, NY 10016
T: 212-591-7700
F: 212-591-7841
E: darchib@asme.org